

**Validation of Rochester Institute of Technology's (RIT's)  
Digital Image and Remote Sensing Image Generation (DIRSIG) Model -  
Reflective Region**

Russell A. White

Rochester Institute of Technology  
Chester F. Carlson Center for Imaging Science

A thesis submitted in partial fulfillment of the  
requirements for the degree of Master of Science  
at the Chester F. Carlson Center for Imaging Science  
in the College of Science  
of the Rochester Institute of Technology

July 1996

Signature of the Author

---

Accepted by \_\_\_\_\_

Coordinator, M.S. Degree Program

CHESTER F. CARLSON  
CENTER FOR IMAGING SCIENCE  
COLLEGE OF SCIENCE  
ROCHESTER INSTITUTE OF TECHNOLOGY  
ROCHESTER, NEW YORK

CERTIFICATE OF APPROVAL

---

**M.S. DEGREE THESIS**

---

The M.S. Degree Thesis of Russell A. White  
has been examined and approved by the  
thesis committee as satisfactory for the  
thesis requirement for the  
Master of Science degree

---

—  
Dr. John R. Schott

---

—  
Dr. Robert Fiete

Mr. Rolando Raqueño

---

Date

THESIS RELEASE PERMISSION FORM  
ROCHESTER INSTITUTE OF TECHNOLOGY  
CENTER FOR IMAGING SCIENCE

**Validation of Rochester Institute of Technology's (RIT's)  
Digital Image and Remote Sensing Image Generation (DIRSIG) Model -  
Reflective Region**

I, Russell A. White, hereby grant permission to the Wallace Memorial Library of R.I.T., to reproduce my thesis in whole or in part. Any reproduction will not be for commercial use or profit.

Signature: \_\_\_\_\_

Date: \_\_\_\_\_

## ACKNOWLEDGMENTS

I would like to thank Dr. Schott, Dr. Robert Fiete, Mr. Rolando Raqueño, and Mr. Scott Brown for their support in this study. All have busy schedules and other obligations, but found time to provide encouragement, to listen, and to provide direction and ideas. I would also like to thank the Eastman Kodak Company for material support; images, cameras, and test equipment, and for access to their experts in the field of imaging science.

## DEDICATION

To Katinka, Natascha, Kevin, and Anna, I love you all.

**Validation of Rochester Institute of Technology's (RIT's)  
Digital Image and Remote Sensing Image Generation (DIRSIG) Model -  
Reflective Region**

by  
Russell A. White

Submitted to the Chester F. Carlson Center for Imaging Science  
in partial fulfillment of the requirements  
for the Maser of Science Degree  
at the Rochester Institute of Technology

**Abstract**

The performance of RIT's Digital Imaging and Remote Sensing Image Generation (DIRSIG) model is validated. The model is robust enough to treat solar, atmospheric, target/background, and sensor interactions. It operates over the 0.28 - 28  $\mu\text{m}$  (Ultraviolet - Long Wavelength Infra-Red) spectral region. However, this study focuses only on the 0.4 - 1.0  $\mu\text{m}$  (reflective) region. To validate the model, reference (actual) imagery from an airborne frame sensor is compared to synthetic imagery of the same scene. This study also evaluates DIRSIG's treatment of reflectivity and recommends improvements.

# Table of Contents

Abstract .....	v
Table of Contents .....	vi
List of Figures .....	ix
List of Images .....	xii
List of Tables .....	xiii
1.0 Introduction .....	1
2.0 Objectives and Technical Approach .....	2
3.0 Background Literature Review .....	3
3.1 Why Do Synthetic Image Generation? .....	3
3.2 The Imaging Chain and the Big Equation .....	4
3.3 Synthetic Image Generation Model Review .....	8
3.4 DIRSIG Review .....	13
3.5 A Review of Efforts to Validate SIG Models .....	23
3.6 Reflectivity Review .....	25
3.6.1 Definition .....	26
3.6.2 Reflectivity Models .....	27
3.6.3 Source Data for Reflectivity Models .....	37
3.6.4 Material Reflectivity in Actual Imagery .....	42
3.6.5 DIRSIG's Treatment of Reflectivity .....	42
4.0 Experimental .....	46
4.1 Scene Selection .....	46
4.2 Scene Creation Process .....	48
4.2.1 Training .....	48
4.2.2 Scene Creation Environment .....	49
4.2.3 Creation of Scene Database Files .....	49

4.2.3.1	Creation of the Geometric Database (.gdb file) ....	51
4.2.3.2	Creation of the Look Angle File (.adv file) .....	70
4.2.3.3	Creation of the Scene Node File (.snd file) .....	71
4.2.3.4	Creation of the Radiosonde Data File (.rsd file)	72
	.....	
4.2.3.5	Creation of the LOWTRAN Card Deck (.cdk file) .....	76
4.2.3.6	Creation of the Weather File (.wth file) .....	80
4.2.3.7	Creation of the Radiance Files (.rad# files) .....	85
4.2.3.8	Creation of the Materials File (.mat file) .....	86
4.2.3.9	Creation of the Emissivity Files (.ems files) .....	88
4.2.3.10	Creation of the Sensor Files (.sen files) .....	101
4.2.3.11	Creation of the Extinction Coefficient Files (.ext files) .....	102
4.2.3.12	Creation of the Batch File (.bat file) .....	103
4.2.4	Running DIRSIG .....	105
4.3	Adjusting Parameters in the Synthetic Image .....	105
4.4	The Reference Imagery Acquisition Process .....	105
4.4.1	Aerial Film Imagery Acquisition Process .....	105
4.4.2	Aerial Digital Imagery Acquisition Process .....	106
4.5	The Scene Validation .....	107
4.5.1	Validation Process .....	107
4.5.2	Validation in the Nadir Perspective .....	108
4.5.3	Validation in the Oblique Perspective .....	116
5.0	Reflectance Model .....	125
5.1	Sensitivity Analysis .....	125

5.1.1	Simple Sensitivity Analysis of the Big Equation (Visible Spectrum) .....	125
5.1.2	Sensitivity Analysis of DIRSIG's Big Equation (Visible Spectrum) - DIRSIG .....	137
5.1.3	Sensitivity Analysis of the Reflectivity Model .....	147
5.1.4	Recommendations for Modifying .....	151
5.2	Proposed Model .....	152
5.2.1	Basis and Structure of the Proposed Model .....	152
5.2.2	Inputs to the Model .....	166
5.2.3	Incorporation into DIRSIG .....	166
5.2.4	Sensitivity Analysis of the Proposed Model .....	178
5.2.5	Topography, Material, and Texture Maps .....	185
5.2.5.1	Topography Maps .....	185
5.2.5.2	Material Maps .....	188
5.2.5.3	Texture Maps .....	189
6.0	Summary .....	190
7.0	References .....	191
8.0	Appendices .....	194
A	WSO Data .....	195
B	Solid Angle Computation .....	197
	Obtaining Specularity Data .....	198

## List of Figures

<u>Figure</u>	<u>Title</u>	<u>Page</u>
3.1	Typical Imaging Chain .....	5
3.2	Radiance originating at the sun .....	6
3.3	Imagery Simulation Facility Schematic Diagram .....	9
3.4	DIRSIG flow chart .....	14
3.5	Solar Radiance and Atmospheric transmission coefficient .....	16
3.6	Upwelled Radiance .....	17
3.7	Downwelled Radiance .....	18
3.8	DIRSIG Ray Tracer Flow .....	19
3.9	DIRSIG Ray Tracer Flow (continued) .....	20
3.10	Reflectivity Characteristics .....	27
3.11	Lambertian Reflectivity .....	29
3.12	Phong Reflectivity .....	30
3.13	Model Angles .....	32
3.14	Angles for Culpepper's model .....	33
3.15	Culpepper's model .....	33
3.16	White's model (proposed) .....	35
3.17	Sampling due to ray-tracing .....	36
3.18	The impact of shape factor .....	37
3.19	Bi-Directional Reflectance .....	38
3.20	Hemispherical Reflectance .....	39
3.21	Hemispherical Reflectance without specular lobe .....	40
3.22	PLIN setup .....	41
3.23	DIRSIG reflectivity model - specular .....	43
3.24	DIRSIG reflectivity model - diffuse .....	43
3.25	DIRSIG Sampling .....	44
4.1	Map of the target area .....	47
4.2	Land Use information obtained from the City of Rochester .....	52
4.3	Area objects of the scene .....	54
4.4	Scene Hierarchy - numbers in the parentheses indicate quantity .....	55
4.5	Digitized Topography Lines .....	57
4.6	Land Forming .....	58
4.7	Alternative topography creation approach .....	59
4.8	Fancy House .....	60
4.9	Garage .....	60
4.10	House 1 .....	60

4.11	House 2 .....	60
4.12	Insertion of house using the land use data as a template .....	61
4.13	House 144 .....	62
4.14	House 146 .....	62
4.15	House 157 .....	63
4.16	House 303 .....	63
4.17	Streets in Region 41 .....	64
4.18	Sidewalks in Region 41 .....	65
4.19	Parking Lots in Region 41 .....	65
4.20	Tree - side view .....	66
4.21	Tree - top view .....	66
4.22	Sedan .....	66
4.23	Pick-up Truck .....	66
4.24	Mini-Van .....	66
4.25	Driving Park Bridge, taken from Jim Salacain's Thesis Work .....	67
4.26	Hawkeye Plant, taken from Jim Salacain's Thesis work .....	69
4.27	Sample .adv file .....	70
4.28	.snd file .....	71
4.29	.rsd file .....	75
4.30	LOWTRAN Input .....	79
4.31	.cdk file .....	80
4.32	.wth file .....	83
4.33	Part of a .rad file .....	85
4.34	Part of the materials file .....	87
4.35	A sample emissivity file .....	89
4.36	ref% sheet from a DB renais file .....	96
4.37	"ems" sheet from a DB renais file .....	97
4.38	"emsfiles" sheet .....	98
4.39	ems file curves for 5 samples (1a, 1b, 2a, 2b, 3a) .....	99
4.40	Reflectivity curves for the same samples above .....	99
4.41	Spectral Response of the DCS 420 Camera .....	101
4.42	.sen file .....	102
4.43	.bat file .....	104
4.44	Histogram of Reference Image, Red Band .....	111
4.45	Histogram of Reference Image, Green Band .....	111
4.46	Histogram of Reference Image, Blue Band .....	112
4.47	Histogram of Reference Image, Combined Bands .....	112
4.48	Histogram of Synthetic Image, Red Band .....	113
4.49	Histogram of Synthetic Image, Green Band .....	113

4.50	Histogram of Synthetic Image, Blue Band .....	114
4.51	Histogram of Synthetic Image, Combined Bands .....	114
4.52	Histogram of Reference Image, Red Band .....	120
4.53	Histogram of Reference Image, Green Band .....	120
4.54	Histogram of Reference Image, Blue Band .....	121
4.55	Histogram of Reference Image, Combined Bands .....	121
4.56	Histogram of Synthetic Image, Red Band .....	122
4.57	Histogram of Synthetic Image, Green Band .....	122
4.58	Histogram of Synthetic Image, Blue Band .....	123
4.59	Histogram of Synthetic Image, Combined Bands .....	123
5.1	Base Case Radiance and Reflectance Maps .....	126
5.2	Case 2a Radiance and Reflectance Maps: No specular reflectance, initial setup .....	129
5.3	Case 2b Radiance and Reflectance Maps: Specular Bounce direction changed (Sun moved to nadir.) .....	129
5.4	Case 3a Radiance and Reflectance Maps: No downwelled Radiance .....	131
5.5	Case 3b Radiance and Reflectance Maps: Shape Factor is 0.5 and sun at nadir. ....	132
5.6	Case 3c and 3d Radiance and Reflectance Maps: Shape Factor is 0.5 and sun at 45 degrees. ....	133
5.7	Case 3e Radiance and Reflectance Maps: Reflectance reduction at high zenith angles. sun at nadir. ....	134
5.8	Case 4 Radiance and Reflectance Maps: Reflectance reduction at High Oblique View Angles. ....	136
5.9	Sensitivity Analysis Setup .....	142
5.10	BDRF of target material .....	142
5.11	Sensitivity Analysis Setup .....	147
5.12	Radiance map above a facet .....	152
5.13	Reflectance map for one wavelength and one viewing angle .....	153
5.14	Actual reflectivity of the sample .....	156
5.15	DIRSIG delta function model of the specular lobe .....	157
5.16	Cone model of the specular lobe .....	157
5.17	Cosine model of the specular lobe .....	158
5.18	Exponential model of the specular lobe .....	159
5.19	Interpolated data model of the specular lobe .....	160

5.20	Proposed Ray-Tracer Flow .....	162
5.21	Proposed Ray-Tracer Flow (continued) .....	163
5.22	Proposed emissivity database (.ems file) structure .....	167
5.23	Reference Angles .....	169
5.24	Basic Golf Ball .....	172
5.25	Golf Ball Matrix 1 .....	173
5.26	Golf Ball Matrix 2 .....	174
5.27	Golf Ball Matrix 3 .....	175
5.28	Call Emissivity Output .....	176
5.29	Surface Topography - lower resolution .....	186
5.30	Surface Topography - higher resolution .....	186
5.31	Topographical Map .....	188

## List of Images

<u>Image</u>	<u>Title</u>	<u>Page</u>
4.1	Aerial Image of the target area .....	48
4.2	Typical House 1 .....	60
4.3	Typical House 2 .....	60
4.4	Nazareth Hall School .....	62
4.5	Rochester School for the Deaf .....	62
4.6	Walter Hall .....	63
4.7	Rochester School for the Deaf .....	63
4.8	Driving Park Bridge .....	68
4.9	Kodak Hawkeye Plant .....	69
4.10	X-Rite 938 spectrodensitometer .....	91
4.11	Experimental Setup .....	92
4.12	Nadir reference Image .....	109
4.13	Nadir synthetic Image .....	109
4.14	Oblique reference Image .....	117
4.15	Oblique synthetic Image .....	118

## List of Tables

<u>Table</u>	<u>Title</u>	<u>Page</u>
4.1	Databases required by DIRSIG .....	50
4.2	Material Attributes .....	56
4.3	Flyover Radiosonde Data .....	74
4.4	Actual wavenumbers Assigned .....	94
4.5	Validation Results, nadir .....	110
4.6	Validation Results, oblique .....	119
5.1	Estimate Error Calculation Results .....	128
5.2	No Specular Reflectance Error Calculation Results .....	130
5.3	Downwelled Radiance and Shape Factor Error Calculation Results ....	135
5.4	High Oblique Viewing Angle Error Calculation Results .....	137
5.5	Error Variable Values .....	141
5.6	Case 1 Sensitivity Analysis .....	145
5.7	Case 2 Sensitivity Analysis .....	146
5.8	Case 3 Sensitivity Analysis .....	149
5.9	Case 4 Sensitivity Analysis .....	150
5.10	Error Variable Values .....	179
5.11	Case 1a Sensitivity Analysis .....	181
5.12	Case 1b Sensitivity Analysis .....	182
5.13	Case 1c Sensitivity Analysis .....	183
5.14	Case 1d Sensitivity Analysis .....	184

## 1.0 Introduction

This study validates the performance of RIT's Digital Imaging and Remote Sensing Image Generation (DIRSIG) model. The purpose of the study is to further validate remote sensing imaging systems modeling techniques and ultimately to further the understanding of the science of remote sensing itself. DIRSIG attempts to generate radiometrically accurate images for use in passive remote sensing applications. The model is robust enough to treat solar, atmospheric, target/background, and sensor interactions. It operates over the 0.28 - 28  $\mu\text{m}$  (Ultraviolet - Long Wavelength Infra-Red) spectral region, however, this study will focus only on the 0.4 - 1.0  $\mu\text{m}$  (reflective) region. This study also evaluates DIRSIG's treatment of reflectivity and recommends improvements.

DIRSIG's radiometric performance in the reflective region was baselined by Stark in 1993. Since his validation the following modifications have been made to DIRSIG.

- The radiometry submodel has been improved. The model can now simulate targets that have specular and diffuse reflectance components, surface texture, and transmissive objects such as clouds and vegetation (trees). A newer version of the atmospheric model LOWTRAN, called MODTRAN, has also been incorporated.
- The sensor submodel can now handle frame cameras, line scanners, and pushbroom scanners.
- Runtime improvements and software corrections have been made.

Each modification has been independently validated. However, the magnitude and number of modifications dictate that an overall revalidation be accomplished. This study will provide that overall revalidation using an approach similar to Stark's. Reference

(actual) imagery will be compared to synthetic imagery of the same scene. The reference images will include multiple perspectives from an airborne frame sensor.

The second part of this study evaluates DIRSIG treatment of reflectivity. A common task of SIG models is to determine how a given image would look from different perspectives. For example, a military user may have a satellite photo of a scene and want to know how the scene would look to an aircraft ingressing for a strike. The ability of the SIG model to accurately generate these images could be critical to mission success. Based on sensitivity analysis, recommendations are made to improve the efficiency of adjusting material reflectivity to generate more radiometrically accurate imagery.

## **2.0 Objectives and Technical Approach**

The first objective of this study is to revalidate the radiometric performance of DIRSIG in the 0.4-1.0 $\mu\text{m}$  spectral (reflective) region. To accomplish this objective, the following tasks were performed.

- Literature reviews of DIRSIG and other SIG models and of SIG validation methods were conducted.
- Aerial reference images that had the following qualities were acquired.
  - a. Aerial access to the target area was available for imaging.
  - b. Ground access to the target area was available for truth data collection.
  - c. Atmospheric data was available for input to LOWTRAN.
  - d. Sensor system characteristics were available.
  - e. Emissivity data was available for the materials in the scene.
- A synthetic image of the scene using DIRSIG was generated.

- The synthetic (DIRSIG) and reference images were compared using Root Mean Square (RMS) and Rank Order Correlation (ROC) techniques.

The second objective of this thesis is to evaluate DIRSIG's treatment of reflectivity and to develop methods for efficiently adjusting reflectivity values. The goal is to develop methods that are applicable to the situation described in the introduction, changing perspectives. To accomplish this objective, the following tasks were performed.

- A literature review of methods for modeling material reflectivity and how they are implemented in SIG models was conducted.
- Sensitivity analyses of the radiance reaching the sensor and the parameters affecting reflectivity were performed.
- Based on the sensitivity analyses, recommendations were made regarding which reflectivity parameters should be adjusted first to maintain radiometric accuracy as perspectives change.
- The recommendations were used to “manually” adjust the reflectivity values of several materials in a scene to accommodate different perspectives to validate the method.
- Changes to DIRSIG's current reflectivity model were recommended.

The accomplishment of these tasks should contribute to the understanding of how to model remote sensing imaging systems and ultimately to further the understanding of the science of remote sensing itself.

### **3.0 Background Literature Review**

Before beginning the validation, several questions need to be addressed. Questions like: Why do SIG? What is remote sensing? What is a typical SIG model? What is DIRSIG? Why valid DIRSIG in particular? How do you validate a SIG model? What is the nature of reflectivity? How is it modeled? These questions are addressed in this section.

### **3.1 Why do Synthetic Image Generation?**

A remote sensing satellite can cost between 50 million and a billion dollars to build and over 100 million dollars to put into orbit. Once in orbit correcting flaws is almost impossible. The satellite must be built right the first time. Traditional methods of building it right the first time have included expensive and extensive physical prototyping and testing. With the decreasing cost of computers and their increasing availability and power, computer modeling has become a cost effective alternative. This is also true for less expensive aerial remote sensing systems. The models use the satellite or aircraft remote sensing system design parameters, target models, and expected suite of imaging conditions to generate images that the envisioned system will produce operationally. By adjusting the design parameters and analyzing the model's output, engineers are able to determine how to build it right the first time.

SIG models can also be used to manage the resources by giving the user of an imaging system an ability to visualize images before they are actually acquired. By analyzing those images, the user can determine the minimum acceptable conditions for image acquisition. This gives the manager of the resource maximum flexibility in satisfying imaging requirements.

Another important use of synthetic image generators is in parametric studies. SIG models allow researchers to evaluate the impact of changing a single parameter, which is impractical, if not impossible, to do for actual collections. This of particular importance

when the Signal to Noise Ratio (SNR) of the parameter of interest is low or is sensitive to the imaging conditions, i.e. correlated to another parameter. In SIG models, all the parameters can be controlled.

### 3.2 The Imaging Chain and the Big Equation

Before various models are discussed, it is useful to describe what we are attempting to model. The process of generating an image can be thought of as chain of smaller processes. A typical imaging chain for passive remote sensing is shown in Figure 3.1.

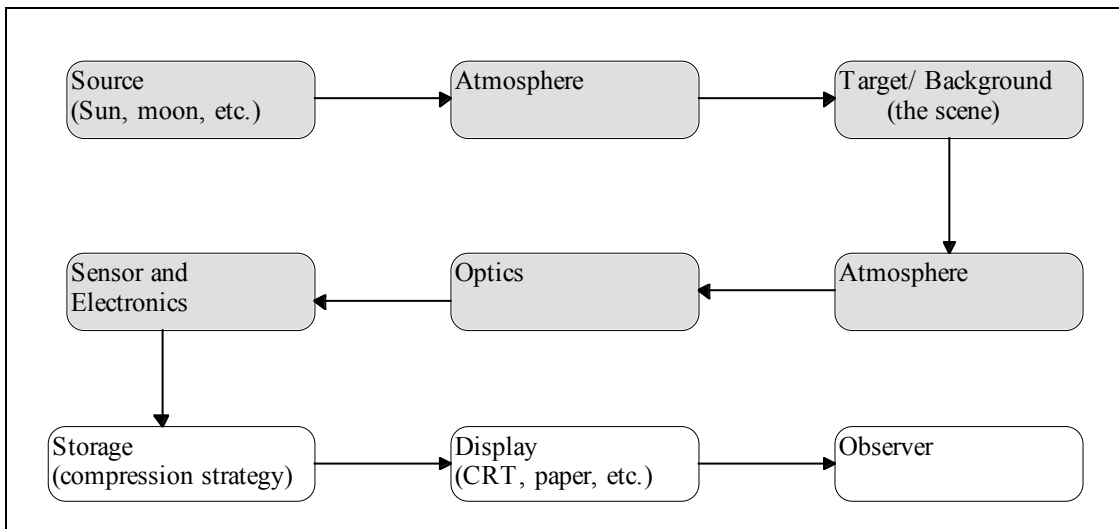


Figure 3.1 Typical Imaging Chain

SIG models generally take one of two approaches to modeling the imaging chain. The first approach is to model one link of the chain in as much detail as possible. The remaining parts of the chain are left to be modeled by others or are modeled with less rigor. The second approach is to model as much of the imaging chain as possible. The models of significance to this study generally model the shaded links in Figure 3.1.

DIRSIG is an example of this approach. It treats the source, atmosphere, target and background, and sensor links of the chain and their interactions.

DIRSIG's model is based on first principles. It begins with a governing equation for the radiance reaching the sensor. The equation accounts for all significant sources of radiation and their various paths to the sensor. Using inputs to the equation and the sensor response, it computes final image pixel values (digital count).

In remote sensing the governing equation for the imaging process is often called the "Big Equation" (Schott, 1997). The Big Equation accounts for all the radiance reaching the sensor. In one form or another, it is incorporated into all the models discussed in the next section. It is shown pictorially in Figure 3.2. There are generally four significant sources of photons in the visible/NIR spectral region.

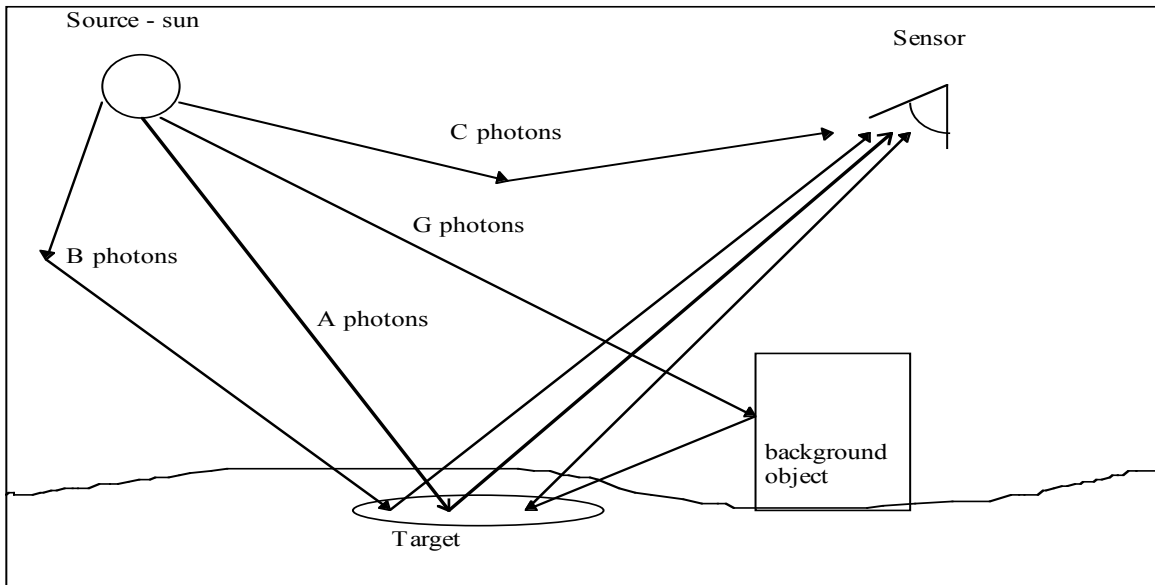


Figure 3.2. Radiance originating at the sun. The notation conventions used here follow those used by Schott (1997.)

Mathematically, the Big Equation is given by

$$L_{\lambda} = A_{photons} + B_{photons} + C_{photons} + G_{photons}$$

where

- $L_{\lambda}$  - total radiance reaching the sensor [ $\text{W}/\text{cm}^2\text{sr}^{-1}$ ]
- $A_{photons}$  - radiance that originates at the sun, passes through the atmosphere, is reflected by the target, and passes through the atmosphere to the sensor
- $B_{photons}$  - radiance that originates at the sun, is scattered by the atmosphere to the target, is reflected by the target, and then passes through to atmosphere to the sensor. It is commonly called skylight or downwelled radiance.
- $C_{photons}$  - radiance that originates at the sun and is reflected by the atmosphere to the sensor. It is commonly called upwelled radiance
- $G_{photons}$  radiance that originates at the sun, passes through the atmosphere, is reflected by background objects to the target, is reflected by the target, and then passes through the atmosphere to the sensor

Substituting expressions for the  $L_A$ ,  $L_B$ ,  $L_C$ , and  $L_G$ , using Schott's (1997) notation and conventions, gives

$$L_{\lambda} = \frac{E'_{s\lambda}}{\pi} \cos \sigma' \tau_1(\lambda) r(\lambda) \tau_2(\lambda) + FL_{ds\lambda} r_d(\lambda) \tau_2(\lambda) + L_{us\lambda}(\theta, \phi) + (1 - F)L_{bs\lambda} r_d(\lambda) \tau_2(\lambda)$$

where

- $\frac{E'_{s\lambda}}{\pi}$  - exoatmospheric radiance onto a surface perpendicular to the incident beam [ $\text{W}/\text{cm}^2\text{sr}^{-1}$ ]
- $\cos \sigma'$  - accounts for the off axis angle between  $E_{s\lambda}$  and the target [unitless]
- $\tau_1(\lambda)$  - atmospheric transmission coefficient along the sun-target path [unitless]

- $r(\lambda)$  - reflectance of the target [unitless]
- $\tau_2(\lambda)$  - atmospheric transmission coefficient along the target-sensor path [unitless]
- $F$  - fraction of the hemisphere above the target that is sky [unitless]
- $L_{ds\lambda}$  - downwelled radiance [ $\text{W}/\text{cm}^2\text{sr}^{-1}$ ]
- $r_d(\lambda)$  - reflectance of a diffuse target [unitless]
- $L_{u\hat{s}\lambda}(\theta, \phi)$  - upwelled radiance [ $\text{W}/\text{cm}^2\text{sr}^{-1}$ ]
- $(1 - F)$  - fraction of the hemisphere above the target that is background (not sky) [unitless]
- $L_{b\hat{s}\lambda}$  - radiance from the background [ $\text{W}/\text{cm}^2\text{sr}^{-1}$ ]

Once the radiance's are traced along their paths to the sensor, the impact of the sensor is incorporated.

$$\bar{L} = \int_0^\infty L_\lambda \bar{R}(\lambda) d\lambda$$

where

- $\bar{L}$  - the effective radiance reaching the sensor
- $\bar{R}$  - normalized response of the sensor

How that it is understood what the models are attempting to model, a description of how they attempt to model it is represented. The models described below show that the approaches vary, sometimes significantly.

### 3.3. Synthetic Image Generation Model Review

SIG models that attempt to produce radiometrically accurate images have been around since the 1970's. The number of models and their complexity has increased with the availability of cheaper and more powerful computers. Earlier simplifications of the governing equations are giving way to detailed models of each link in the chain and their interactions. In addition, the relative ease of developing a model compared to the past has enabled less capitalized research groups to enter the field. Just as important, modifications to user interfaces are allowing the models to be used productively by less technically oriented users.

There are two basic approaches used to create radiometrically accurate SIG models, physical models and computer models. Both approaches require the input of many parameters such as weather, spatial relationships, and material data. However, how those parameters are incorporated is very different for each approach. In physical modeling, the input parameters are incorporated into a miniaturized scene. In computer modeling, the input parameters are described and contained in database files.

The setup for the Itek Corporation's physical SIG model is shown in Figure 3.3 (Maver, 1993).

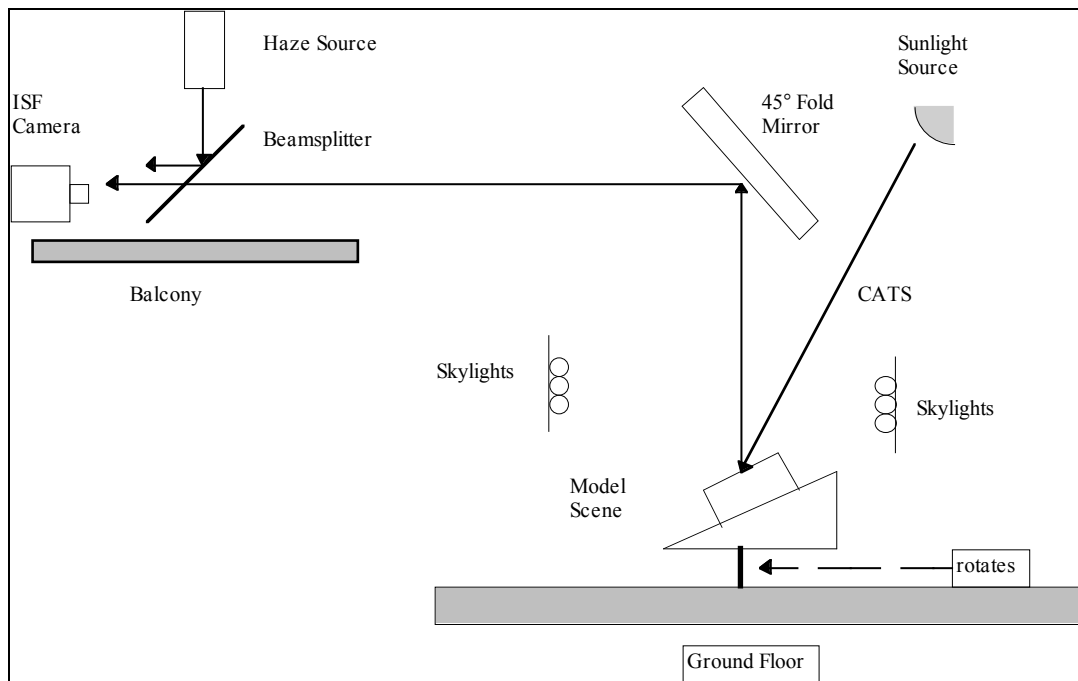


Figure 3.3. Image Simulation Facility Schematic Diagram. Itek Optical Systems.

The model scene is placed on a platform that allows its orientation relative to the camera to be adjusted. Radiation sources are provided by artificial lighting, both solar and downwelled sources are simulated. Atmospheric interactions are simulated by combining the reflected radiation with a haze source. The scene is then imaged with a camera system. Francis (1993) has shown that this approach is quite effective in producing “realistic” visible imagery. However, the approach is limited by its technology. Because the scene is a physical model, it forces the remaining parts of the model to be physical as well. Physically simulating some of these parts, such as the atmosphere, is difficult if not impossible since some physical properties do not scale linearly with respect to physical dimensions. In addition, physical modeling defeats one of the main purposes of modeling, the elimination of expensive prototyping of the imaging system. Post processing to include these effects would require computer modeling, something physical modeling attempts to minimize. This is not to say that physical modeling is not useful.

Currently, it reproduces features of real imagery, such as spatial relationships, with much better fidelity than computer generated imagery.

The other approach to creating synthetic images is to generate the images entirely through computer modeling. To accomplish this, the process begins with a three dimensional geometric mathematical representation of the scene. Objects in the scene are then assigned material properties. Next, atmospheric conditions, sources of radiation, and the sensor characteristics are determined. All of this information is stored in databases. The databases can be extensive or limited depending on the requirements of the model and the application. The last step is to compute the radiance reaching the sensor. A common technique used for this task is ray-tracing. In ray-tracing, the radiation reaching the sensor is traced backwards from the sensor to the objects in the scene and then to the radiation sources.

Brief overviews of some representative computer models are given below with a more detailed description of DIRSIG provided in the next section.

TAV-IR (The Advanced Visualizer - Infra-Red)

Wavefront Technologies -- Santa Barbara, California

TAV-IR (Henry, 1994) was originally built for the Navy to help evaluate pilot vision through aircraft canopies. Synthetic images are treated as input to models of potential canopy material. Scenes are created in a graphics package and the objects are assigned material properties. Sources of radiation and the sensor characteristics are then input. It is interesting to note that this model includes a model of the sensor response of the eye. No information was available on how TAV-IR models the atmosphere. Computation of the final pixel values uses a ray-tracing approach. The model is advanced enough to

address the directional nature of reflectivity. Unfortunately, no validation information has been published concerning the model's radiometric accuracy.

CREATION (Computer-generation of Realistic Environments with Atmospheres for Thermal Imagery with Optics and Noise)

US Army CECOM Center for Night Vision and Electro-Optics -- Fort Belvoir, VA

CREATION (Kornfeld, 1989) was developed by the Army to help evaluate the effectiveness of proposed Forward Looking Infrared (FLIR) Sensors. The synthetic images are used as input to automatic target recognizers (ATRs) and sensor models. The first step in generating images is the creation of insertion objects, mainly tanks and trees, and the background. An atmospheric attenuation is then applied separately to the background and the insertion objects. A LOWTRAN 6 equivalent is used for this task. Next, the objects and the background are merged using weights to establish translucency. If the task is to evaluate an ATR, the images are then degraded according to sensor models. Again, no validation results have been published.

GTVISIT (Georgia Tech Visible and Infrared Synthetic Imagery Testbed)

Georgia Institute of Technology -- Atlanta, Georgia

GTVISIT (Cathcart, 1988) was developed to support "research activities ranging from performance studies of human observers to the development of feature extraction algorithms." Thus its main distinction relative to other models is its flexibility. Like the generic model, it begins with a geometric description of the scene. It then assigns attributes to elements in the scene using material databases. Next, GTVISIT uses a Z-buffering algorithm instead of ray-tracing to determine pixel values. Z-buffering is a technique used to project a three-dimensional scene onto a two-dimensional surface.

Finally, atmospheric attenuation and sensor models are incorporated. Again, no validation results have been published.

These model descriptions must be considered temporary. The developers are continually modifying the models as the demands on them increase and change. If the model began in the IR region, it will probably model the visible region before long. Likewise, if the model began in the visible region, it will probably soon model the IR region. While the models are increasing in complexity, many are adding Graphical User Interfaces to make them easier to use. This is an important development because it will allow those with minimal technical background to productively use them. As their use increases, the demands on the models will likewise increase. The changes in the next ten years should be truly remarkable. To track the developments and to obtain more detailed information about the models, the reader is directed to the yearly Society of Photo-Optical Instrumentation Engineers (SPIE), International Society for Optical Engineers conference on models and related topics.

Of all these models, why focus on a review and validation of DIRSIG? There are a number of reasons. DIRSIG uses a first principles approach. This allows a complete investigation of the impact of a change in a single parameter on the final image. The model treats the effects of each parameter with great rigor by minimizing simplification and broad assumptions whenever feasible. Detailed descriptions of how DIRSIG works are available, allowing a thorough analysis of its workings and performance. This is not true for many models. DIRSIG is available, currently free, allowing for the maximum research for the minimum amount of funding. The performance of DIRSIG has been documented and published. This is important for several reasons. First, it establishes a performance metric by which other models can be compared and second it establishes an acceptable validation method. Finally, based on a review of many models, DIRSIG is on the cutting edge of technology for remote sensing applications.

### **3.4 DIRSIG Review**

DIRSIG was originally developed at RIT in the early 1980's to study the absolute radiometric calibration of Thermal Infrared Imagery (TIR) with a special interest in correction for atmospheric effects (Schott, 1991). It has grown since then to model the imaging chain from the source through the sensor and to cover both the visible and IR spectral bands (0.28  $\mu\text{m}$  - 28  $\mu\text{m}$ ). Throughout its development special efforts have been made to ensure that the outputs are radiometrically correct, this includes publishing validation results.

As stated previously, DIRSIG is a completely computerized synthetic image generator. It is organized similarly to the generic model described above. Scene generation begins with the construction of a geometric representation of the scene. DIRSIG uses AutoCAD (Autodesk, 1989) for this purpose because of its wide availability, low cost, and product support. During the building of the geometric representation, some material attributes are assigned to the objects that comprise the scene. Files containing sensor characteristics, atmospheric data, material emissivity data, and other input data are then created. Once the databases have been populated, DIRSIG is executed. DIRSIG uses a ray-tracing approach to compute radiance reaching the sensor per incremental bandpass. The incremental values are then combined into the number of bands the sensor is sensitive to. Figure 3.4 shows this process pictorially.

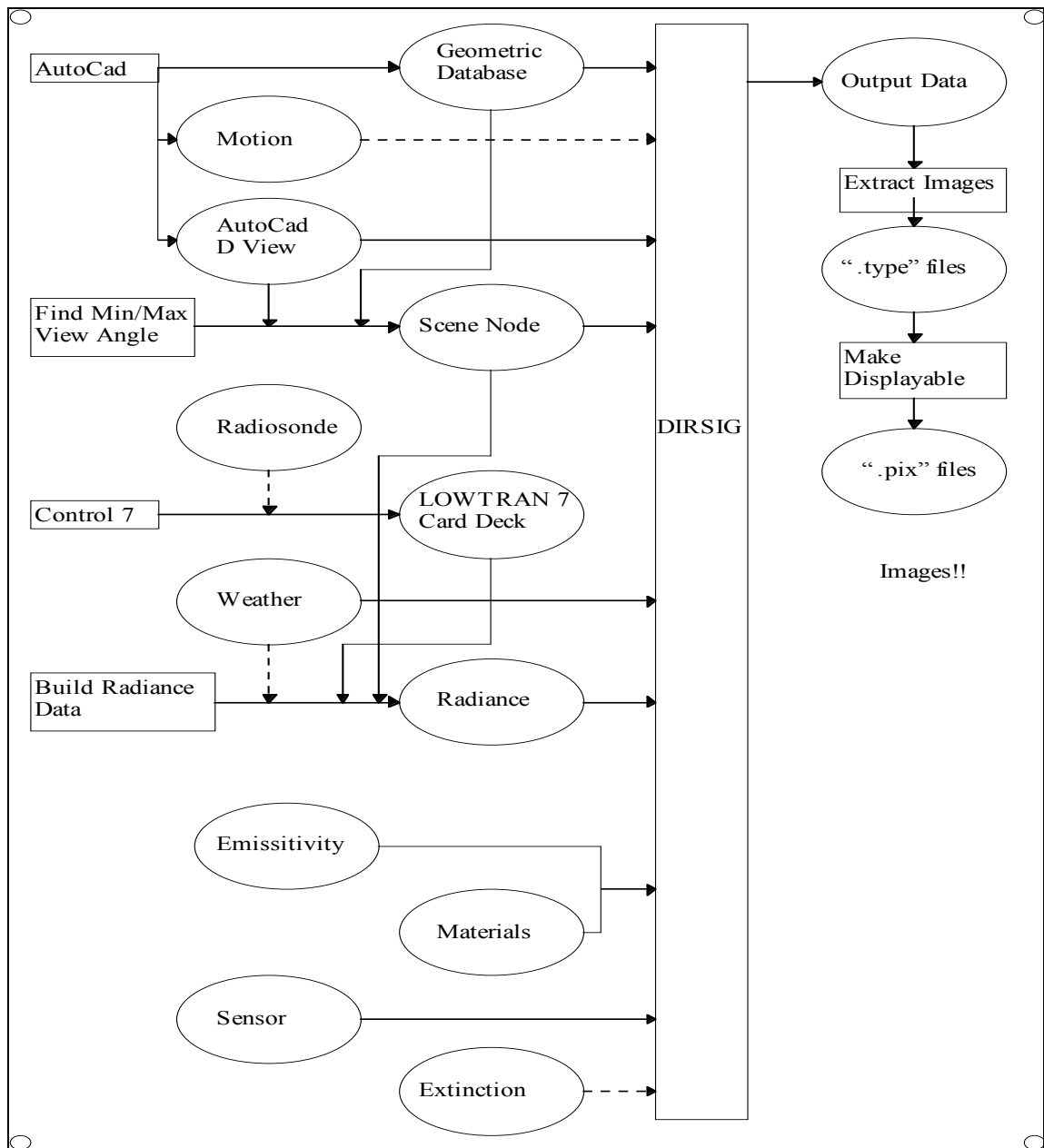


Figure 3.4. DIRSIG flow chart. Files are shown in ellipses. Programs are shown in rectangles. Optional input arguments are indicated with dashed lines (Schott, 1993).

Each of the submodels are reviewed below.

### Geometric Submodel

The geometric submodel, using ACAD, creates a description, via a database, of the scene to be simulated. The scene is composed of objects, which are composed of parts, which are composed of facets, which are the basic working elements. Each facet is described in terms of its spatial and material parameters. The spatial (or geometric) parameters include the location of the vertices, the normal to the surface, slope angle, and azimuth angle. The material parameters include temperature, self-generated power, specific heat, thermal conductivity, mass density, specularity, visible emissivity, thermal emissivity, exposed area, thickness, optical description (opaque or transmissive), emissivity (file name), texture (file name), and extinction coefficient (file name). Most of the material parameters are required for the thermal submodel and therefore are not of interest to this study. Parameters of interest include specularity, emissivity, texture, and extinction coefficient.

### Radiometry Submodel

The radiometric submodel computes the solar radiance, atmospheric transmission coefficients, upwelled radiance, and downwelled radiance. The submodel is built around the US Air Force's MODTRAN (LOWTRAN) atmospheric propagation model (Kneizys, 1988). MODTRAN (Berk, 1989) is a very detailed model that accounts for atmospheric factors that can attenuate the radiance reaching the sensor. It is widely used and the results have been thoroughly validated.

The solar radiance ( $E_s$ ) and the atmospheric transmission coefficient ( $t_1$ ) are computed spectrally. This is illustrated in Figure 3.5.

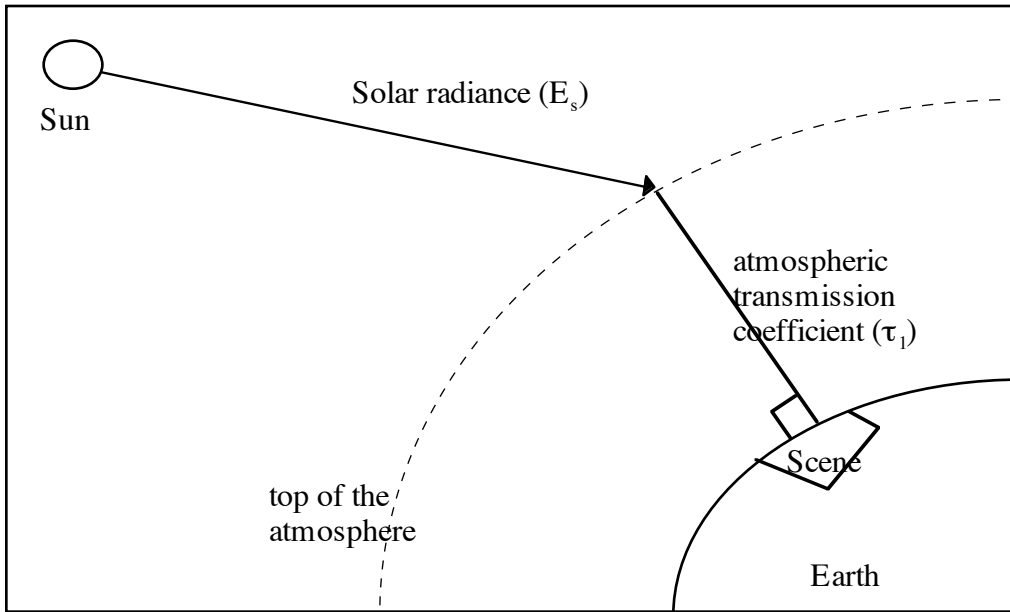


Figure 3.5. Solar Radiance and Atmospheric transmission coefficient.

The upwelled radiance and the sensor/target transmission coefficients are computed spectrally over the field-of-view of the sensor that covers the scene. Typically, the values are computed at two degree increments. A circular symmetry is assumed. This is illustrated in Figure 3.6.

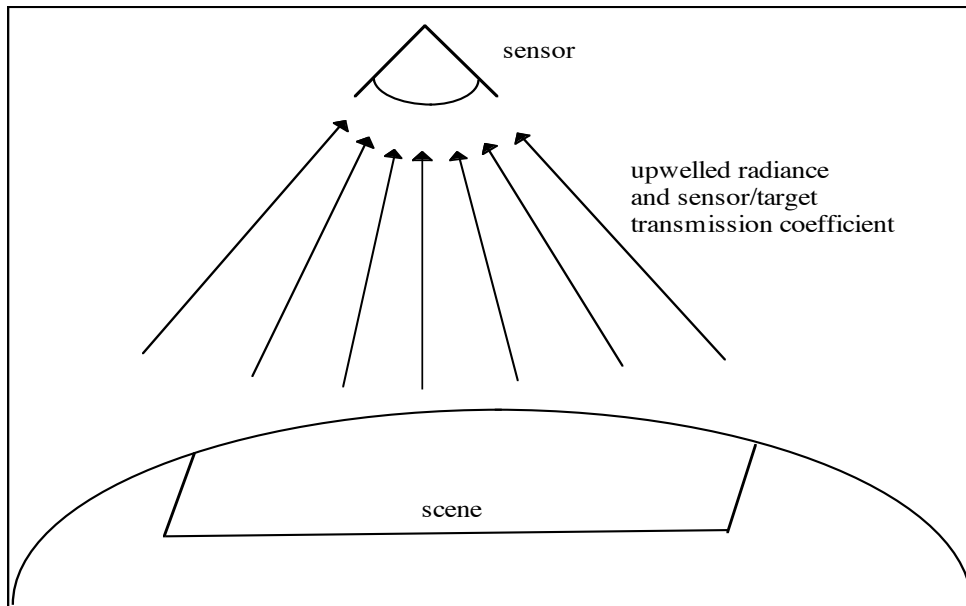


Figure 3.6. Upwelled Radiance

While circular symmetry (no variation as a function of azimuth) is convenient computationally it does not reflect reality and produces increasing errors as the field of view of the sensor increases. This asymmetry is more pronounced as the specular bounce to the sun nears and enters the field of view of the sensor. The scene builder must be aware of this limitation when building a scene with these imaging conditions.

The downwelled radiance is computed spectrally over the hemisphere above the center of the scene. Values are computed at 30 degree azimuth and 15 degree elevation intervals. This is illustrated in Figure 3.7.

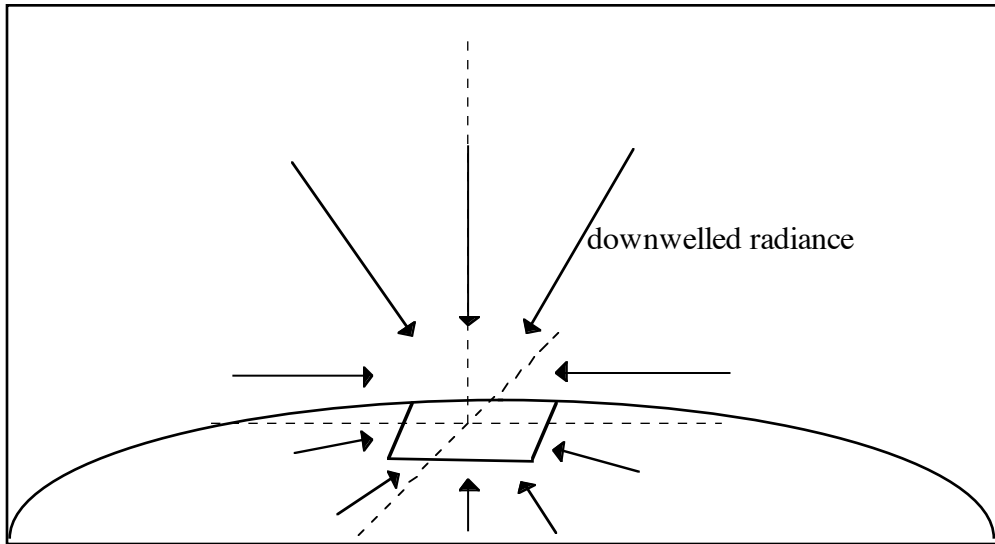


Figure 3.7. Downwelled Radiance.

### Ray-Tracer Submodel

The main task of the ray-tracer submodel is to map a two-dimensional view of the three-dimensional scene. To do this, the submodel retraces the radiance reaching each pixel of the sensor back to its source(s). The second task of the ray-tracer is to guide the scene creation process by calling the other submodels at the proper times and directing data flow. The algorithm flow is shown pictorially in Figure 3.8 and 3.9.

Before the ray-tracing begins, DIRSIG determines bounding volumes for each object and part to help with the ray tracing. The bounding volumes reduce the overall processing time by limiting intersection testing to only those facets that are within the first bounding volume the ray intersects.

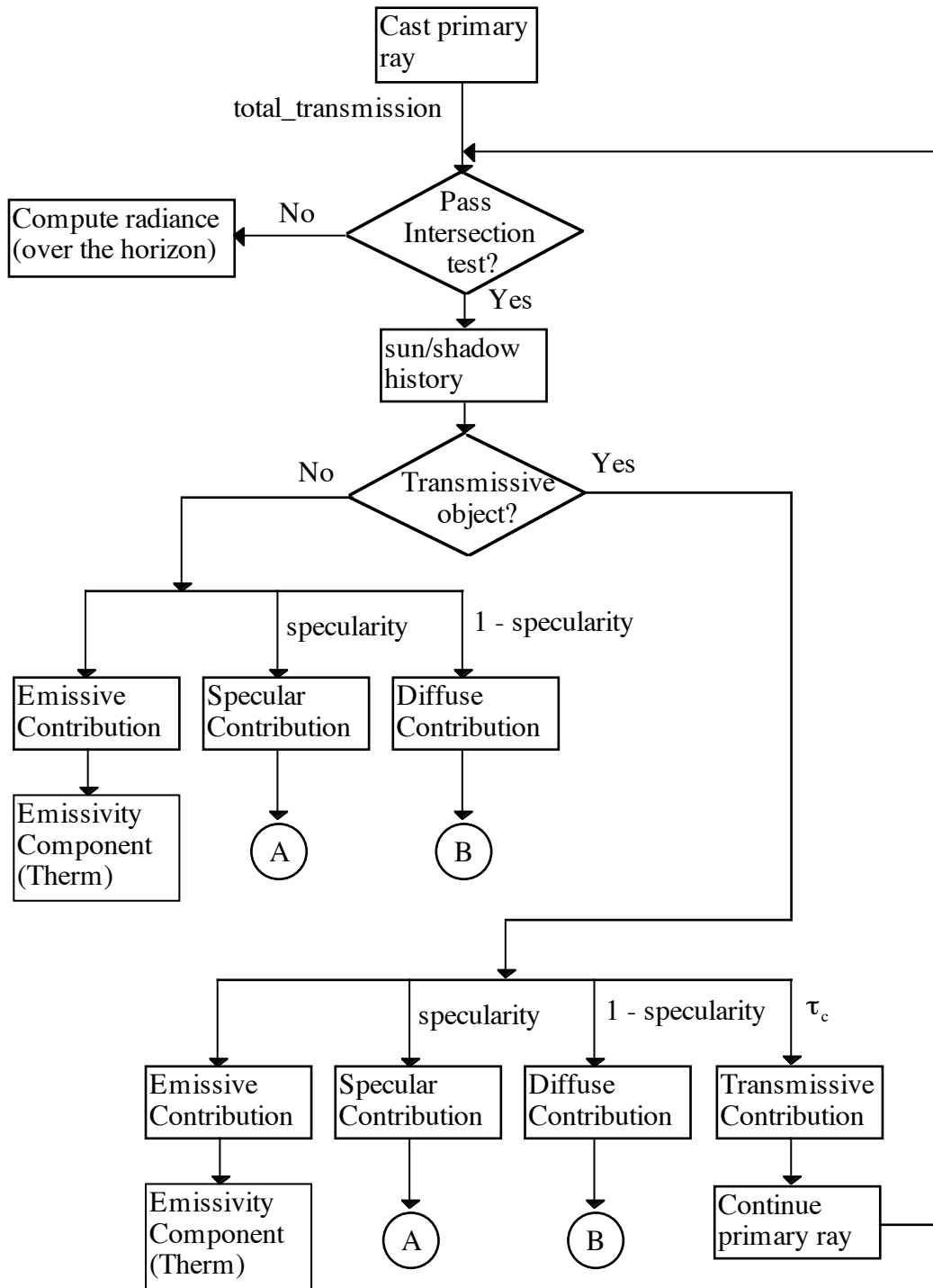


Figure 3.8. DIRSIG Ray Tracer Flow

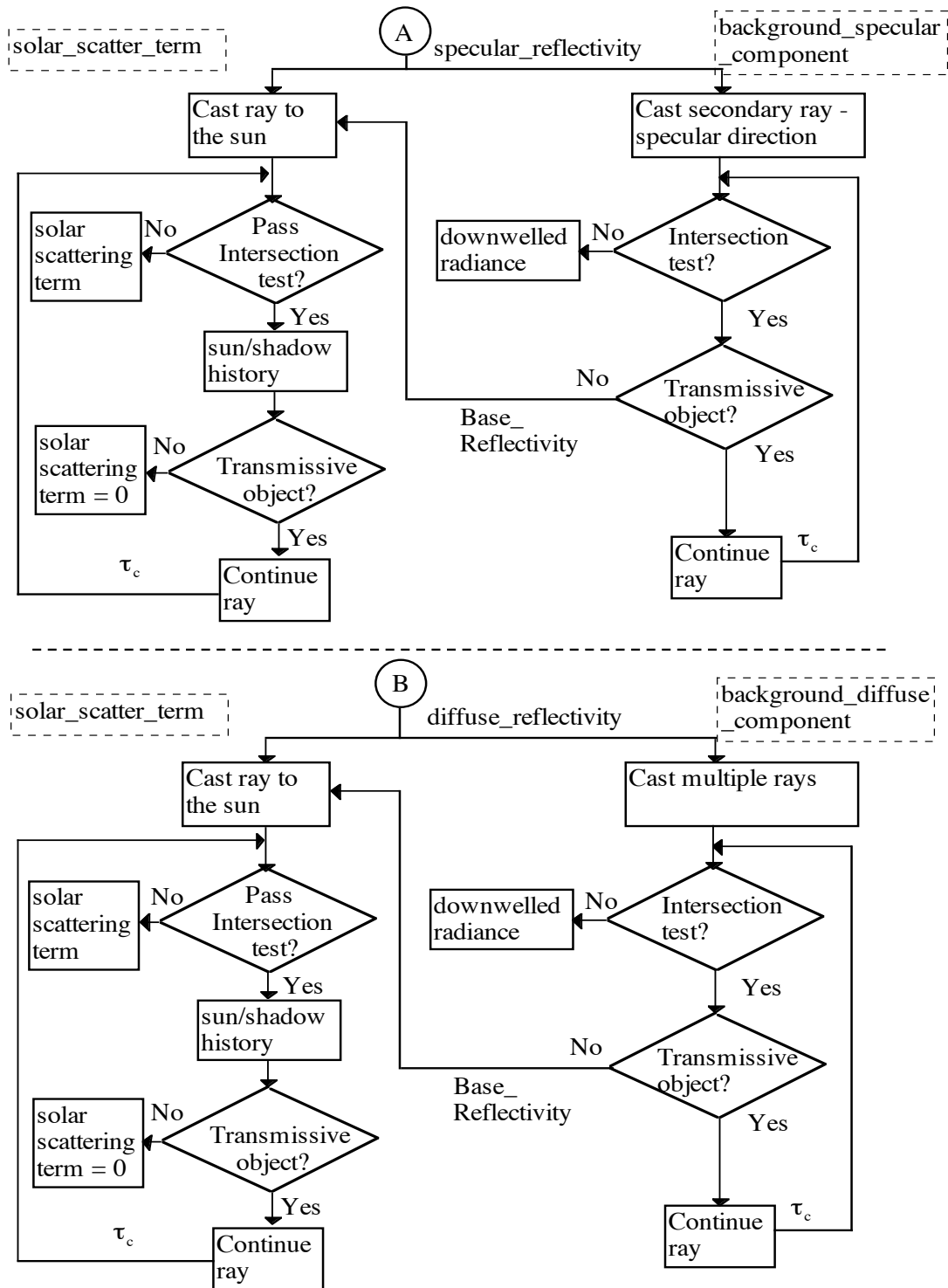


Figure 3.9. DIRSIG Ray Tracer Flow (continued)

The process begins by casting a ray from the focal plane (single pixel) onto the scene. The ray starts at the center of the pixel and its path is determined through sensor-scene geometry. The path of the ray also provides the required information for the retrieval of radiance and transmission values from the radiance database described above.

Within the scene, the facet (if any) the ray strikes is determined through intersection tests. If the ray does not pass the intersection test (does not intersect a facet), it is assumed that the pixel is looking above the horizon and the effective sky radiance is computed. If the ray passes the intersection test, the sun/shadow history is computed.

The sun/shadow history is computed by casting a ray from the facet to the sun at set time intervals. Typically, a 15 minute interval and a 24 hour time period are used. If the ray intersects an opaque facet, the direct solar insolation term is set to zero for that time. If the ray intersects a transmissive facet, the solar irradiance term is multiplied by the predicted transmittance of the intersected facet and  $t_1$ . If the ray does not intersect any facets, the direct solar insolation term is used. DIRSIG can also model the effects of moving objects obscuring the sun during the history. Based on this information, the THERM submodel computes the time dependent facet temperature.

The next step is to determine if the facet is transmissive or opaque. If the facet is opaque, the emissive and reflective radiance contributions exiting the facet are determined. The reflective contribution is broken into specular and diffuse contributions, weighed by the facet material specularity and its complement ( $1 - \text{specularity}$ ). This value is contained in the materials database. The emissive contribution is computed using the therm submodel, which is described separately.

The specular contribution is computed by casting two rays, one to the sun and one in the specular direction. The radiance contributions resulting from these two rays are combined and reduced by the specular\_reflectivity. The specular\_reflectivity is computed by multiplying the spectral reflectivity by the angle dependent specular fall-off values. If the ray cast to the sun does not intersect a facet, the solar\_scattering\_term is used. If the ray cast to the sun intersects a facet, the sun/history of that facet is determined. If the facet is opaque, the solar\_scattering\_term is set to zero. If the facet is transmissive, the ray is continued and the transmission coefficient is noted for reduction of the radiance attributable to the continuing ray.

If the ray cast in the specular direction does not intersect a facet, the downwelled radiance is used. If the ray intersects a transmissive facet, the ray is continued and the transmission coefficient of the intersected facet is noted for reduction of the radiance attributable to the continuing ray. If the ray intersects an opaque facet, a second ray is cast to the sun and the spectral reflectivity of the facet noted in order to adjust the radiance reflected by this facet. This ray then undergoes the same testing as the original ray cast to the sun.

The diffuse contribution is computed similarly to the specular contribution except that multiple rays are cast in addition to the ray cast to the sun. The contribution from each of the multiple rays is weighed appropriately. The weighing of the contributions can be complicated, as each ray represents a solid angle. As such, boundaries are implied. DIRSIG assigns an equal weighting to each ray, thus putting the boundaries equal distance from each point. The acceptability of this approach is discussed in Section 5. The ideal (continuous, not discrete) handling would require an integration of the form.

$$L = \int \int_{\phi \theta} L(\phi, \theta) * r(\phi, \theta) \partial \phi \partial \theta$$

where f and q define the limits of integration (the solid angle.)

The emissive component, specular component, and the diffuse component are then summed, multiplied by the atmospheric transmission coefficient (total\_transmission), and added to the upwelled radiance. This is the radiance reaching the sensor.

### Thermal Submodel

The thermal submodel calculates the time dependent temperature of a facet using a program called THERM. THERM was developed by DCS Corporation (1987) for the US Air Force. It predicts the object temperature based on the material characteristics of the facet, environmental influences, and internal sources. The calculations are based on a first principles understanding of the rate of heat transfer corresponding to a specific temperature difference between an object and its environment. Temperatures for each facet are computed separately and in isolation. Inter-facet conductive transfer is not modeled. A more detailed treatment of the Thermal Submodel is provided by Kraska (1996.)

### Sensor Submodel

The sensor submodel reduces the radiance reaching the sensor by the sensitivity of the sensor. This is accomplished on an incremental bandpass basis. The incremental contributions are then combined into the number of bands of the sensor. The sensor submodel also accounts for the type of sensor (Salacain, 1995).

This review of representative SIG models, and DIRSIG in particular, provides the basis for the discussions that follow.

### **3.5 A Review of Efforts to Validate SIG Models**

Now that representative models have been described, one wonders just how good they are. Validation results for most SIG models, except for DIRSIG, are hard to find in published literature. The reason for this is unknown. The descriptions of some models claim validation, but do not publish the results. This presents two problems. The first is that it is impossible to compare the performance of one model against another, i.e. measure the state of the art. The second problem involves the lack of a standard validation procedure. The one paper that did describe other validation techniques, but without results, listed statistical comparisons (histograms) and MTF comparisons as acceptable methods (Lindahl, 1990). However, because the models are still being used and developed, it must be assumed that they are satisfying the needs of their primary customers. TAV-IR continues to serve as input to canopy designs and CREATION as input to sensor and algorithm designs.

DIRSIG is the one model that has consistently published validation data. Stark baselined DIRSIG and published results in 1993. However, since that validation, many improvements have been made. In particular, the radiometry submodel has been rewritten. It can now handle targets that have specular and diffuse components, surface texture, and transmissive objects such as clouds and vegetation (trees). As the improvements were made, they were evaluated but not formally validated. This study will provide that validation, the first since the baseline. However, it will take a different approach than Stark's to scene selection, aerial images from two perspectives will be

used instead of a single perspective from a roof top. This approach will more closely simulate the conditions under which DIRSIG is used.

The validation will use Rank Order Correlation (ROC) and Root Mean Squared (RMS) error as metrics. ROC measures the relative brightness' of different objects of an image with the relative brightness' of those same objects in the comparison image. The formula for ROC is given below (Servoss, 1993).

$$\rho_{TOD} = 1 - \frac{6 \sum (R_i - R'_i)^2}{n^3 - n}$$

where

$\rho$	Correlation coefficient
TOD	Time of Day
$R_i'$	Rank in DIRSIG
$n$	Number of samples
$R_i$	Rank in the real imagery

This technique was not found in published validation descriptions of other SIG models. However, since other methods have not been described, it can not be determined if it is used or not. The other technique that will be used is RMS error. This technique will give insight into the overall bias errors between the actual and synthetic images. As a point of comparison and discussion, the histograms of the SIG and reference images will be discussed. The histograms will provide an insight into the overall image statistics.

Analysis of the results, and a review of the model, will provide information not only on how well DIRSIG models the remote sensing imaging chain but on our understanding of

the imaging chain itself. In particular, this study has chosen to focus on the reflectivity link in the imaging chain.

### **3.6 Reflectivity Review**

Much of the work of remote sensing is based on the spectral signatures (colors) of the objects in the images. The spectral signature is mainly, assuming common illumination, a function of the reflective characteristics of the object material(s). For this reason, reflectivity is a main focus of this study. The goal is to determine how important it is and how best to model it. In this section, reflectivity is defined, various reflectivity models available to SIG developer are reviewed, the various sources of data available to the models are described, the nature of reflectivity in actual remote sensed imagery is discussed, and how DIRSIG models reflectivity is reviewed. This information will serve as a basis for the sensitivity analysis and proposed improvements to the current model presented in Section 5.0.

#### **3.6.1 Definition**

Reflectivity is a material characteristic that describes how a material reflects light. It is a function of the composition of the material, the surface roughness, the wavelength of the incident radiation, and the illumination and viewing angles. For coatings, such as paint, it can also be a function of coating thickness. The character of reflectivity is described by the Bi-Directional Reflectance Distribution Function (BRDF) and has units of inverse steradians ( $\text{sr}^{-1}$ ). Because in many situations a unitless measure is desired, the term Bi-Directional Reflectance Factor (BDRF) was developed. BDRF is defined as “the ratio of radiant flux actually reflected by a sample surface to that which would be reflected into the same beam geometry by an ideal (lossless) perfectly diffuse (Lambertian) standard

surface irradiated in exactly the same way as the sample” (Feng, 1990). BRDF is related to BDRF by

$$r_{BRDF} [sr^{-1}] = \frac{r_{BDRF}}{\pi [sr]}$$

According to Schott (1990), “data acquired at fixed illumination angles indicate that common backgrounds can vary in their reflectance factors by 100 to 400% for view angles ranging from nadir to 75 degrees off nadir.” Generally, materials are classified as specular, diffuse, or non-ideal (typical). A material that reflects all incident energy at the same zenith angle, but 180 azimuthal degrees away, is classified as specular. A highly polished piece of metal is an example of a specular material. A material that reflects incident energy equally into the hemisphere above it is classified as diffuse or Lambertian. Grass, unfinished concrete, and asphalt can be loosely classified as diffuse. Most materials have both specular and diffuse components and are classified as non-ideal or typical. These cases are shown in Figure 3.10.

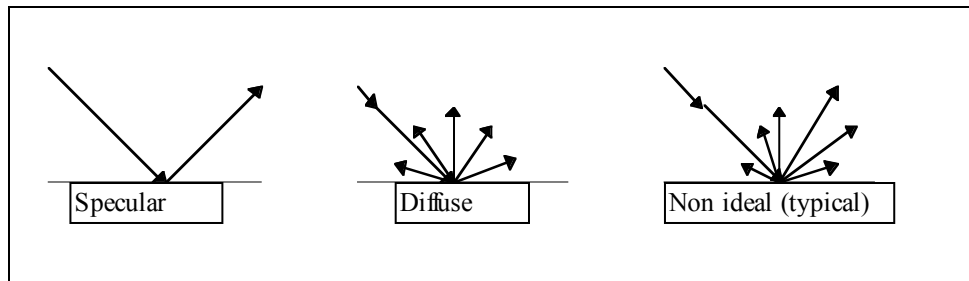


Figure 3.10 Reflectivity Characteristics (Stark, 1993)

The shape of the BDRF surface is also influenced by the surface roughness of the material. Generally, the rougher the surface of a particular material the more diffuse it appears for a fixed wavelength. This is a result of the net effect of the light striking the

surface at many angles. The rougher the surface the more surface orientations there are in a small area for the light to reflect against. The same results are observed when the wavelength is decreased.

### **3.6.2 Reflectivity Approaches in SIG Models**

There is a spectrum of approaches for handling reflectivity in SIG models. At one end of the spectrum is the strict use of empirical data. At the other end are pure mathematical models. Of course, the approach taken by most SIG models uses empirical data in conjunction with a math model. The particular approach lies in a trade space that balances the difficulty of obtaining data to feed the model, computational limitations, and the radiometric fidelity required by the application.

Using material reflectivity (BRDF) databases can produce excellent results if the databases are extensive. However, extensive databases are scarce and creating one is a costly, labor intensive, tedious, and time consuming task. In addition, obtaining controlled measurements are often impractical or impossible.

Some of the models available to SIG developers include, Lambertian, Phong, Cook-Torrance, Culpepper (Culpepper, 1995) (Cook, 1982), DIRSIG, and White (proposed). DIRSIG's model is discussed in Section 3.6.5.

The Lambertian model assumes that the incident radiance, attenuated by the reflectivity of the material, is reflected uniformly over the hemisphere above the material. It is given mathematically by

$$\text{BRDF} = r / \pi [\text{sr}^{-1}]$$

where  $r$  is a constant between 0 and 1

In discrete implementations (ray-tracing) the  $1/p$  is replaced by the fraction of the hemisphere (solid angle) represented by the ray cast.

It is shown graphically in Figure 11.

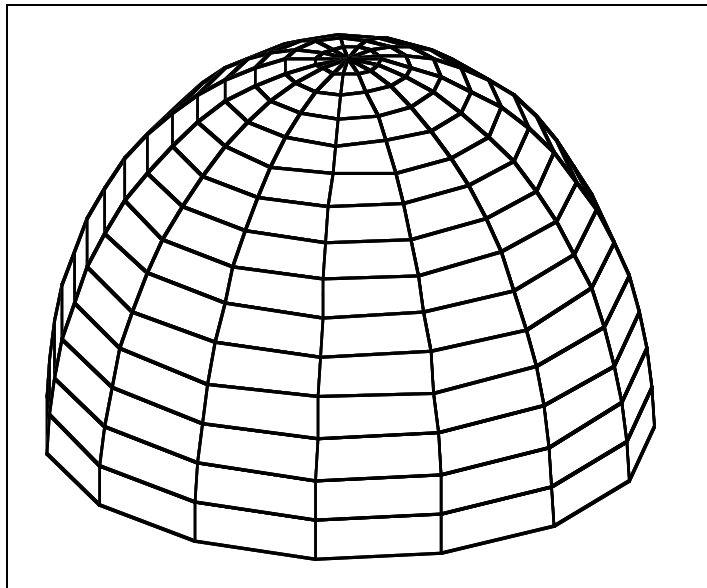


Figure 3.11. Lambertian reflectivity

In SIG models,  $r$  is often given as a function of wavelength to improve fidelity. The advantages of this model include the ease of obtaining input data and computational efficiency. The input data can be obtained using a simple “low cost” spectral-densimeter. The one used by the researcher costs only a few thousand dollars, is very accurate, easy to use, and can be taken into the field. Since the reflectivity is modeled as a dome over the material, no computation is required. The disadvantage of this approach is evident when the specular nature of material is important to the application.

The Phong model (Phong 1975, Culpepper 1995), which is extensively used in computer graphics, improves upon the Lambertian model by adding a specular lobe term. The specular lobe is modeled with a cosine function. It is given mathematically by.

$$BRDF = \frac{r}{\pi} + \frac{A \cos^\epsilon(\beta)}{\pi} \quad [sr^{-1}]$$

where

$r / \pi$  is the Lambertian term

$A$  is the specular lobe peak amplitude

$\beta$  is the angle between the sample direction and the specular direction

$\epsilon$  is a parameter which describes the specular lobe shape; the larger  $\epsilon$ , the more narrow the lobe.

The model is shown graphically in the Plane of Incidence (PLIN) (using the parameters listed) in Figure 3.12.

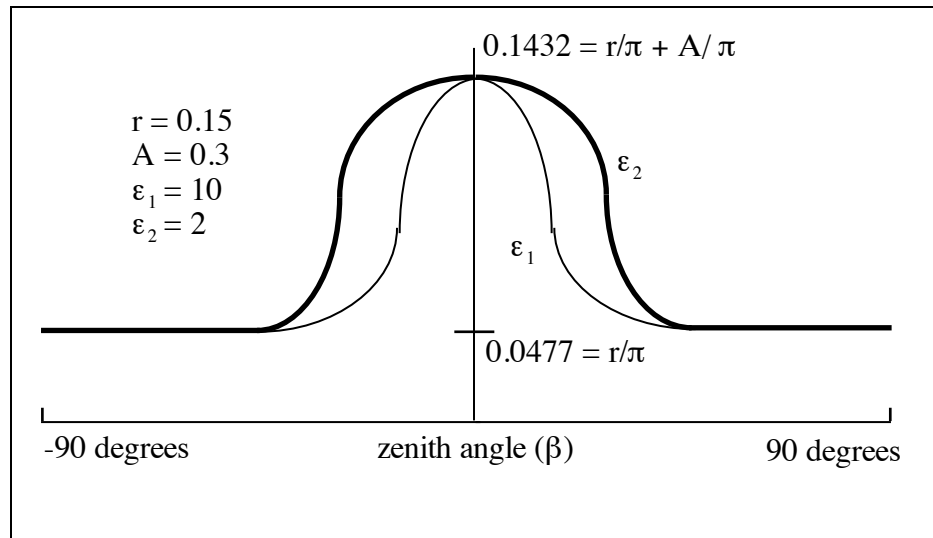


Figure 3.12. Phong Reflectivity

The model as described, is not sensitive to wavelength or azimuthal angle. If these issues are addressed, the model is much more accurate. The major advantage of this approach is the relatively small number of inputs required, the ease of obtaining them, and the small computational requirements. The inputs for the Lambertian term can be obtained for individual materials with a spectral-densitometer and the inputs for the spectral lobe can be obtained for a class of materials using a PLIN instrument. (PLIN is described in section 3.6.3) The major disadvantage of this model is that the function used to describe the spectral lobe may not fit the experimental data to the accuracy required.

The Cook-Torrance model (Culpepper, 1995) also contains Lambertian and specular terms. The model treats the surface of the material as collection of micro-facets whose orientation characterize the reflectance of the material. It is given by

$$BRDF(\theta_i, \theta_r, \theta_N, \alpha) = \frac{r}{\pi} + \frac{1}{\pi} \frac{F(\alpha)}{F(0)} \frac{D(\theta_N)S(\theta_i, \theta_r, \theta_N)}{\cos \theta_i \cos \theta_r} \quad [sr^{-1}]$$

where

$r/\pi$  is the Lambertian term

F is the Fresnel reflectivity factor

D is the distribution function of the micro-facet slopes

S is the shadowing/masking factor

$\theta_i, \theta_r, \theta_N, \alpha$  are as shown in Figure 13.

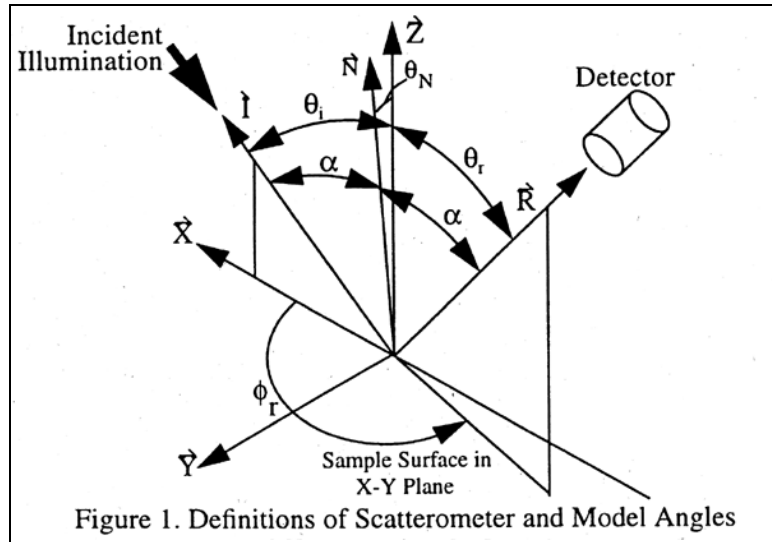


Figure 3.13. Model angles

The input and computational requirements of this model limit its utility for SIG applications. A graph of the model is not available due to lack of input data.

Culpepper's (1995) does not separate the BRDF into diffuse and specular terms, rather it attempts to find a function that matches empirical (BRDF) data. It is given by

$$BRDF = \frac{\left( \sqrt{\left( \Pi_1 \cos \frac{\gamma}{2} \right)^2 + \left( \Pi_2 \cos \frac{\gamma}{2} \right)^2} \right)}{\cos \theta_r} \cdot T(\theta_i, \beta, \gamma) \quad [sr^{-1}]$$

where  $\Pi_1 = f_{r1}(\theta_i, \beta) \cos \theta_{r1}$  and  $\Pi_2 = f_{r2}(\theta_i, \beta) \cos \theta_{r2}$  = empirical results at  $R_1$  and  $R_2$

T is an empirical function for adjustment of the specular lobe shape

(T = 1 in the PLIN)

Angles are as shown in Figure 3.14.

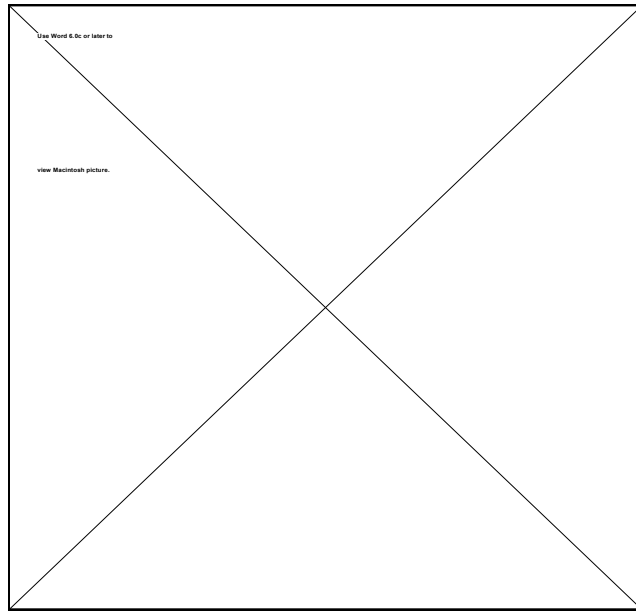


Figure 3.14. Angles for Culpepper's model

The model, in the PLIN, is shown graphically in Figure 3.15

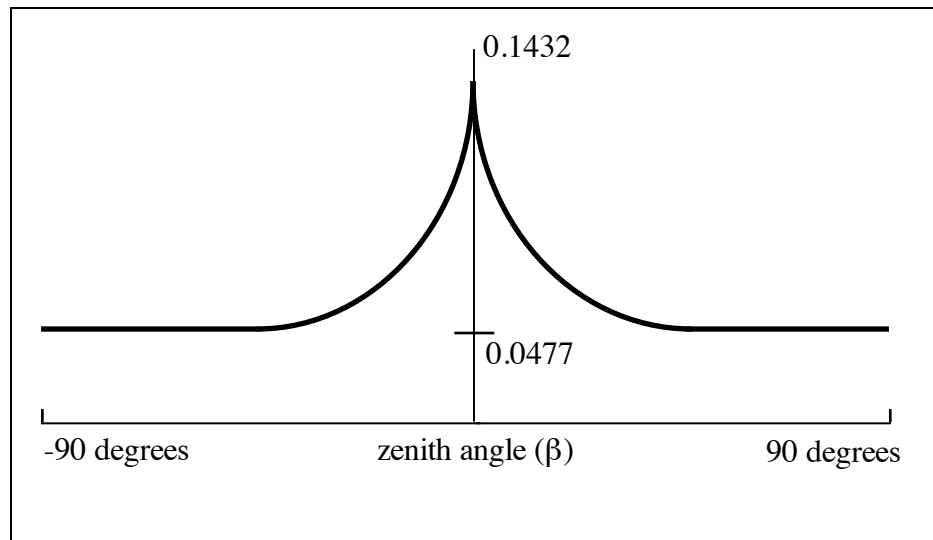


Figure 3.15. Culpepper's model

The advantages of this model are (potential) radiometric accuracy and the relative ease of obtaining input data. Culpepper has been able to model the BDRF data of a **very small**

number of materials to with 10% for any combination of incident and viewing angles. Input data consists of PLIN incident measurements. The disadvantage of this model is the small but significant increase in computational requirements.

The last model, White's (proposed), is similar to Phong's except that a cone function is used for the specular lobe instead of a cosine function. It is given by

$$\text{If angle } |\phi_\varepsilon| > |\beta| \quad BRDF = \frac{r}{\pi} \quad [sr^{-1}]$$

$$\text{Else} \quad BRDF = \frac{r}{\pi} + \frac{\alpha}{\pi} * TRI\left(\frac{\phi_\varepsilon}{2\beta}\right) \quad [sr^{-1}]$$

where  $r/\pi$  is the Lambertian term

$\phi_\varepsilon$  is the angular distance from the specular bounce direction  
(includes zenith and azimuth distances) [degrees]

$\alpha/\pi$  is the specular lobe peak amplitude as measured from the amplitude of the  
Lambertian term [ $sr^{-1}$ ]

$\beta$  is the angular width (includes zenith and azimuth distance) of the base of the  
specular lobe [degrees]

The model, in the PLIN, is shown in Figure 3.16.

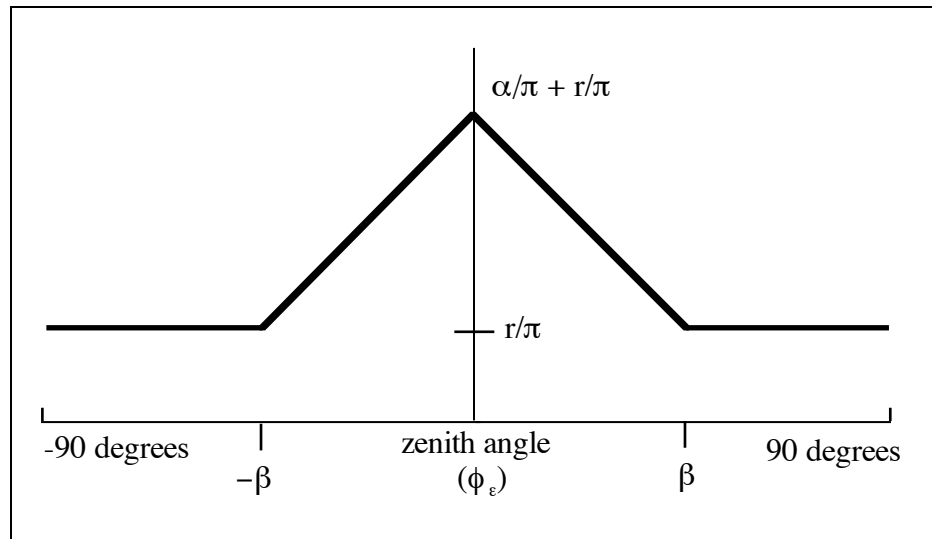


Figure 3.16. White's model (proposed)

The advantages of this model are the ease of obtaining data, computational simplicity, and a structured design for SIG modeling. The inputs for the Lambertian term can be obtained for individual materials with a spectral-densitometer and the inputs for the spectral lobe can be obtained for a class of materials using a PLIN instrument. The major disadvantage of this model is that the function used to describe the spectral lobe may not fit the experimental data to the accuracy required.

While these models can match the BDRF data to various degrees, their fidelity is also a function of how they are implemented in SIG models. Typically, in SIG models which take a ray-tracing approach, the number of rays cast from the material to characterize the reflectance is limited due to computational requirements. The result is a sampling of the surface, reducing its accuracy. In addition, the rays must characterize the radiance map over the material facet, which is different topographically from the reflectance map. Thus the SIG model must choose the number of rays and their orientation intelligently to minimize error.

This concept is shown in Figure 3.17.

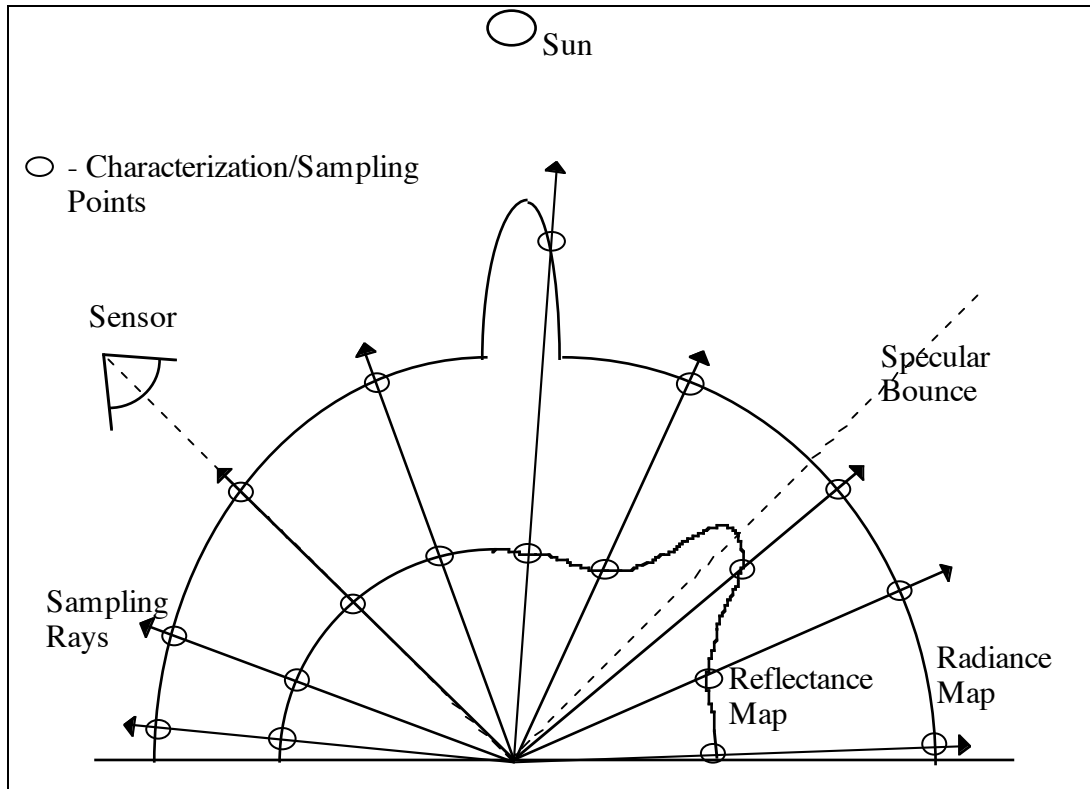


Figure 3.17. Sampling due to ray-tracing. Note: The radiance map is not to scale, the solar lobe peak is actually much greater than shown relative to the downwelled portion of the map.

The values at each characterization/sampling point along a ray, by definition, represents the map values over that solid angle. From the figure, it is clear that if a ray is not cast towards the sun or in the specular direction large errors can occur. This is especially so if the sun and specular directions coincide. In addition, significant errors can occur when obscuration of the radiance map due to background objects such as buildings, trees, or topography (shape factor) occurs, as illustrated in Figure 3.18.

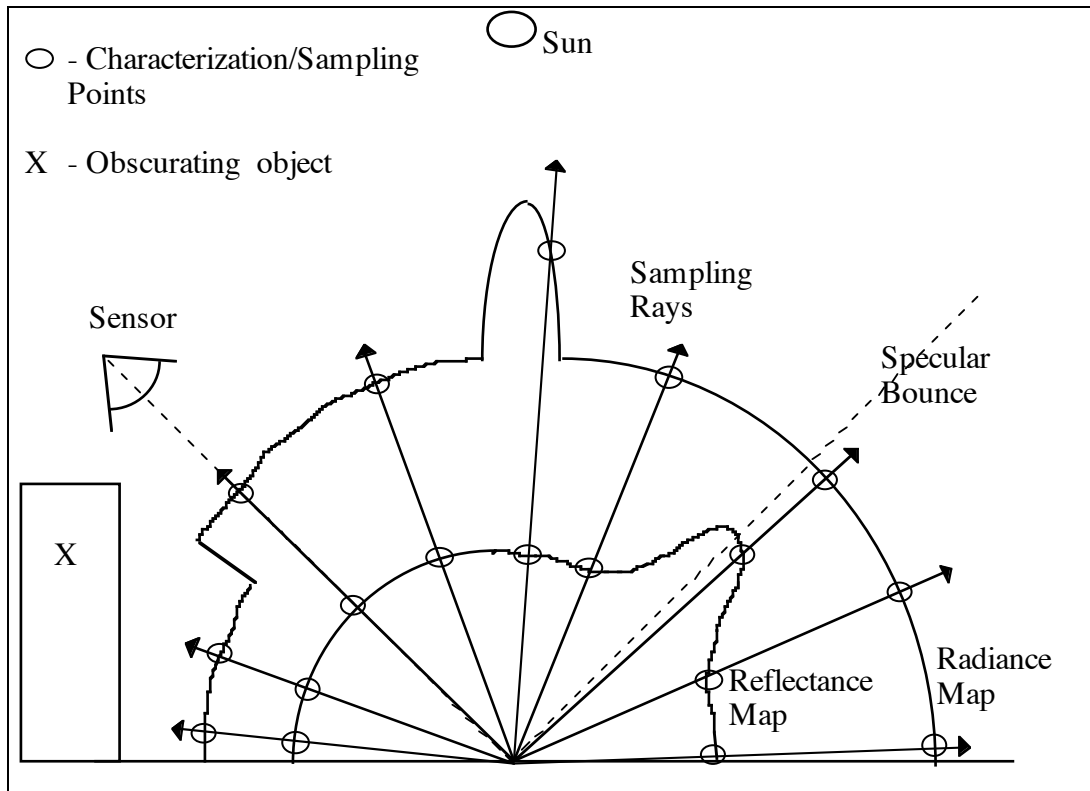


Figure 3.18. The impact of shape factor.

### 3.6.3 Source Data for Reflectivity Models

The value of above models is also a function of the ability (ease) of obtaining data for them. In this section, common methods for measuring reflectivity values are discussed with the focus on how the measurements would feed the models. The individual model may require a combination of the following methods.

#### Bi-Directional Reflectance (with fixed angle)

This is one of the simplest and easiest measurements to take. The setup is shown in Figure 3.19.

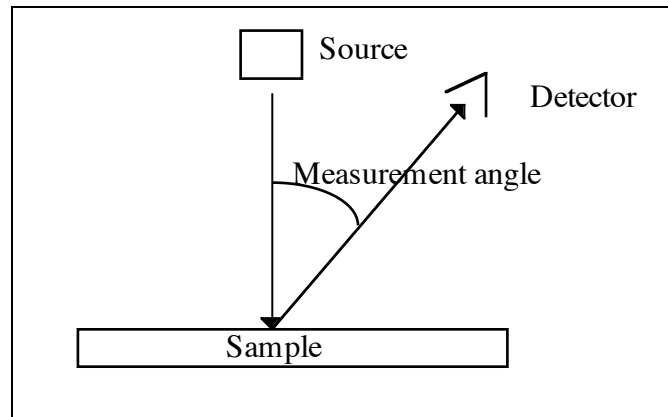


Figure 3.19. Bi-Directional Reflectance

The sample is irradiated perpendicular to its surface and the reflected radiation is measured over a pre-defined solid angle at a fixed angle relative to the source. Typically, angles of 15 or 45 degrees are used (angles that are not in the specular lobe).

These measurements can be used for the Lambertian term in the models that separate reflectivity into diffuse and specular components. During the research for this study, it was discovered that these measurements are often taken as the “reflectivity” of the material even though the spectral lobe is not included.

The simplicity of the measurements has allowed handheld spectral-densitometers to be developed. These instruments are very convenient for making field measurements to fill a database or to provide ground truth data.

### Bi-Directional Reflectance (BRDF)

The ultimate input to the above models would be to characterize the reflectance of a material over all combinations of incident and viewing angles, the instrument must be able to adjust the source and detector orientations, BRDF. However, instruments that are

capable of this are generally confined to laboratories due to size and calibration requirements. The utility of these instruments is also limited due to the complexity of the measurement setup and operation. The value in these measurements for the SIG developer is that they can be used to validate reflectance models.

#### Hemispherical Reflectance with spectral lobe (Directional Hemispherical Reflectance)

This type of measurement provides the average reflectance into the hemisphere above the material. The setup is shown in Figure 3.20.

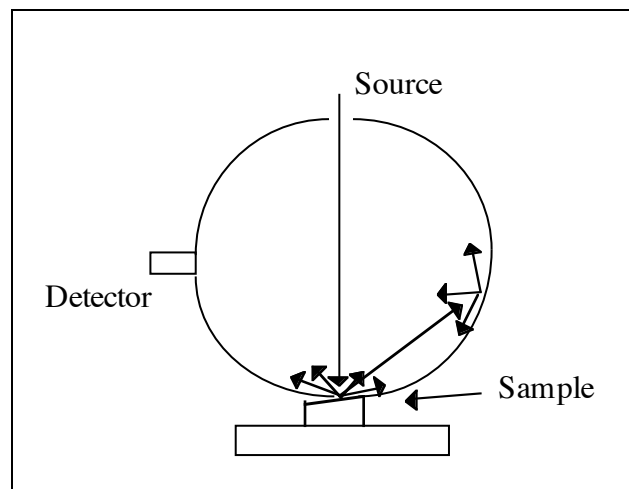


Figure 3.20. Hemispherical Reflectance

The sample is irradiated slightly off perpendicular with respect to the source. The radiation measured at the detector is then the integrated hemispherical reflectance of the sample.

Because the measurement includes the specular lobe, the reflectance, in general, will be greater than that measured with the fixed angle bi-directional reflectance. This limits their usefulness except as a coarse validation of the reflectance model. By subtracting

this measurement from the fixed angle bi-directional reflectance measurement the contribution of the specular lobe can be roughly (without directional information) estimated.

### Hemispherical Reflectance without specular lobe

This measurement is similar to the previous measurement except that specular lobe is removed. The setup is shown in 3.21.

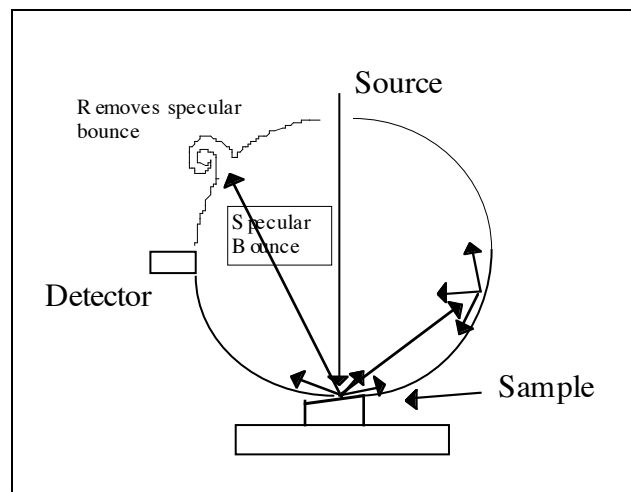


Figure 3.21. Hemispherical Reflectance

The radiation measured by the detector more accurately represents the diffuse, or Lambertian, reflectivity.

### Plane-of-incidence (PLIN)

PLIN measurements are a subset of the BRDF measurements. The setup is shown in Figure 3.22.

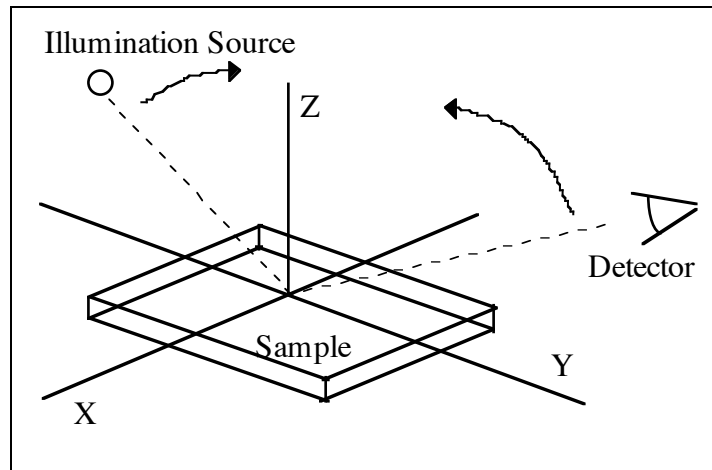


Figure 3.22. PLIN setup

The sample is placed in the X-Y plane. The illumination source and the detector are placed in the Z-Y plane (typically). Measurements are taken with the source and detector at all combinations of angles within that plane. The result is a partial BRDF set. By assuming symmetry in the spectral lobe and diffuse reflectivity, inputs to most of the models can be derived. Appendix B describes how these values for a class of materials can be obtained from the Non-Conventional Exploitation Factors (NEF) database (NEF, 1995).

The aperture, or the area of the material over which the measurements is made, is also significant. In general, the effective aperture should match the resolution of the synthetic imagery. This means that if the aperture of the instrument is small, multiple measurements over the material need to be taken and averaged. In creating SIG images for remote sensing, scale is also an issue. Often, the resolution of images greatly exceeds the scale of the objects in the scene. For example, the scale of a shingle may be 0.3 meters and the resolution of the image may be 3 meters. This means that to generate radiometrically accurate images, the reflectances of several shingles must be averaged. (Often, a roof consists of several complementary colored shingles.)

### **3.6.4 Material Reflectivity in Actual Imagery**

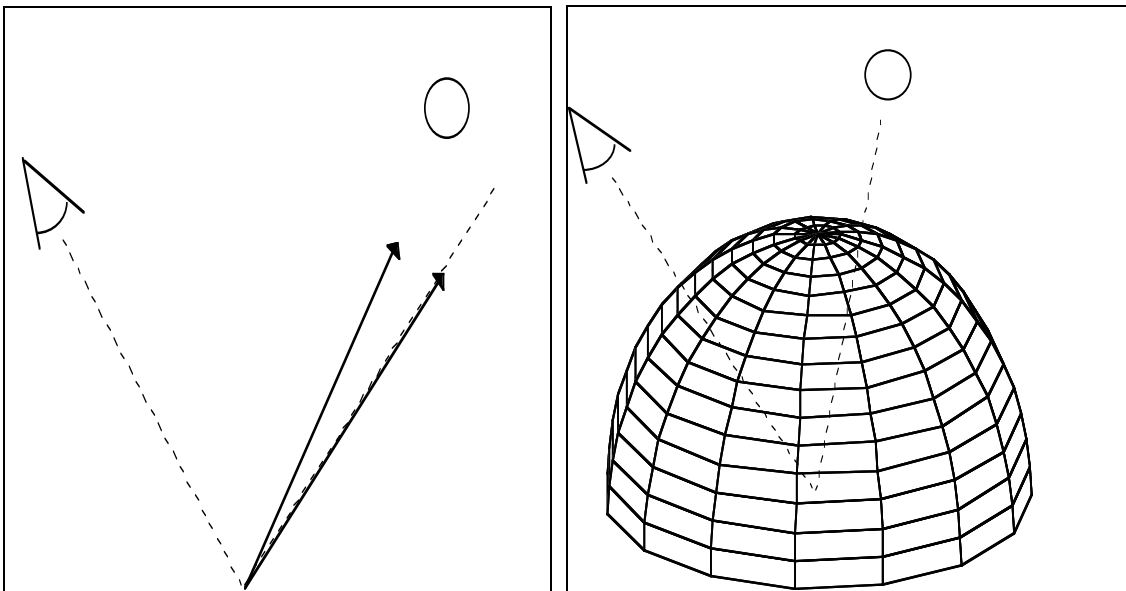
While it may appear that the character of reflectivity presents many difficulties for the SIG model, this is not necessarily the case. Most imaging systems act as integrators. Radiance is collected over a defined area (pixel) and spectral band. Therefore, the reflectivity measured is an average over a range of viewing angles and wavelengths. The larger the projected area of the pixel onto the scene the larger the range of viewing angles over which the reflectivity is averaged. This reduces the sensitivity of the measured reflectivity to changes in viewing angles. A similar reduction in sensitivity is caused by the imaging system that integrates over a large range of wavelengths.

These “realities” create a condition of diminishing returns with respect to reflectance model fidelity. A model of high fidelity, such as Culpepper’s, may not model “reality” any better than a low fidelity model, such as DIRSIG’s current model, but have higher computational and source data requirements. The point is that the modeler must balance the trade space with the actual requirements (reality).

DIRSIG attempts to make this balance in its reflectivity model, as discussed in the next section. In particular, DIRSIG attempts to account for the significant “bumps” in the radiance and reflectance maps, i.e. the solar radiance and the specularity.

### **3.6.5 DIRSIG’s Treatment of Reflectivity**

DIRSIG breaks the reflectivity map into specular and diffuse components as illustrated in Figure 3.23 and 3.24.



Figures 3.23 and 3.24. DIRSIG reflectivity model. Dashed lines indicate the specular direction.

The specular component consists conceptually of two samples of the reflectivity map. The first sample is in the specular bounce direction and the second is in the direction of the sun. This sampling is designed to capture the significant topographical features of the reflectivity map as well as the radiance the map. Because each of the samples are assigned a specular reflectivity value, this approach is more accurate as the specular bounce direction and the solar direction coincide.

The diffuse component consists of a patterned sampling of a Lambertian surface (dome) and an addition sampling in the direction of the sun. Again, the sampling is designed to capture the significant topographical features of the reflectivity map as well as the radiance the map.

The importance of the DIRSIG's model is shown in Figure 3.25.

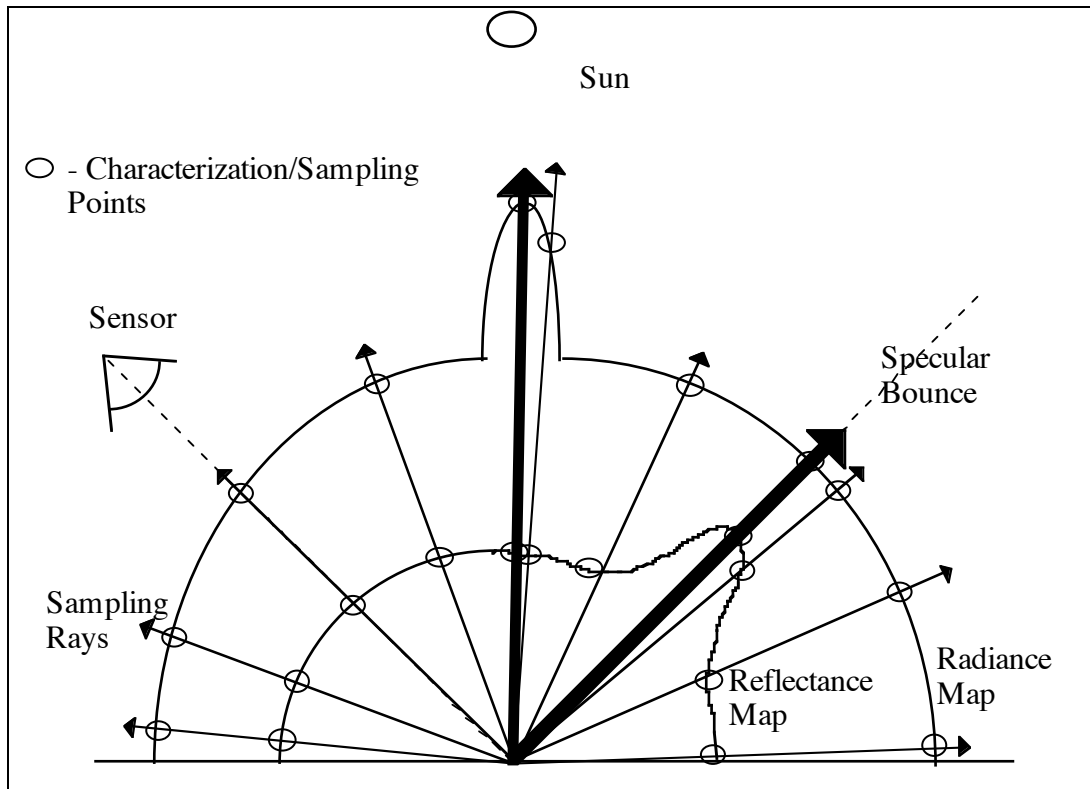


Figure 3.25. DIRSIG Sampling.

The thick lines are the “intelligent” sampling of the reflectance maps to capture the significant topographical features of both the reflectivity map and the radiance map.

DIRSIG also allows for texture maps which allow the reflectivity to be adjusted as a function space and spectrum while still maintaining the statistical parameters of an actual image.

DIRSIG does not dictate a particular method for obtaining input data since sources of data are scarce. This researcher generally used Bi-Directional Reflectance with-fixed-angle (spectral-densitometer) for the diffuse component. PLIN measurements were used to estimate specular reflectivity and specularity (weighting factor).

This review of reflectivity, how it is modeled, and its impact on the final radiance exiting a material shows its importance. A more quantitative measure is provided in Section 5.

## **4.0 Experimental**

This section documents the synthetic image creation, reference image acquisition, and validation processes.

### **4.1 Scene Selection**

The area surrounding the Kodak Hawkeye plant was selected for the target scene. A map of the area is shown in Figure 4.1. The area was suitable for the following reasons.

- The area contained residential, commercial, industrial, and recreational (a park) land use areas, a forest, and a river, eliminating the need for multiple scenes.
- Significant topographical features had not been created in DIRSIG. The area contained significant topographical features, the Genesee River has eroded a 200 foot gorge through the center of the area. The remaining area consists of rolling hills, 50 to 75 feet high.
- The area was 20 minutes from RIT, allowing for repeat visits for ground surveys.
- Aerial imagery was available in multiple perspectives, thus reducing the need to arrange for and fund flyovers of the area. Kodak's Aerial Systems Division is located at the Hawkeye Plant and uses the area as a test target for new films.
- Parts of the target area, the Hawkeye plant and the Driving Park bridge, had already been created, reducing the effort required to create the scene.

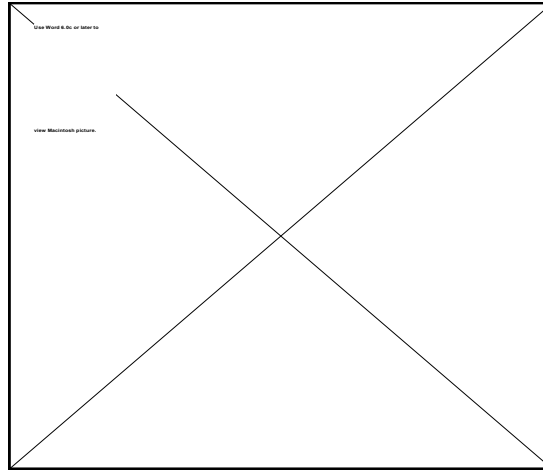


Figure 4.1. Map of the target area.

The target area is 1.1 km by 1.1 km with the Genesee River running south to north through the middle. The Lower Falls [A], Rochester General Electric (RGE) power generation plant [B], and the Driving Park bridge [C] are located in the bottom center of the scene. The Kodak Hawkeye plant [D] and the Rochester School for the Deaf [E] are located on the east side of the river. The Rochester Rose Garden [F], YMCA complex [G], Nazareth Academy [H], Nazareth Hall School [I], and the Grace United Methodist church [J] are located on the west side of the river. The area contains over 850 structures and thousands of trees. Aerial imagery of the area is shown in Image 4.1 (Kodak Aerial Systems, 1994).

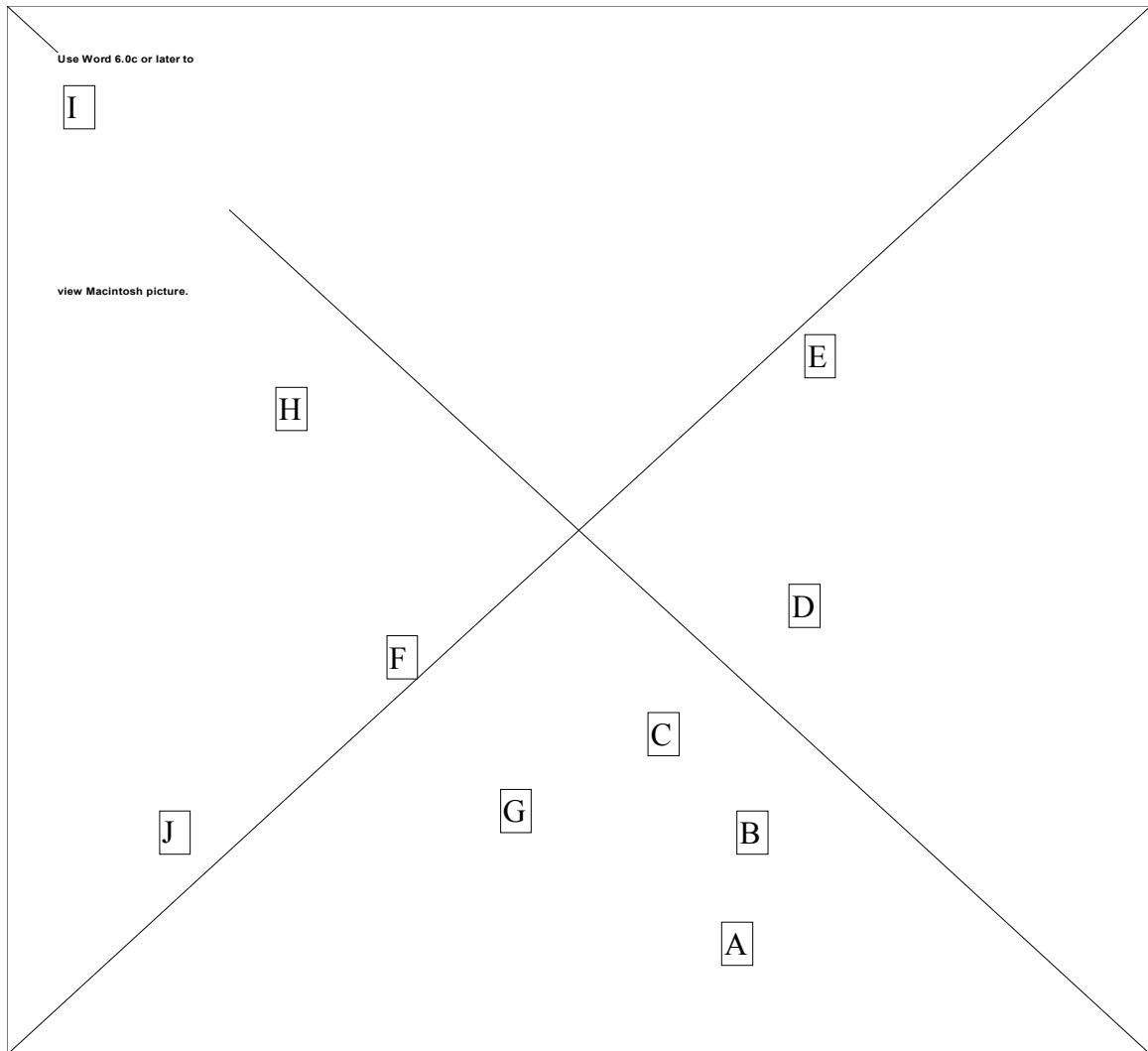


Image 4.1. Aerial Image of the target area.

## 4.2 Scene Creation Process

### 4.2.1 Training

The researcher did not have any experience with DIRSIG or any other SIG model before beginning this effort. Training consisted of reading the DIRSIG tutorial and stepping through it, using DIRSIG, with the help of another graduate student. The tutorial was

straight forward and well documented. After a few days, some experimentation, and several practice scenes, the basics of scene creation were understood. The initial scenes generally consisted of a box or a pyramid sitting on a flat surface. The training process was aided by canned support files, such as weather and scene node files, which allowed the researcher to focus on the mechanics of creating the scene. As the understanding of DIRSIG grew, the DIRS staff was available to answer more detailed questions.

#### **4.2.2 Scene Creation Environment**

The initial scene was created using DIRSIG version 2.9. The final validation used DIRSIG version 3.0. All versions were run on a Dec Alpha 300 running OSF/1 Version 3.2c in the DIRS laboratory. It is important to note that DIRSIG is documented and controlled to the level of an engineering model. If a problem was discovered, the program was modified to correct it immediately.

#### **4.2.3 Creation of Scene Database Files**

Documentation on the structure and the contents of the database files can be found in the DIRSIG User's Tutorial and User's Guide (Salvaggio, April 1991). The references describe how to create the files and show samples. Documentation on ACAD can be found in the ACAD User's manual.

Scene creation requires the generation of eleven databases and one batch file. Those databases and a brief description of their function are provided in Table 4.1.

Table 4.1. Databases required by DIRSIG

<b>File extension</b>	<b>File name</b>	<b>Purpose or Function</b>
.gdb	Geometric database	Contains facet spatial parameters and some facet material parameters
.adv	Look Angle	Contains perspective information and image size
.snd	Scene node	Contains scene position information and some sensor information
.rsd	Radiosonde	Contains radiosonde data required by LOWTRAN
.cdk	LOWTRAN card deck	Contains atmospheric information required by LOWTRAN
.wth	Weather	Contains weather information
.rad	Radiance	Contains atmospheric transmission and radiance values
.mat	Materials	Contains thermal parameters
.ems	Emissivity	Contains emissivity (reflectivity) data
.sen	Sensor	Contains sensor spectral sensitivity parameters
.ext	Extinction Coefficient	Contains extinction coefficients for transmissive materials
.bat	Batch	Executes DIRSIG and contains the location of the databases

Two issues became important when the databases were created, organization and delta testing. In the process of creating the databases hundreds of files are created, therefore a directory tree structure was used to organize the files. Delta, or incremental, testing became important not for validation, but for identifying and eliminating runtime errors. The approach taken was to begin the scene with databases known to be valid, then only change the geometric database. After each significant change, DIRSIG was run. This greatly reduced the time required to isolate errors as only one database had changed. After the geometric database was fairly complete, the remaining databases were modified, one at a time, and test runs were made to ensure that their structure, not necessarily their content, was correct.

#### **4.2.3.1 Creation of the Geometric Database ( .gdb file)**

This database was created with another graduate student who was validating DIRSIG in the IR spectrum (Kraska, 1996). It was the most time consuming and tedious database to create, taking approximately eight weeks of very intense effort. The scene was the most complex of its type that had been created in DIRSIG. Many techniques and strategies were developed in the process to facilitate its creation.

##### Source Data

Topographical information was obtained from the United States Geographical Survey (USGS) map, Rochester West, NY (N4307.5 W7737.5/7.5) and from a Rochester Gas and Electric (RGE) survey of the gorge. The USGS map was created in 1971 from aerial photographs using photogrammetric methods and was field checked in 1976. The scale of the map is 1":24,000' with elevation contours at nominal five foot intervals. (Digital data of the area does not yet exist according to USGS.) The section of the USGS map that covers the target area is shown in Figure 4.1. No background information is available on the RGE map obtained from RGE, however, the map agreed with the USGS map, aerial imagery of the area, and ground surveys conducted by the researcher.

Land use information was obtained from the City of Rochester. The point of contact was

Jeff Tiede, Assistant Field Surveyor  
City of Rochester  
Bureau of Engineering Services  
Department of Environmental Services  
City Hall, 30 Church Street  
Rochester, New York 14614  
716-428-6873

The information was prepared using 1":500' scale photographs taken in April 1991. It includes Geographical Information System (GIS) planimetric layers of buildings, curbs, sidewalks, hydrology, driveway aprons, streets, and city maintained trees (not those on private property). Street light and fire hydrant data were also available but not obtained. The information is maintained in ACAD version 12 and was transferred to ACAD version 11, which we were using at the time, through the ACAD .dxf data transfer format. The land use information cost \$171.18 ( $\$75.00 + 229 \text{ acres} * \$0.07 / \text{acre} = \$171.18$ ) and is shown in Figure 4.2.

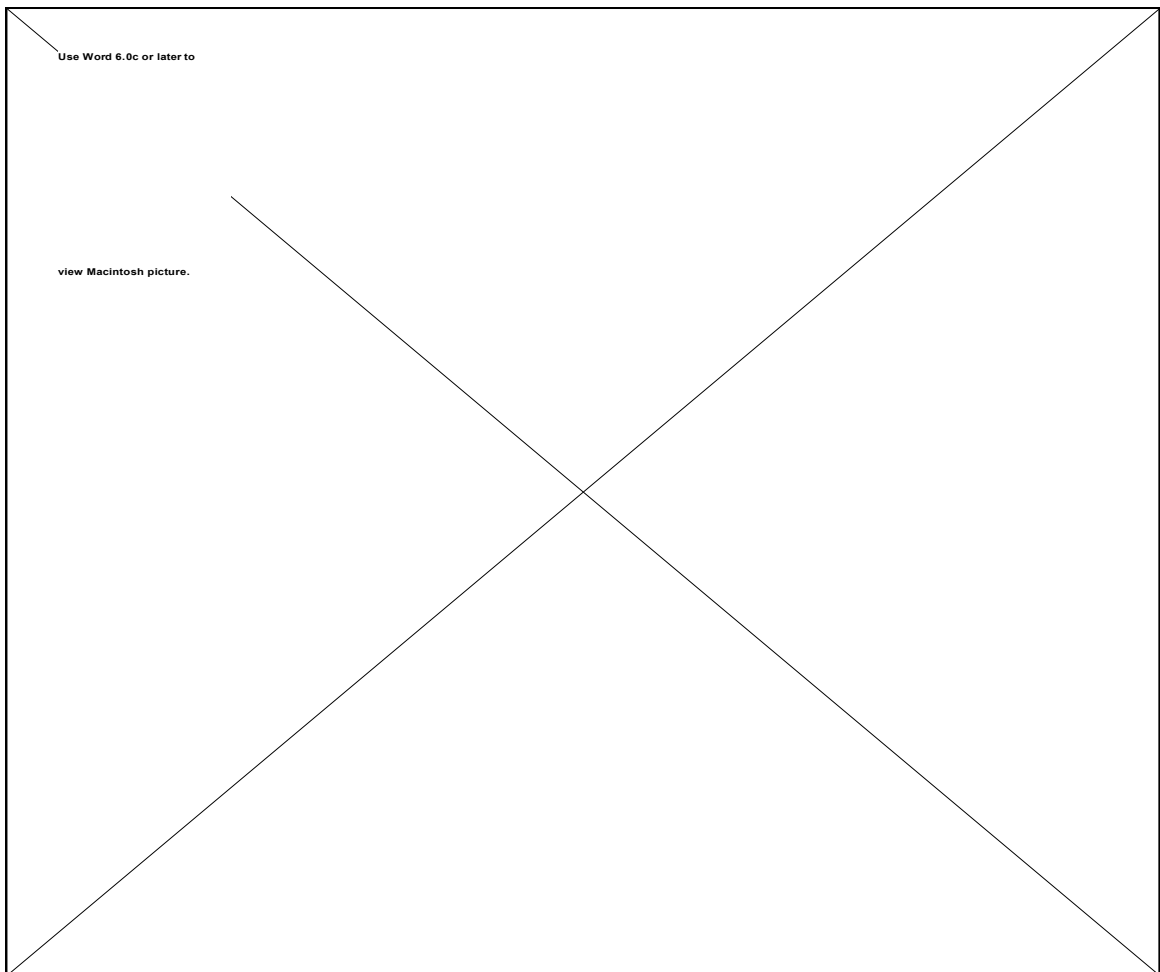


Figure 4.2. Land Use information obtained from the City of Rochester

## File Creation

The geometric database was initially created using ACAD version 11 (Autodesk, 1989) running on a Dec Alpha 3000 running OSF/1 Version 3.2c. Later, the generation of the database was moved to ACAD version 13 running on a Silicon Graphics Indigo running IRIX 5.3.

The resolution and detail of the database varied based on the information available and rough estimates of the resolution required for validation. In addition, the scene was limited to approximately 120,000 3-sided facets (DIRSIG allows 3 or 4-sided facets), the maximum DIRSIG could handle using the DIRS computers available at the time. (This limitation was due to system memory.) The bulk of the facets were allocated to the roughly 3,000 trees in the scene.

To reduce DIRSIG runtime (mostly through minimizing intersection testing), the scene was broken into 20 areas, as shown in Figure 4.3. Each area was an object and the objects were made up of parts; topography, streets, sidewalks, individual houses, and individual buildings. Groups of trees were treated as objects for convenience.

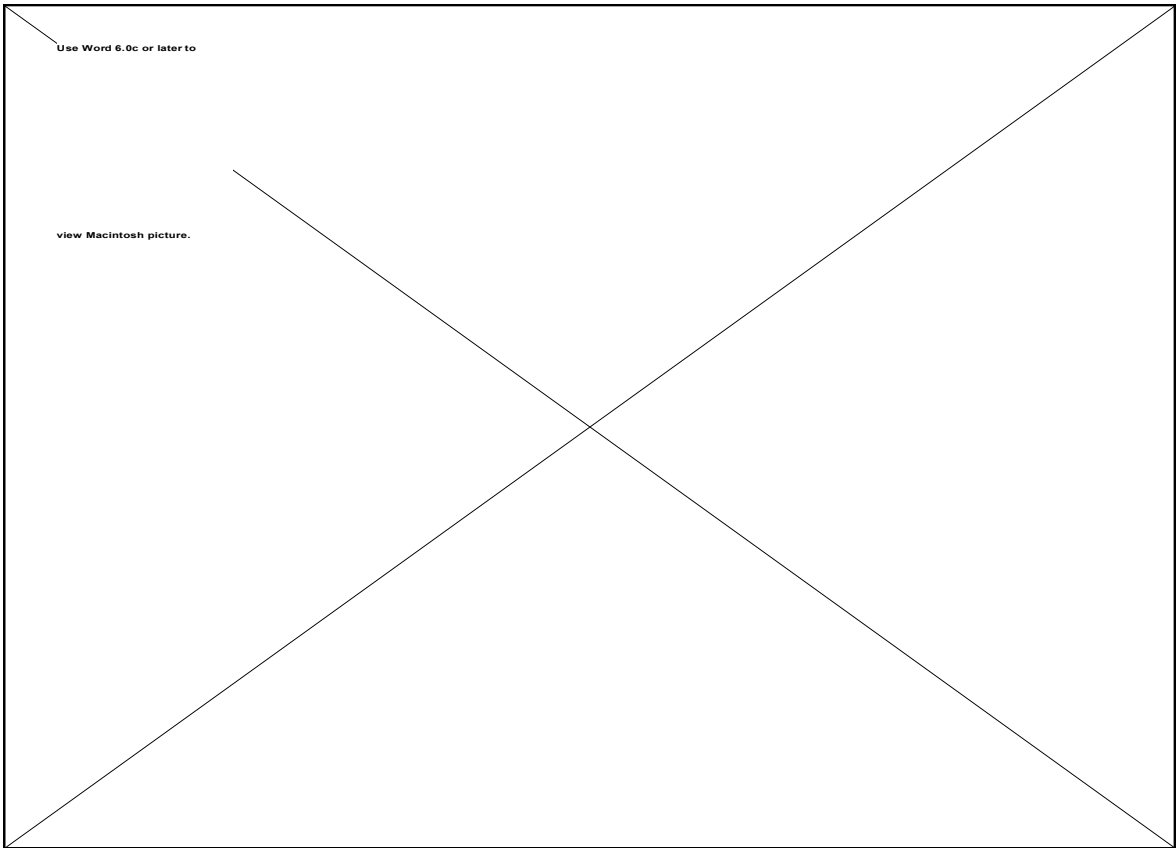


Figure 4.3. Area objects of the scene.

The hierarchy of the scene is shown in Figure 4.4.

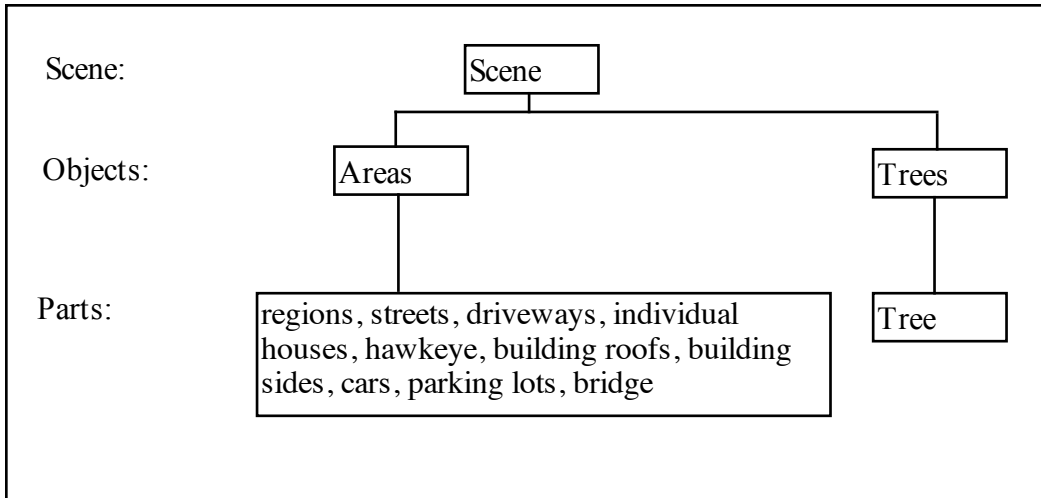


Figure 4.4. Scene Hierarchy - numbers in the parentheses indicate quantity

Script files were used to assemble the parts into objects and the objects into the scene. This made possible the accurate reassembling of the objects and the scene after changes were made to parts or parts were added. During the creation of the scene, the facets of the parts were assigned generic material attributes. Material attributes are divided between the materials database and the facet description. This division allows the most variable parameters of a material to be adjusted without creating a new material each time the parameter changed. In general, the default parameter values were used as the values are used by the therm model and therefore were not required for the “visible” images. The default values are shown in Table 4.2.

Table 4.2. Material Attributes

<b>Attribute</b>	<b>Value</b>	<b>Comments</b>
Material	Wood	Material type
Identification number	37	material identification number
Name	house side	part name
temperature	-1	Default.
thickness	5	Default.
power	-1	Default.
exp_area	-1	Default.
exvar1	null	Default.
exvar2	null	Default.
exvar3	null	Default.

The assignment of material attributes to parts that have many facets and many materials can be difficult. To make this process easier, complicated parts were broken up into multiple parts along material lines. All the facets of the same material were then grouped together as a part. After the geometric database was completed, the material attributes were adjusted to bring them in line with the reference imagery.

The topographical and land use information were inserted and used as templates for creating the different parts of the scene. The topography was created first, followed by the streets, driveways, sidewalks, houses, special buildings, the Driving Park bridge, the Hawkeye plant, and trees.

### *TOPOGRAPHY*

To create the topography the USGS and RGE map contour lines were digitized using a digitizing pad and then imported to ACAD as a layer. The USGS contour lines are

shown in Figure 4.5. The scale and rotation were adjusted to match the Land use data. (The contour lines were imported into a file containing the Land Use data.) Both the Land Use data (See Figure 4.2.) and the contour lines were then used as a template to create the topography.

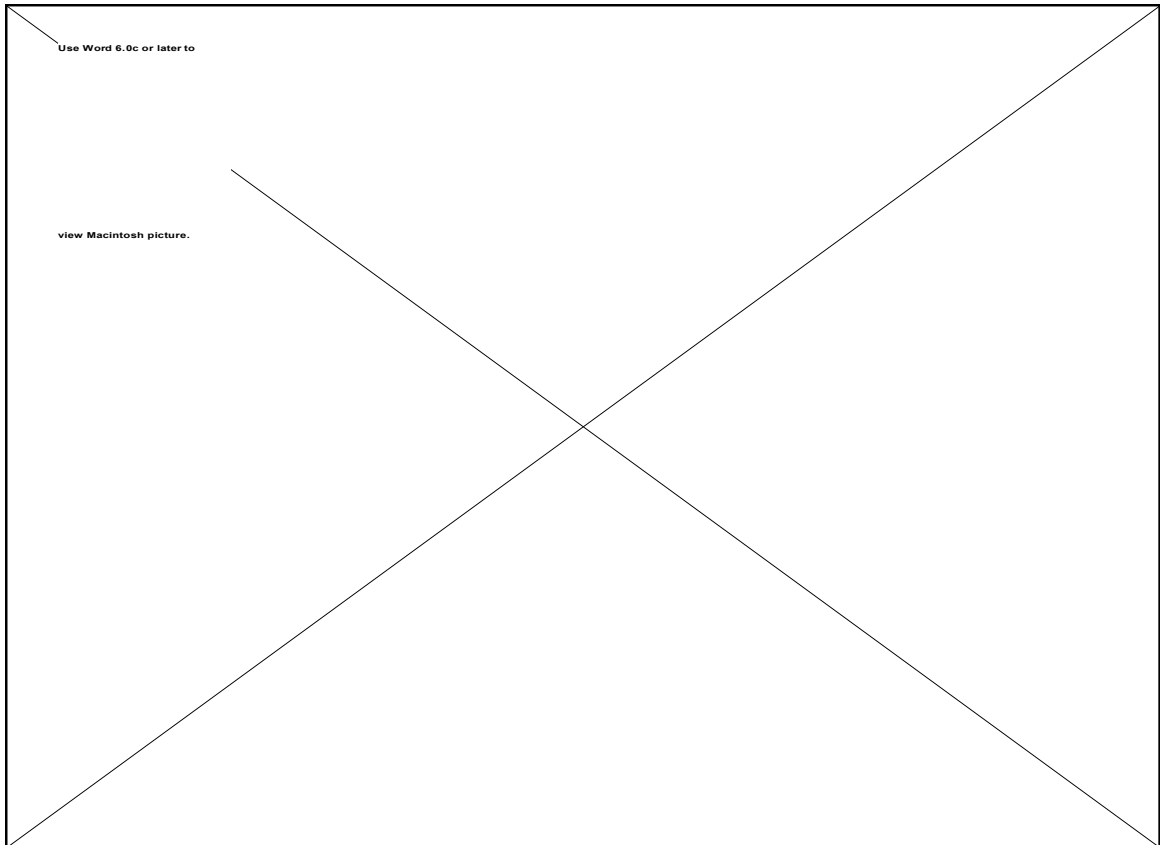


Figure 4.5. Digitized Topography Lines

The topography of the land in the target area has been formed by man to allow for roads, homes, and other buildings. An example of land forming is shown in Figure 4.6.

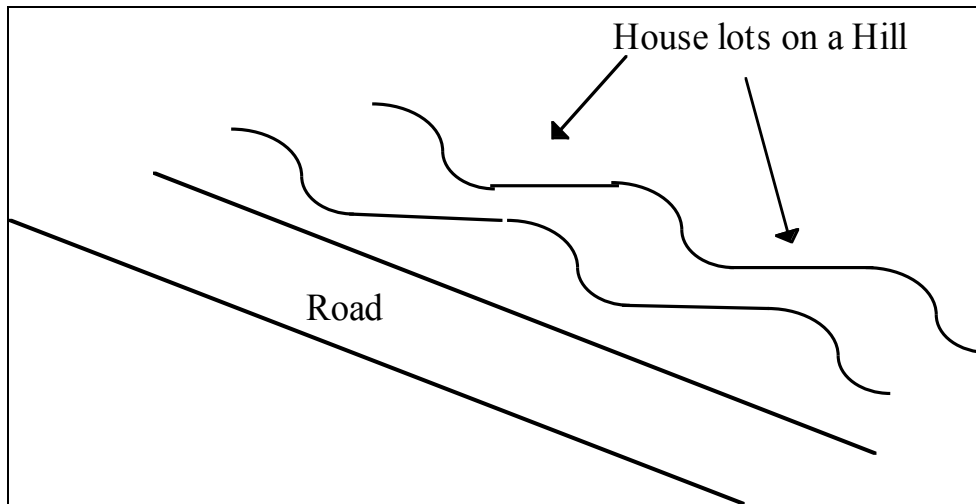


Figure 4.6. Land Forming

To accommodate land forming and the requirement for 3-4 sided facets, the borders of the facets match the borders of the land forming. A topography facet generally extends from one contour line to another contour line or to the edge of a street.

Since the create of this scene, the researcher has learned a better way to create the topography. The initial steps are the same as just described, the land use data and the contour lines are imported into AutoCAD as layers. After switching to a new layer, a mesh is then inserted. DIRSIG allows for meshes of up to 256 X 256. The vertices of the mesh are then moved interactively to intersection points between the contour lines and the land use data. This is performed in a nadir perspective. It is shown in Figure 4.7.

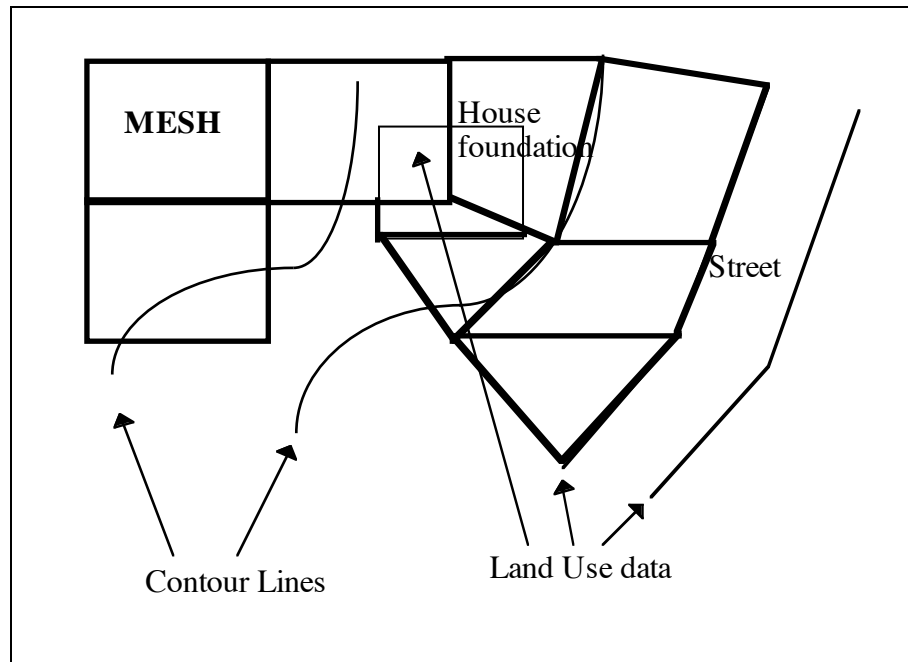


Figure 4.7. Alternative topography creation approach

The vertices of the mesh (shown in bold point) are moved to create facets that match the underlying data. The vertices of the “new” mesh are then elevated to the correct altitude. Using this approach should greatly reduce the time required to create the topography.

## HOUSES

Three generic houses and one garage were created for insertion into the scene. The houses are shown in Figures 4.8-4.11. A comparison of the house drawings and Images 4.2 and 4.3 shows that they capture their basic structure.

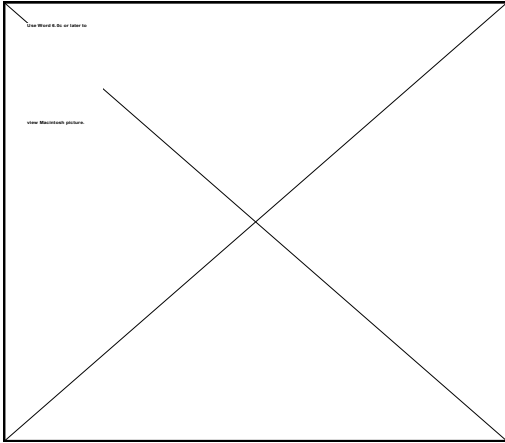


Figure 4.8. Fancy House

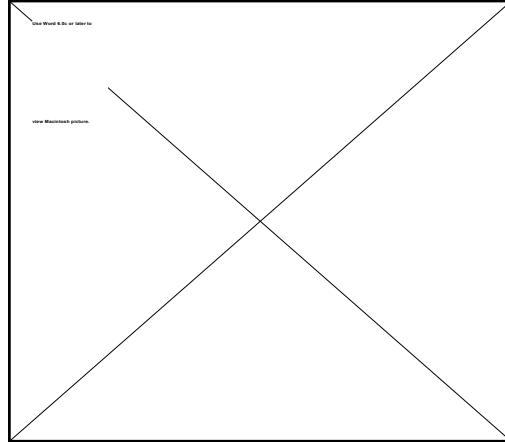


Figure 4.9. Garage

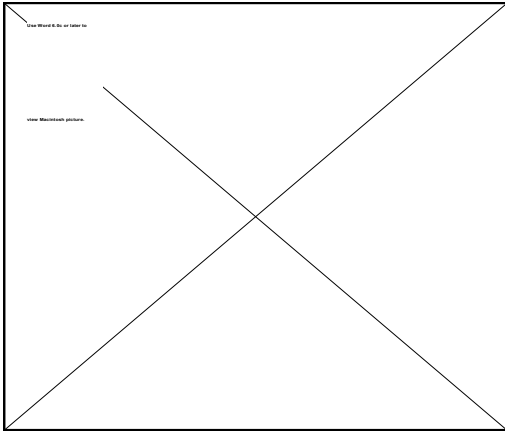


Figure 4.10. House 1

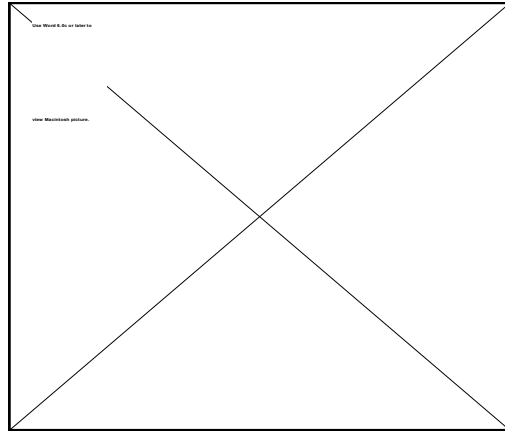


Figure 4.11. House 2

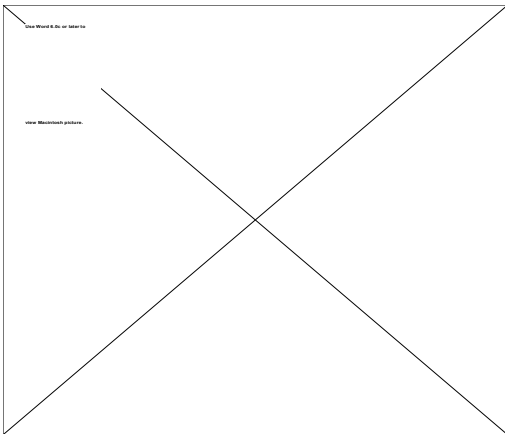


Image 4.2. Typical House 1

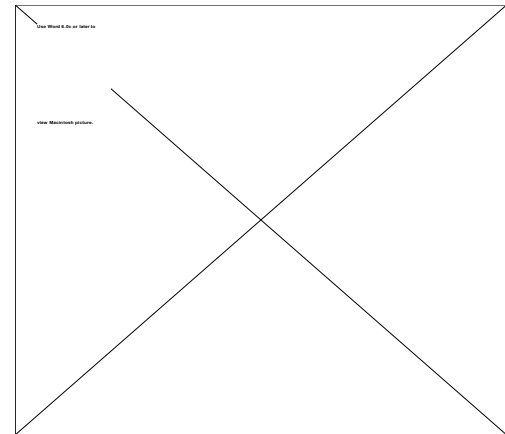


Image 4.3. Typical House 2

The scale of the house drawings is 1 unit by 1 unit. The houses were inserted using the land use data as a template for the latitude and longitude location and the scale in the horizontal directions (x, y). Figure 4.12 shows this process. The height of the houses ranges from 33 to 37 feet. The altitude above sea level was estimated using the topographical information.

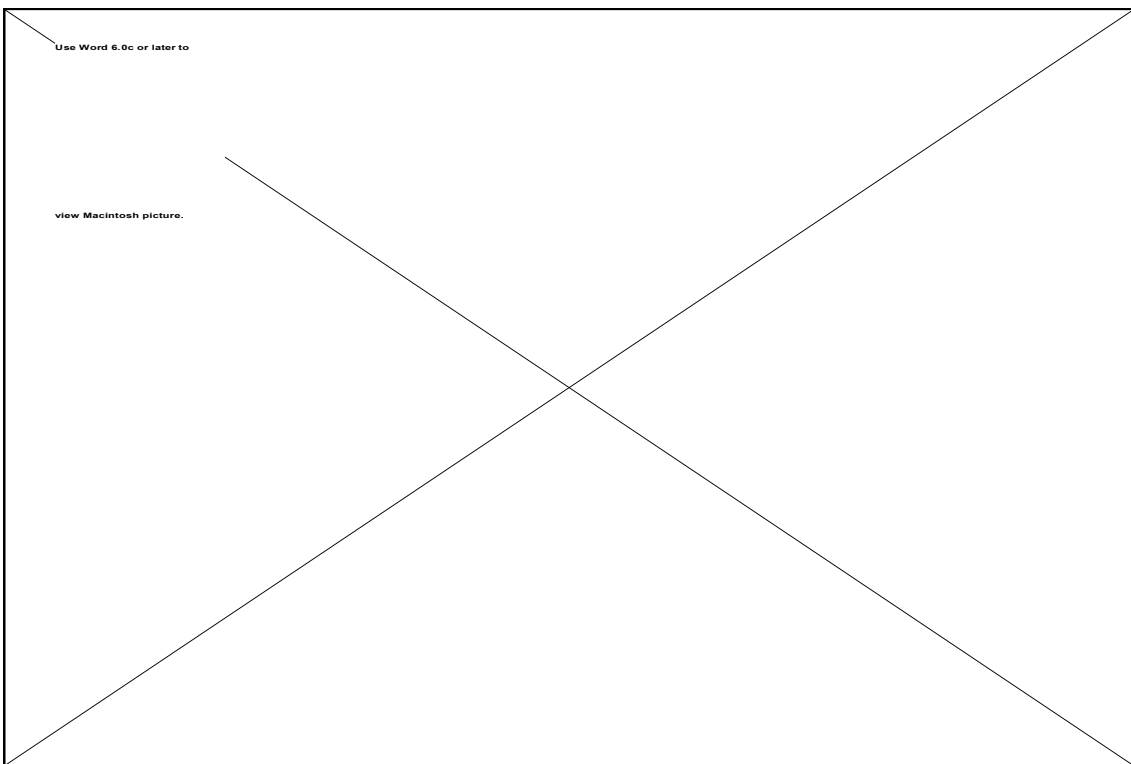


Figure 4.12. Insertion of house using the land use data as a template.

Once the houses were inserted, the location information was captured in a script file to allow for reassembling of the objects. To reduce the work required, ten different colored houses were created. The roof and porch roof are one color and the sides of the house and the porch are another color.

## OTHER STRUCTURES

Other structures such as churches, schools, and businesses were created individually, based on land use information and photos of the area. The land use data provided the location, scale, and rotation information. The heights of the buildings were estimated based on photos and experience. The structures were built at sea level and then moved to the correct altitude. Examples of the structures created are shown in Figures 4.13-4.16 and Images 4.4-4.7.

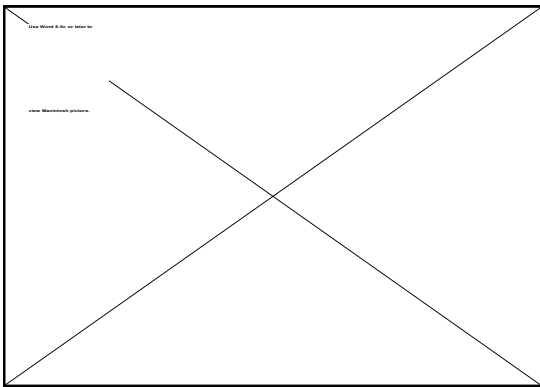


Figure 4.13. House 144

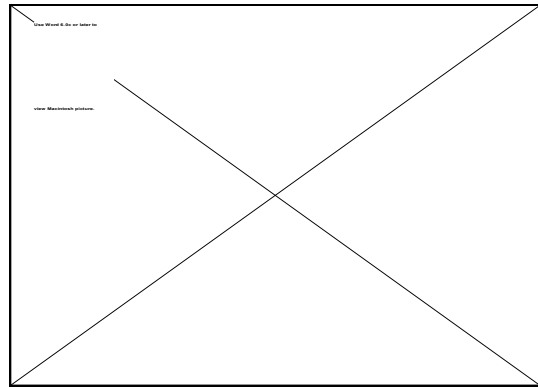


Figure 4.14. House 146

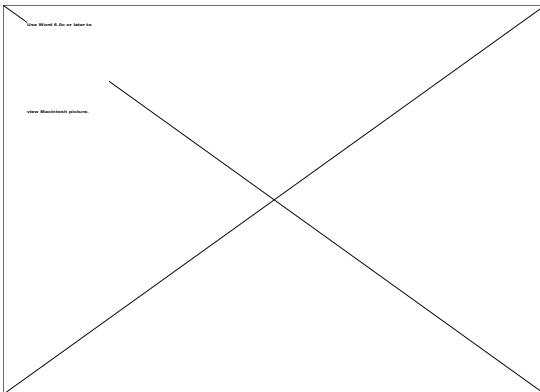


Image 4.4. Nazareth Hall School

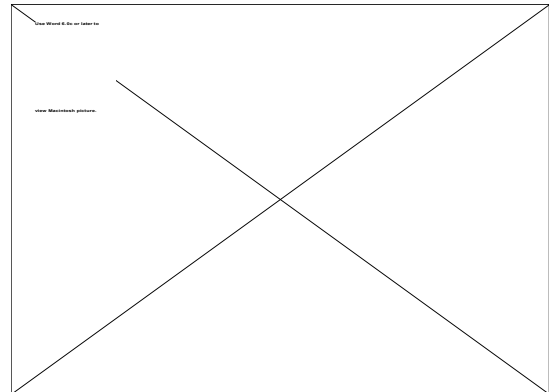


Image 4.5. Rochester School for the Deaf

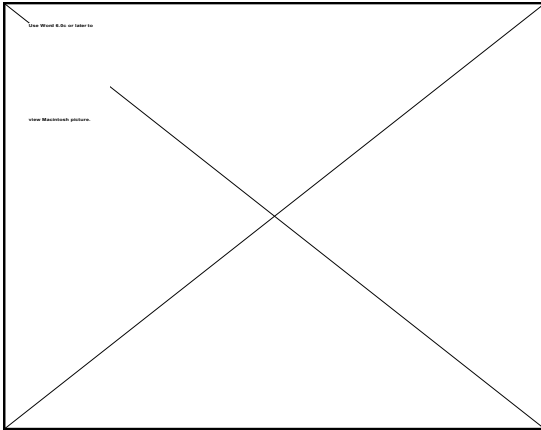


Figure 4.15. House 157

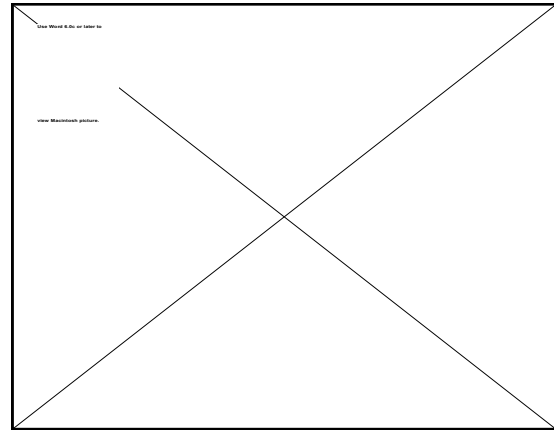


Figure 4.16. House 303

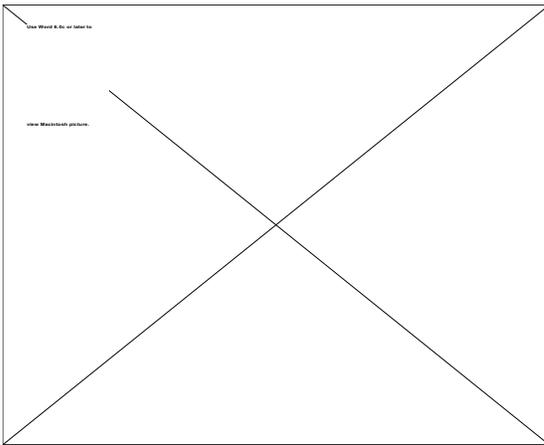


Image 4.6. Walter Hall Deaf.

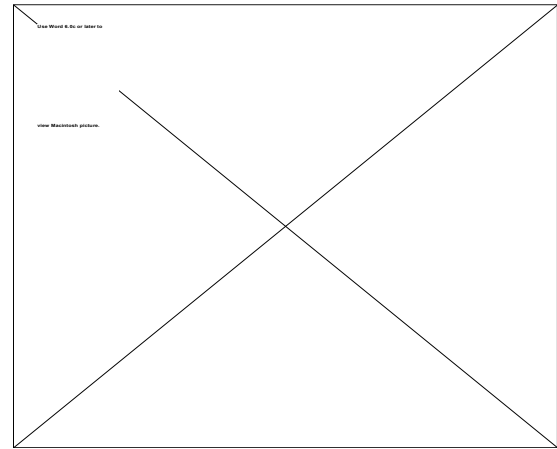


Image 4.7. Rochester School for the Deaf.

Again, all the location information was captured in a script file for use in reassembling the objects.

## STREETS

Land use and topographical data were used to determine the location and position of streets. An example of the streets for an object is shown in Figure 4.17.

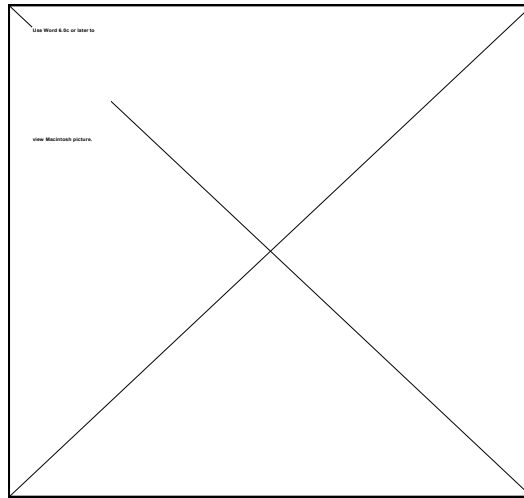


Figure 4.17. Streets in Region 41

Typically, the streets were elevated three to six inches to minimize error during the intersection testing on the facets to determine which facet is above the other.

#### SIDEWALKS/DRIVEWAYS/PARKING LOTS

Land use data and photos of the area were used to determine the location of sidewalks, driveways, and parking lots. The structures were created by either changing the material of a topography facet to match the material desired or by placing a facet over the topography facet. Typically, a six inch elevation was used. Examples of sidewalks and parking lots are shown in Figures 4.18 and 4.19.

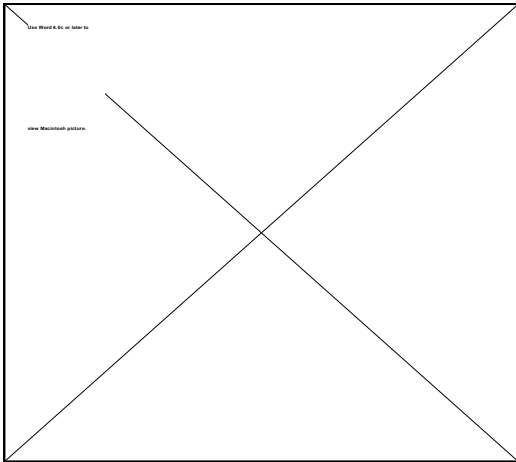


Figure 4.18. Sidewalks in Region 41

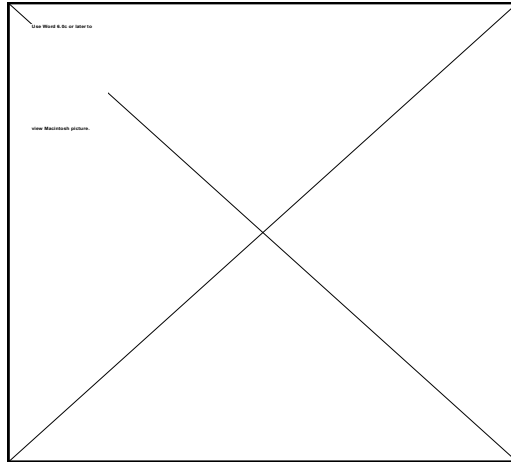


Figure 4.19. Parking Lots in Region 41

## TREES

Several type of trees were attempted throughout the scene creation process. The largest constraining factor was the number of facets the tree contained. The synthetic scene required approximately 3,000 trees so each tree was limited to 20 facets (20 facets/tree X 3,000 trees = 60,000 facets). The remaining facets were allocated to the remainder of the scene. This was adequate for low resolution images. However, as the resolution increased the trees became inadequate. This wasn't necessarily disadvantageous, since often as resolution increases the number of trees in the scene decreases thus allowing more facets to be allocated the trees. The location of the trees was determined from photos or ground surveys for the residential areas and were randomly placed for the forest in the gorge. The height of the trees were estimated and randomized (Side, 1996).

Typical trees are shown in Figures 4.20 (top view) and 4.21 (side view).

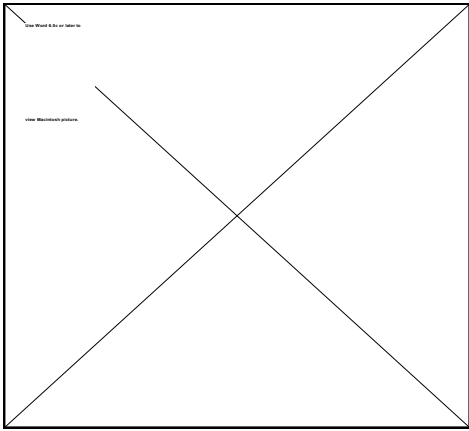
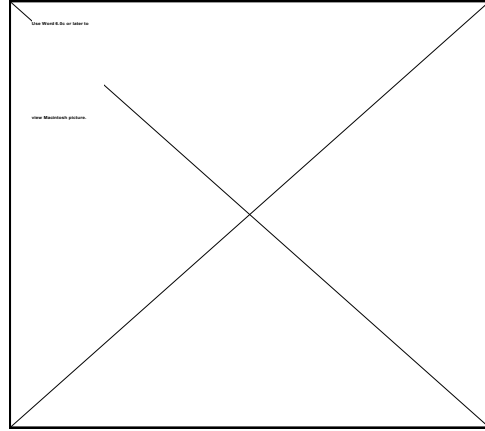


Figure 4.20. Trees - side view

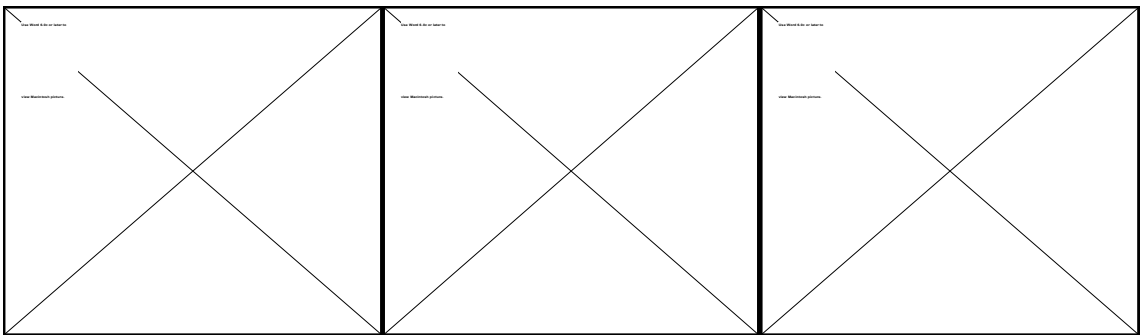


Figures 4.21. Trees - top view

## VEHICLES

Three generic vehicles (sedan, pick up, and van) were created to add context to the image. The scale of the vehicles was unity and scaled appropriately as they were inserted. The location, type, and color were determined randomly or through photos. The altitude was determined through trial and error.

The vehicles are shown in Figures 4.22-4.24.



Figures 4.22. Sedan

Figure 4.23. Pick-up truck

Figure 4.24. Mini-van

## BRIDGE

The Driving Park bridge object was created by Jim Salacain (1995) during his thesis work and was used as a template to create a part. Recreating the bridge as a part allowed the material attributes to be changed. The part and a photo of the bridge are shown in Figure 4.25 and Image 4.8. The only spatial changes to the part were position and scale which were adjusted when the part was inserted.

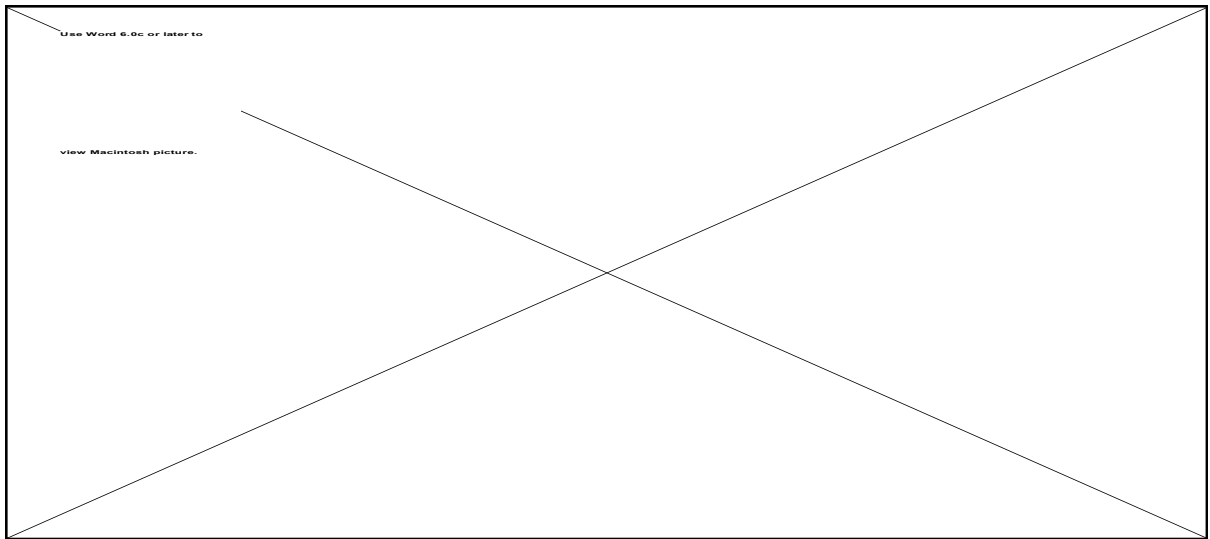


Figure 4.25. Driving Park Bridge, taken from Jim Salacain's Thesis Work

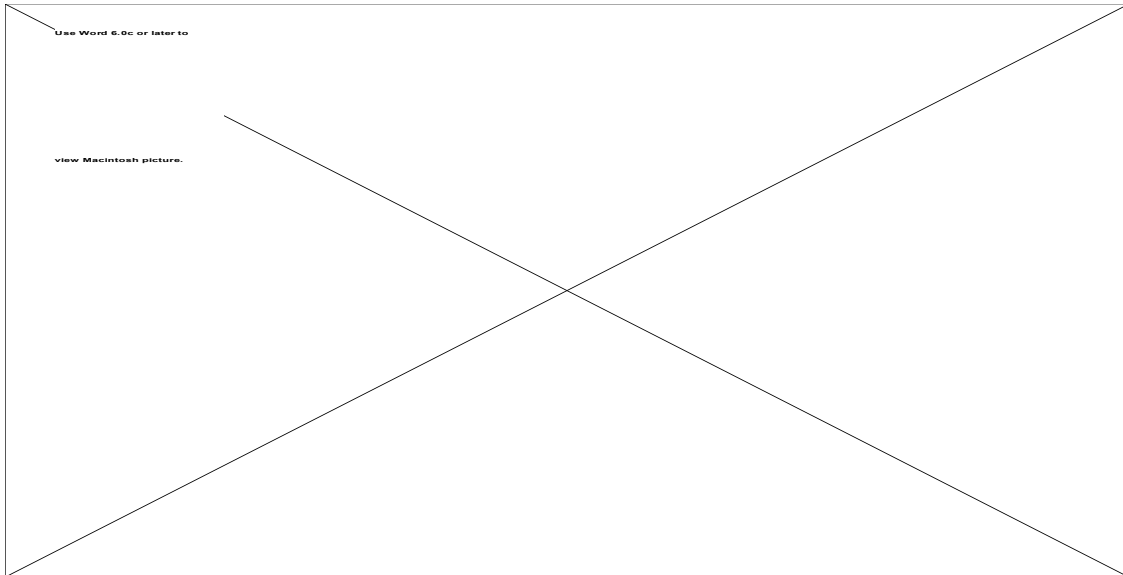


Image 4.8. Driving Park Bridge

## HAWKEYE

The Hawkeye plant object was also created by Jim Salacain during his thesis work and was used to create a part. In addition, windows and surface bricks were added to the part. The Hawkeye part and an image of Hawkeye are shown in Figure 4.26 and Image 4.9. The part position and scale were adjusted when it was inserted into the validation scene.

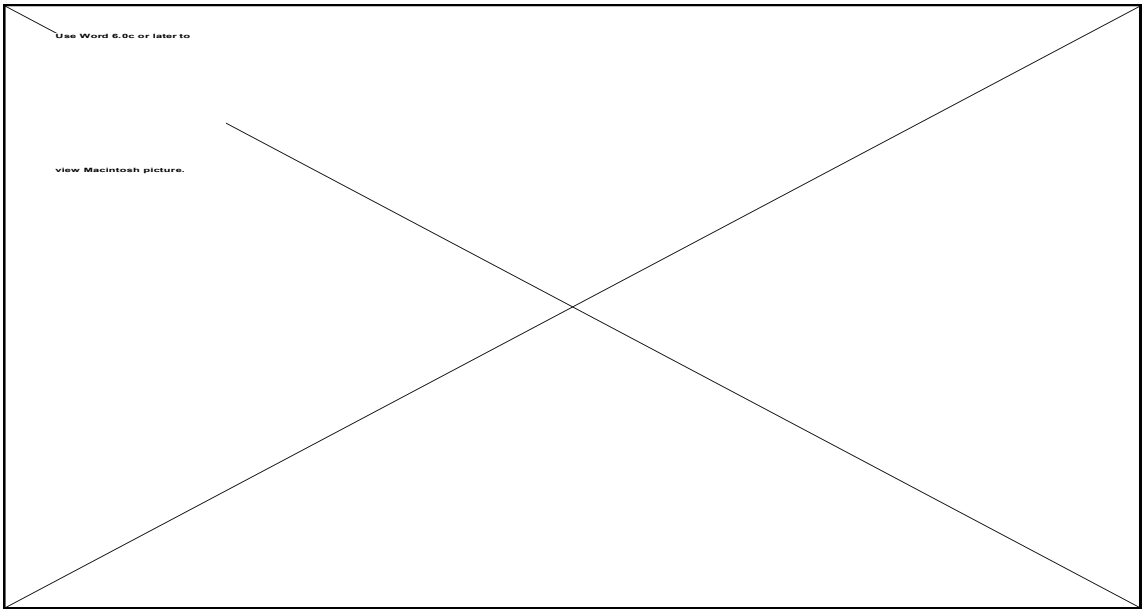


Figure 4.26. Hawkeye Plant, taken from Jim Salacain's Thesis work

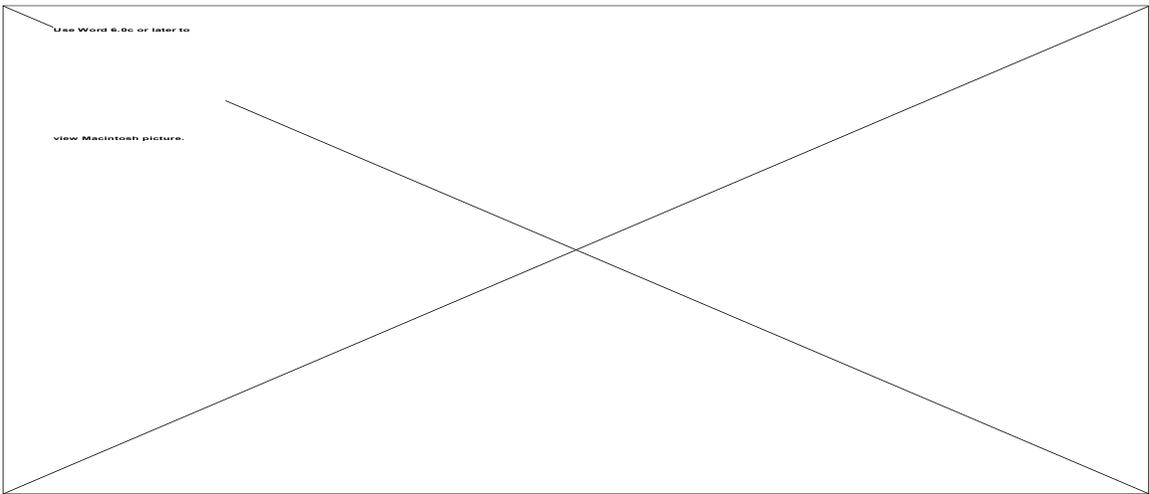


Image 4.9. Kodak Hawkeye Plant.

### 4.2.3.2 Creation of the Look Angle File (.adv file)

#### Source Data

The source data for the .adv were obtained by adjusting the view of the scene in ACAD, using the dview command, until it matched the actual image. The view settings; Target Point, Camera Point, Camera angles, and Camera Focal Length, were then recorded for inclusion in the .adv file. The image size varied depending on the purpose of the image created. If the image was used for incremental testing it was typically 16 pixels by 16 pixels to reduce DIRSIG runtime. The image size for the validation images was selected so that mixed pixels could be created. (Mixed pixels contain more than one material.)

#### File Creation

The .adv file was created using Word™ and saved as “Text Only” file. A sample of one of the .adv files used is shown in Figure 4.27.

1800 1800 465	<i>Target point (x,y,z) in ACAD units</i>
1700 1700 1600	<i>Camera Point (x,y,z) in ACAD units</i>
90 -91 0.0	<i>Camera Angles (elevation, azimuth, twist - degrees)</i>
40	<i>Camera focal length (mm)</i>
512 512	<i>Image Size (pixels; rows, columns)</i>

Figure 4.27. Sample .adv file

The target point corresponds to middle of the image at the level of the top of the gorge and is given in feet. The Camera Point corresponds to the location of the sensor in the reference image and is given in feet. The camera angles orient the camera to look at the target from its position and are given in degrees. The camera focal length is for the synthetic imager. The image size was adjusted based on the purpose of the image.

### 4.2.3.3 Creation of the Scene Node File (.snd file)

#### Source Data

Source data for the .snd file came from various sources. The minimum and maximum view angles were obtained by running the DIRSIG find\_min\_max\_view\_angle program. The program computes these angles based on the .adv and .gdb files. The program uses two approaches to compute the angles, “scene-bounding-box” and “field-of-view”. The “field-of-view” approach values were used based on the recommendations of the DIRS staff. The minimum and maximum frequency of the sensor were obtained from camera specification sheets. The remaining data was chosen to match the reference image data.

#### File Creation

The .snd file was created using Word™ and saved as a “Text Only” file. A sample of one of the .snd files used is shown in Figure 4.28.

1.0	sensor altitude (km)
3	number of spectral bands
14400.0 16800.0 60.0	min, max, increment freq of sensor (cm <sup>-1</sup> ) (Band 3)
16800.0 20000.0 80.0	min, max, increment freq of sensor (cm <sup>-1</sup> ) (Band 2)
20000.0 25000.0 125.0	min, max, increment freq of sensor (cm <sup>-1</sup> ) (Band 1)
-77.0 78.0 1.0	min, max, and increment for view angle
9 30 95	month, day, year of simulation
19	time of day (decimal, 24-hour, clock, GMT)
5	GMT offset for Buffalo, NY
43.08333 77.66667	latitude, longitude of the target

Figure 4.28. .snd file

The first field is the altitude of the sensor above sea level in km. The next field is the number of spectral bands in the image. Three bands were chosen for the validation. The next three lines give the bandpass of each channel. Each of these values correspond to the reference sensor. The frequency increment of the sensor was chosen such that the error in the radiance calculation was minimized. The next field is the minimum and maximum view angles of the sensor and the incremental view angle of the sensor. (See .rad file description.) The date and time correspond to the time the reference image was taken. The GMT offset for Rochester (and Buffalo) is five hours. The last two fields are the latitude and longitude of center of the target.

#### **4.2.3.4 Creation of the Radiosonde Data File (.rsd file)**

The creation of this file required the support of the DIRS staff to explain how to best deal with gaps in input data and variance in surface temperature conditions.

#### Source Data

The nearest location to the target area where radiosonde data are collected is the Buffalo Weather Service Office (WSO) at the Buffalo Airport. It is assumed that the meteorological conditions at the Buffalo Airport were similar to those over the target area.

Balloons are released twice a day at 0800L and 2000L. Measurements are taken at 50 millibar decrements, from 950 to 100 millibars, as the balloon rises. A measurement is also taken at ground level, for a total of 19 readings. The data are then put onto a computer network that can be accessed from the Rochester WSO. (See weather file for address and points of contact.) The data is not in a convenient layman readable format and must be translated. Arrangements to have the data accessed and translated at the

Rochester WSO were made a couple of weeks before the flyover. (The data was also obtained from the Buffalo WSO but did not arrive in a layman readable format.) The data from the Rochester WSO cost \$0.25 a page. Only one reading is required by DIRSIG, so the total cost was \$0.25. (Readings for the 48 hours before the flyover and the next reading after the flyover were also obtained.)

The flyover was at 1400L, about midway between two radiosonde readings. The two readings were compared and were found to be within a couple of degrees for the layers above the surface as shown in Table 4.3. To account for the time offset the Buffalo surface layer readings (Marked by \*\* in the table.) were replaced with Rochester Airport surface layer readings, i.e. 23.8 C was substituted for 11.6 C and 7.8 C for 7 C.

The atmospheric pressure (PRESSURE) is given in millibars (mb). The balloon height (HEIGHT) is given in feet (ft) and meters (m) above ground level (AGL). The temperature (TEMP) and dew point (DEWPT) are given in degrees Fahrenheit (F) and Celsius (C). If no data was available the field shows -999.

Table 4.3. Flyover Radiosonde Data

30 Sep 95	0800L			30 Sep 95	2000L	
Atmospheric pressure (millibars)	Balloon Altitude (km - AGL)	Atmospheric Temperature (C)	Dew Point (C)	Balloon Altitude (km - AGL)	Atmospheric Temperature (C)	Dew Point (C)
998	0.218	**23.8/11.6	**7.8/7	0.218	20.6	10.6
950	0.639	14.7	6.4	0.646	20.0	6.2
900	1.097	14.4	6.4	1.109	15.8	4.1
850	1.578	10.2	4.2	1.592	11.2	2.2
800	2.078	7.7	-13.8	2.088	6.6	-0.9
750	2.610	9.1	-17.7	2.616	3.2	-12.1
700	3.178	5.0	-20.0	3.180	4.0	-20.0
650	3.765	1.0	-22.2	3.762	-0.7	-23.3
600	4.399	-2.7	-24.9	4.398	-5.7	-26.8
550	5.088	-5.6	-28.3	5.074	-8.6	-30.1
500	5.843	-9.5	-31.5	5.823	-13.1	-33.1
450	6.636	-16	-36.6	6.607	-18.2	-37.5
400	7.523	-21.9	-40.9	7.483	-25.1	-44.1
350	8.474	-28.5	-34.8	8.421	-33.1	-50.1
300	9.573	-38.1	-41.2	9.503	-39.5	-54.5
250	10.803	-47.7	-50.8/-999	10.723	-48.5	-999
200	12.253	-56.9	-60.0/-999	12.153	-58.9	-999
150	14.043	-62.5	-65.6/-999	13.953	-61.1	-999
100	16.493	-68.5	-71.6/-999	16.453	-65.3	-999

File Creation

The .rsd file, shown in Figure 4.29, was created using Microsoft Excel™ and saved as a “text only tab-delimited” file.

0.218	998	23.8	7.8
0.639	950	14.7	6.4
1.097	900	14.4	6.4
1.578	850	10.2	4.2
2.078	800	7.7	-13.8
2.610	750	9.1	-17.7
3.178	700	5	-20
3.765	650	1	-22.2
4.399	600	-2.7	-24.9
5.088	550	-5.6	-28.3
5.843	500	-9.5	-31.5
6.636	450	-16	-36.6
7.523	400	-21.9	-40.9
8.474	350	-28.5	-34.8
9.573	300	-38.1	-41.2
10.803	250	-47.7	-50.7
12.253	200	-56.9	-59.9
14.043	150	-62.5	-65.5
16.493	100	-68.5	-71.5

Figure 4.29. .rsd file

The balloon altitude, column one, was converted from meters to kilometers and the altitude differential between sea level and ground level at Buffalo airport, 0.218 km, was added to each value. The atmospheric measurements, column two, are given in millibars. The Celsius temperature measurements, column three, were entered as provided except for the surface temperature. For that measurement, the temperature (23.8 C) at the Rochester airport was used. The Celsius dew point data, column four, were entered as provided except for the surface temperature. For that measurement, the local surface dew point (7.8 C) was used instead of the Buffalo measurement. Also, no data was available for the last four readings so the data extrapolated by maintaining the temperature

differential between the last valid dew point measurement and the temperature measurement, 3.1 C.

#### **4.2.3.5 Creation of the LOWTRAN card deck (.cdk file)**

The creation of this file required the support of the DIRS staff to clarify some of the explanations in the references.

##### Source Data

The source data for the creation of this file came from general imaging condition information such as the weather, location, time, etc..

##### File Creation

The file is created by running a DIRSIG program called CONTROL7. The program queries the user for inputs about the imaging conditions and then based on those inputs creates the card deck. The questions asked and the answers given are in Figure 4.30. Where appropriate comments are made.

```
ENTER FILE NAME FOR PRODUCED CARD DECK:    flyover.cdk

INPUT ATMOSPHERIC MODEL TYPE
MODEL=      0 IF METEOROLOGICAL DATA ARE SPECIFIED (HORIZONTAL PATH ONLY)
            1 TROPICAL ATMOSPHERE
            2 MID-LATITUDE SUMMER
            3 MID-LATITUDE WINTER
            4 SUB-ARCTIC SUMMER
            5 SUB-ARCTIC WINTER
            6 1976 U.S. STANDARD ATMOSPHERE
```

7 NEW MODEL ATMOSPHERE (RADIOSONDE DATA)

CHOOSE A MODEL NUMBER: 7

IS THE INPUT RADIOSONDE DATA (Y OR N)? y

INPUT THE TYPE OF ATMOSPHERIC PATH

ITYPE= 1 FOR A HORIZONTAL (CONSTANT PRESSURE) PATH  
2 VERTICAL OR SLANT PATH BETWEEN TWO ALTITUDES  
3 VERTICAL OR SLANT PATH TO SPACE

CHOOSE A TYPE: 2

PROGRAM EXECUTION MODE

IEMSCT= 0 PROGRAM EXECUTION IN TRANSMITTANCE MODE  
1 PROGRAM EXECUTION IN RADIANCE MODE  
2 PROGRAM EXECUTION IN RADIANCE MODE WITH SOLAR/LUNAR SCATTERED RADIANCE INCLUDED  
3 DIRECT SOLAR IRRADIANCE

ENTER EXECUTION MODE: 2

MULTIPLE SCATTERING EXECUTION MODE

IMULT= 0 PROGRAM EXECUTED W/OUT MULTIPLE SCATTERING  
1 PROGRAM EXECUTED WITH MULTIPLE SCATTERING

MULTIPLE SCATTERING MODE: 1

DO YOU WANT TO MODIFY THE DEFAULT ALTITUDE PROFILES OF TEMPERATURE AND PRESSURE (Y OR N)? n

DO YOU WANT TO MODIFY THE DEFAULT ALTITUDE PROFILE OF WATER VAPOR (Y OR N)? n

DO YOU WANT TO MODIFY THE DEFAULT ALTITUDE PROFILES OF OZONE (Y OR N)? n

DO YOU WANT TO MODIFY THE DEFAULT SEASONAL DEPENDENCE OF CH4 (Y OR N)? n

DO YOU WANT TO MODIFY THE DEFAULT SEASONAL DEPENDENCE OF N2O (Y OR N)? n

DO YOU WANT TO MODIFY THE DEFAULT SEASONAL DEPENDENCE OF CO (Y OR N)? n

DO YOU WANT TO PRINT THE ATMOSPHERIC PROFILES (Y OR N)? n

WHAT IS THE TEMPERATURE OF THE EARTH (BOUNDARY LAYER) IN DEGREES K (0.0 USES THE FIRST RADIOSONDE READING)? 0

ENTER THE SURFACE ALBEDO (0.00 IS A BLACKBODY) 0

SELECT AN AEROSOL EXTINCTION

IHAZE= 0 NO AEROSOL ATTENUATION INCLUDED IN CALCULATION  
1 RURAL EXTINCTION, 23-KM VIS.  
2 RURAL EXTINCTION, 5-KM VIS.  
3 NAVY MARITIME EXTINCTION, SETS OWN VIS.  
4 MARITIME EXTINCTION, 23-KM VIS.  
5 URBAN EXTINCTION, 5-KM VIS.  
6 TROPOSPHERIC EXTINCTION, 50-KM VIS.  
7 USER DEFINED AEROSOL EXTINCTION COEFFICIENTS TRIGGERS READING IREG FOR UP TO 4 REGIONS OF USER DEFINED EXTINCTION ABSORPTION AND ASSYMETRY  
8 ADVECTION FOG EXTINCTION, 0.2-KM VIS.  
9 RADIATION FOG EXTINCTION, 0.5-KM VIS.  
10 DESERT EXTINCTION SETS OWN VISIBILITY FROM WIND SPEED

CHOOSE AEROSOL EXTINCTION TYPE: 5 (The visibility is adjusted later.)

SELECT A SEASON

ISEASN= 0 DEFAULT SEASON FOR MODEL  
(SUMMER FOR MODELS 0,1,2,4,6,7)  
(WINTER FOR MODELS 3,5)  
1 SPRING-SUMMER  
2 FALL-WINTER

CHOOSE A SEASON: 2

SELECT A VOLCANIC AEROSOL EXTINCTION

IVULCN= 0 DEFAULT TO STRATOSPHERIC BACKGROUND  
1 STRATOSPHERIC BACKGROUND  
2 AGED VOLCANIC TYPE/MODERATE VOLCANIC PROFILE

3 FRESH VOLCANIC TYPE/HIGH VOLCANIC PROFILE  
 4 AGED VOLCANIC TYPE/HIGH VOLCANIC PROFILE  
 5 FRESH VOLCANIC TYPE/MODERATE VOLCANIC PROFILE  
 6 BACKGROUND STRATOSPHERIC TYPE/MODERATE VOLCANIC PROFILE  
 7 BACKGROUND STRATOSPHERIC TYPE/HIGH VOLCANIC PROFILE  
 8 FRESH VOLCANIC TYPE/EXTREME VOLCANIC PROFILE  
 CHOOSE A VOLCANIC EXTINCTION: **0**

**SPECIFY CLOUD/RAIN RATE MODEL**

ICLD = 0 NO CLOUDS OR RAIN  
 1 CUMULUS CLOUD BASE .66KM TOP 2.7KM  
 2 ALTOSTRATUS CLOUD BASE 2.4KM TOP 3.0KM  
 3 STRATUS CLOUD BASE .33KM TOP 1.0KM  
 4 STRATUS/STRATO CUMULUS BASE .66KM TOP 2.0KM  
 5 NIMBOSTRATUS CLOUD BASE .16KM TOP .66KM  
 6 2.0MM/HR DRIZZLE (MODELED WITH CLOUD 3) RAIN 2.0MM/HR AT 0KM TO .22MM/HR AT 1.5KM  
 7 5.0MM/HR LIGHT RAIN (MODELED WITH CLOUD 5) RAIN 5.0MM/HR AT 0KM TO .2MM/HR AT 1.5KM  
 8 12.5MM/HR MODERATE RAIN (MODELED WITH CLOUD 5) RAIN 12.5MM/HR AT 0KM TO .2MM/HR AT 2.0KM  
 9 25.0MM/HR HEAVY RAIN (MODELED WITH CLOUD 1) RAIN 25.0MM/HR AT 0KM TO .2MM/HR AT 3.0KM  
 10 75.0MM/HR EXTREME RAIN (MODELED WITH CLOUD 1) RAIN 75.0MM/HR AT 0KM TO .2MM/HR AT 3.5KM  
 11 USER DEFINED CLOUD EXTINCTION, ABSORPTION, AND AEROSOL EXT. COEFFICIENTS' TRIGGERS READING IREG FOR UP TO 4 REGIONS OF EXTINCTION ABSORPTION + ASSYMETRY  
 18 STANDARD CIRRUS MODEL  
 19 SUB VISUAL CIRRUS MODEL  
 20 NOAA CIRRUS MODEL (LOWTRAN 6)

CHOOSE A CLOUD MODEL: **0**

DO YOU WANT TO USE ARMY VERTICAL STRUCTURE ALGORITHM FOR AEROSOLS IN BOUNDARY LAYER (Y OR N)? **n**  
 DO YOU WANT TO OVERRIDE THE DEFAULT VISIBILITY (Y OR N)? **y**  
 VISIBILITY (KM)? **23**  
 WHAT IS THE RAIN RATE? (MM/HR) **0**  
 WHAT IS THE GROUND ALTITUDE ABOVE SEA LEVEL? (KM) **0.218 (Target altitude)**  
 ENTER NUMBER OF ATMOSPHERIC LEVELS TO BE INSERTED: **19**  
 ENTER NAME OF NEW ATMOSPHERE: **hawkeye**  
 DO YOU WANT TO READ IN AEROSOL CONTROL BY LAYER (Y OR N)? **n**

WHAT FILE CONTAINS THE RADIOSONDE DATA? NOTE: DATA LINES MUST LIST ALTITUDE IN KM, PRESSURE IN MBARS, TEMPERATURE IN DEG(C), AND DEW POINT TEMP (TD IN T(C)) RESPECTIVELY. **30Sep95800L.rsd**

ENTERING DATA FOR LAYER 1: **ALTITUDE 0.2180000**  
 ENTERING DATA FOR LAYER 2: **ALTITUDE 0.6390000**  
 ENTERING DATA FOR LAYER 3: **ALTITUDE 1.097000**  
 ENTERING DATA FOR LAYER 4: **ALTITUDE 1.578000**  
 ENTERING DATA FOR LAYER 5: **ALTITUDE 2.078000**  
 ENTERING DATA FOR LAYER 6: **ALTITUDE 2.610000**  
 ENTERING DATA FOR LAYER 7: **ALTITUDE 3.178000**  
 ENTERING DATA FOR LAYER 8: **ALTITUDE 3.765000**  
 ENTERING DATA FOR LAYER 9: **ALTITUDE 4.399000**  
 ENTERING DATA FOR LAYER 10: **ALTITUDE 5.088000**  
 ENTERING DATA FOR LAYER 11: **ALTITUDE 5.843000**

```

ENTERING DATA FOR LAYER      12:  ALTITUDE  6.636000
ENTERING DATA FOR LAYER      13:  ALTITUDE  7.523000
ENTERING DATA FOR LAYER      14:  ALTITUDE  8.474000
ENTERING DATA FOR LAYER      15:  ALTITUDE  9.573000
ENTERING DATA FOR LAYER      16:  ALTITUDE 10.803000
ENTERING DATA FOR LAYER      17:  ALTITUDE 12.253000
ENTERING DATA FOR LAYER      18:  ALTITUDE 14.043000
ENTERING DATA FOR LAYER      19:  ALTITUDE 16.493000

ENTER H1, INITIAL ALTITUDE (KM) (OBSERVER POSITION):      0.237 (Sensor altitude updated by .snd file)
ENTER H2, FINAL ALTITUDE (KM):      0.218
ENTER INITIAL ZENITH ANGLE (DEGREES) AS MEASURED FROM INITIAL ALTITUDE
(NOTE: 0 LOOKS STRAIGHT UP, 180 STRAIGHT DOWN):      109.29
ENTER PATH (RANGE) LENGTH (KM):      0
ENTER EARTH CENTER ANGLE SUBTENDED BY H1 AND H2 (DEGREES):      n
DO YOU WANT TO OVERRIDE THE DEFAULT EARTH RADIUS (Y OR N)?      n
USE THE SHORT PATH FROM OBSERVER'S TO FINAL ALTITUDE (Y OR N)?      y

SPECIFY THE GEOMETRY OF THE OBSERVATION
IPARM =      0 SPECIFY
              1 OBSERVER LATITUDE
              2 OBSERVER LONGITUDE
              3 SOURCE LATITUDE
              4 SOURCE LONGITUDE
IPARM =      1 SPECIFY
              1 OBSERVER LATITUDE
              2 OBSERVER LONGITUDE
IPARM =      2 SPECIFY
              1 AZIMUTHAL ANGEL
              2 ZENITH ANGLE OF THE SUN
CHOOSE A TYPE OF GEOMETRY SPECIFICATION:      1

IPH =      0 HENYEY-GREENSTEIN AEROSOL PHASE FUNCTION
              1 USER SUPPLIED AEROSOL PHASE FUNCTION
              2 MIE GENERATED DATA BASE OF AEROSOL PHASE FUNCTIONS FOR THE LOWTRAN MODELS
ENTER PHASE FUNCTION TYPE:      2

ENTER THE DAY OF THE YEAR (I.E. FROM 1 TO 365):      273
ENTER OBSERVER LATITUDE (-90 TO 90):      43.083
ENTER OBSERVER LONGITUDE (0 TO 360):      77.667
ENTER TIME OF DAY IN DECIMAL HOURS:      1400.0
ENTER PATH AZIMUTH AS DEGREES EAST OF NORTH:      274.57
WHAT UNITS ARE YOU USING FOR WAVELENGTH? (MICRONS OR NANOMETERs):      microns
INPUT STARTING AND ENDING WAVELENGTH ON BANDPASS      0.4-0.7
HOW MANY INTERVALS ACROSS BANDPASS? (MAXIMUM 396)      396

IRPT=      0 TO END LOWTRAN 6 RUN
              1 TO READ ALL DATA CARDS AGAIN
              3 TO READ ONLY CARD 3 AGAIN (GEOMETRY DATA)
              4 TO READ ONLY CARD 4 AGAIN (WAVELENGTH RANGE)
SELECT IRPT:      0
=====

```

Figure 4.30. LOWTRAN Input.

The resulting .cdk file is shown in Figure 4.31.

```

7 2 2 1 0 0 0 0 0 0 1 1 1 0.000 0.00
5 2 0 1 0 0 0.000 0.000 0.000 0.000 0.218
19 0 0HAWKEYE
0.218 0.998E+03 0.238E+02 0.780E+01 0.000E+00 0.000E+00ABG
0.639 0.950E+03 0.147E+02 0.640E+01 0.000E+00 0.000E+00ABG
1.097 0.900E+03 0.144E+02 0.640E+01 0.000E+00 0.000E+00ABG
1.578 0.850E+03 0.102E+02 0.420E+01 0.000E+00 0.000E+00ABG
2.078 0.800E+03 0.770E+01-0.138E+02 0.000E+00 0.000E+00ABG
2.610 0.750E+03 0.910E+01-0.177E+02 0.000E+00 0.000E+00ABG
3.178 0.700E+03 0.500E+01-0.200E+02 0.000E+00 0.000E+00ABG
3.765 0.650E+03 0.100E+01-0.222E+02 0.000E+00 0.000E+00ABG
4.399 0.600E+03-0.270E+01-0.249E+02 0.000E+00 0.000E+00ABG
5.088 0.550E+03-0.560E+01-0.283E+02 0.000E+00 0.000E+00ABG
5.843 0.500E+03-0.950E+01-0.315E+02 0.000E+00 0.000E+00ABG
6.636 0.450E+03-0.160E+02-0.366E+02 0.000E+00 0.000E+00ABG
7.523 0.400E+03-0.219E+02-0.409E+02 0.000E+00 0.000E+00ABG
8.474 0.350E+03-0.285E+02-0.348E+02 0.000E+00 0.000E+00ABG
9.573 0.300E+03-0.381E+02-0.412E+02 0.000E+00 0.000E+00ABG
10.803 0.250E+03-0.477E+02-0.507E+02 0.000E+00 0.000E+00ABG
12.253 0.200E+03-0.569E+02-0.599E+02 0.000E+00 0.000E+00ABG
14.043 0.150E+03-0.625E+02-0.655E+02 0.000E+00 0.000E+00ABG
16.493 0.100E+03-0.685E+02-0.715E+02 0.000E+00 0.000E+00ABG
0.237 0.218 109.290 0.000 0.000 0.000 0
1 2 273 0
43.083 77.667 0.000 0.000 14.000 274.570 0.000 0.000
2000.000 3333.333 5.000
0

```

Figure 4.31. .cdk file

The file is basically the inputs to the questions formatted correctly for input to LOWTRAN. (See Section 4.2.3.7 Creation of the Radiance Files.) The program also re-defines some of the radiosonde data.

#### 4.2.3.6 Creation of the Weather File (.wth file)

##### Data Source

Weather data for the flyover was obtained from

National Oceanic and Atmospheric Administration (NOAA)  
National Weather Service Office (WSO) - Rochester  
1 Airport Way  
Rochester, NY 14624  
(716) 328-7633 (Observation Room Number)

Two weeks before the flyover, the WSO was contacted for support. They agreed to save the data, which they usually only keep for a limited time, for pick up after the flyover. The data was in the form of printouts and four printouts were needed to cover the 48 hours required for the weather file. Copies of the printouts cost \$0.25 a piece for a total cost of \$1.00. The data obtained from the WSO is shown in Appendix A.

The WSO collects data at the airport, which is approximately three miles south of the target area. This proximity allowed the airport weather data to be used for the target area. The data is collected once an hour. The time field (Time) is in local time on a 24 hour clock without adjustment for daylight savings time. At this time of year one hour must be added. The temperature (Temp) and dew point (Dp) are in degrees Fahrenheit. The wind speed (Wnd) is in Knots. The first three numbers are the direction the wind is coming from and the last number is the speed. The surface barometric pressure (Asi) is in millibars. The data is given in three digits, with the 1 assumed if the pressure is above 1000 millibars.

The cloud information is described in layers. Time data is structured as described above. The next field (Tot. Sky) describes in tenths the total amount of the sky obscured by clouds by all the layers. The cloud condition is described as clear (CLR) if the obscuration is 0/10, scattered (SCT) if the obscuration is less than 6/10, broken (BKN) if

the obscuration is 6/10 - 9/10, and overcast if the obscuration is greater than 9/10. Each layer lists the amount (Amt) of obscuration in tenths, the cloud type (Type), and the height (Hgt) of the bottom of the layer above sea level. The cloud types during this period were Cirrus (CI), Altocumulus (AC), and Stratocumulus (SC). The height field only allows for three digits so 2500 ft is listed as 250 and 60,000 ft is listed as 60. The last field describes the total opaqueness (Tot. Opq) of the sky in tenths.

#### File Creation

The .wth file was created using Microsoft Excel™ and saved as a “text only tab-delimited” file. The file is shown in Figure 4.32.

48	1											
0	8	1030	-1	4	2	0	0	1	0	0	0	0
1	5	1030	-1	3	0	0	0	1	0	0	0	0
2	6	1030	-1	4	2	0	0	1	0	0	0	0
3	5	1029	-1	3	2	0	0	1	0	0	0	0
4	4	1029	-1	2	1	0	0	1	0	0	0	0
5	4	1029	-1	3	1	0	0	1	0	0	0	0
6	4	1028	-1	2	0	0	0	1	0	0	0	0
7	4	1029	-1	3	0	0	0	0.95	1	0	0	0
8	7	1030	-1	5	2	0	0	0.95	1	0	0	0
9	10	1030	-1	7	2	0	0	0.95	1	0	0	0
10	14	1030	-1	8	2	0	0	0.95	1	0	0	0
11	19	1030	-1	9	2	0	0	1	0	0	0	0
12	21	1029	-1	10	3	0	0	1	0	0	0	0
13	23	1027	-1	12	2	0	0	1	0	0	0	0
14	24	1026	-1	11	2	0	0	1	0	0	0	0
15	26	1025	-1	11	2	0	0	0.95	5	0	0	0
16	26	1023	-1	11	4	0	0	0.95	5	0	0	0
17	26	1023	-1	11	2	0	0	0.8	5	0	0	0
18	23	1022	-1	12	4	0	0	0.7	5	0	0	0
19	22	1022	-1	12	3	0	0	0.8	1	0	0	0
20	20	1022	-1	11	3	0	0	0.8	1	0	0	0
21	18	1022	-1	11	3	0	0	0.9	1	0	0	0
22	18	1024	-1	11	2	0	0	1	0	0	0	0
23	17	1024	-1	10	2	0	0	1	0	0	0	0
24	17	1024	-1	10	2	0	0	1	0	0	0	0
25	16	1024	-1	11	3	0	0	0.95	1	0	0	0
26	16	1024	-1	11	3	0	0	0.95	1	0	0	0
27	15	1024	-1	10	3	0	0	0.95	1	0	0	0
28	13	1024	-1	8	2	0	0	0.95	1	0	0	0
29	13	1024	-1	8	2	0	0	0.95	1	0	0	0
30	12	1024	-1	8	2	0	0	0.95	1	0	0	0
31	12	1025	-1	8	2	0	0	0.9	1	0	0	0
32	13	1025	-1	8	2	0	0	0.9	1	0	0	0
33	16	1027	-1	9	2	0	0	0.7	1	0	0	0
34	16	1027	-1	8	3	0	0	0.7	1	0	0	0
35	18	1028	-1	10	4	0	0	0.7	1	0	0	0
36	19	1026	-1	10	3	0	0	0.7	1	0	0	0
37	21	1025	-1	10	4	0	0	0.8	1	0	0	0
38	23	1022	-1	9	2	0	0	0.8	1	0	0	0
39	23	1019	-1	8	2	0	0	0.8	1	0	0	0
40	24	1016	-1	7	4	0	0	0.8	1	0	0	0
41	24	1015	-1	6	2	0	0	0.7	1	0	0	0
42	23	1014	-1	7	2	0	0	0.6	1	0	0	0
43	21	1013	-1	8	2	0	0	0.6	1	0	0	0
44	19	1014	-1	8	2	0	0	0.6	1	0	0	0
45	17	1014	-1	9	3	0	0	0.7	1	0	0	0
46	16	1014	-1	9	3	0	0	0.7	1	0	0	0
47	15	1013	-1	8	3	0	0	0.9	1	0	0	0
48	14	1013	-1	8	2	0	0	1	0	0	0	0

Figure 4.32. .wth file

The first row gives the number of lines of weather data and the time increment (hours) between lines. After the first row, column one gives the time relative to midnight of the day before the simulation. DIRSIG assumes that the time of simulation occurs in the second 24 hours of data. Therefore, 48 lines of data (1 hour increments) were entered. (Technically, 38 hours of data would have been enough since the simulation was at 1400L of the second day,  $24 + 14 = 38$ .) Column two gives the temperature in degrees Celsius. To convert the data into degrees Celsius, the formula  $=INT((## - 32)*5/9)$  was used. Column three gives the atmospheric pressure in millibars. Column four gives the relative humidity and was given a value of -1, indicating dew point data would be used. Column five gives the dew point in degrees Celsius. The same formula given above used again to convert the temperatures from Fahrenheit to Celsius. Column six gives the wind speed in m/s. The measured data was converted from Knots to the m/s using the formula  $=INT(##*0.51444)$ . Columns seven and eight, direct and indirect insolation data, were assigned a value of zero because this information is not required for a simulation in the visible region, they are required by the THERM submodel. Column nine gives the sky exposure as a fraction (0 = cloudy, 1 = clear). The values were taken from the Tot. Opq. column of the weather data. The scaling convention is the reverse of that used by DIRSIG, therefore the values entered into the database are  $=1 - \text{Tot. Opq.}$ . When there were clouds present but the Tot. Opq. was clear (0), a value of 0.95 was entered in the weather file. Column ten gives the cloud type and was assigned to the dominate type of clouds present. During the 48 hours, only Cirrus, Alto-Cirrus, and Strato-Cirrus clouds were present. Columns eleven, twelve, and thirteen describe the precipitation conditions. Since there was no precipitation, zeros were assigned.

### 4.2.3.7 Creation of the Radiance Files (.rad files)

#### Source Data

The source data for the .rad files consist of the contents of the .cdk and .snd files.

#### File Creation

The .rad files are created by running a DIRSIG program called build\_radiance. Three files were created, one for each band. Part of a radiance file is shown in Figure 4.33.

1.000000				<b>Sensor Altitude (km)</b>
0.595238				<b>min wavelength (micron)</b>
0.694444				<b>max wavelength</b>
14400.000000				<b>min wavenumber (cm<sup>-1</sup>)</b>
16800.000000				<b>max wavenumber</b>
400.000000				<b>freq increment (degrees)</b>
7				<b># of increments</b>
-77.000000				<b>min view angle (degrees)</b>
78.000000				<b>max view angle</b>
2.000000				<b>view angle incr. (degrees)</b>
999.000000				<b>N/A</b>
79				<b># of increments</b>
0.595238	16800.000000	1.778084e-01	0.166068	<b>λ,wavenumber,Es, t1</b>
0.609756	16400.000000	1.730206e-01	0.182251	<b>“ (Es - W/cm<sup>2</sup>cm<sup>-1</sup>)</b>
0.625000	16000.000000	1.640234e-01	0.191867	<b>“ (t1 - as a fraction)</b>
0.641026	15600.000000	1.614799e-01	0.201759	<b>“</b>
0.657895	15200.000000	1.443334e-01	0.210500	<b>“</b>
0.675676	14800.000000	1.508868e-01	0.226116	<b>“</b>
0.694444	14400.000000	1.441539e-01	0.220623	<b>“</b>
-77.000000	3.476312			<b>view angle, range to earth</b>
0.075898	3.268046e-31	2.798746e-03		<b>t2, Lue, Lus</b>
0.085772	2.038844e-30	2.913450e-03		<b>“ (view angle - degrees)</b>
0.091580	1.246455e-29	2.748693e-03		<b>“ (range to earth - degrees)</b>
0.097715	7.591335e-29	2.682662e-03		<b>“ (Lue - W/cm<sup>2</sup>cm<sup>-1</sup>sr)</b>
0.103212	4.593620e-28	2.339971e-03		<b>“ (Lus - W/cm<sup>2</sup>cm<sup>-1</sup>sr)</b>
0.113674	2.779834e-27	2.469394e-03		<b>“ (t2 - as a fraction)</b>
0.109225	1.612141e-26	1.991768e-03		<b>“</b>
-75.000000	3.021416			

0.106150	3.250604e-31	2.545822e-03
0.138873	4.535199e-28	2.117841e-03

Figure 4.33. Part of a .rad file

The contents of this file are described in the (inserted) bold type.

#### **4.2.3.8 Creation of the Materials File (.mat file)**

The base parameters that describe the attributes of each material, except for temperature, are contained in the materials file. For efficiency, the parameters of a material that have variability from facet to facet (temperature, thickness, self-generated power, and exposed area) are also contained in the geometric database.

#### Data Sources:

The source of data is DCS Corporation literature which lists the parameters required for its Thermal Model for over 200 hundred materials. (The Thermal Model is incorporated into DIRSIG as the therm submodel.) The parameters listed for each material include the material's name, (mass) density, specific heat, thermal conductivity, thickness, visible emissivity, thermal emissivity, exposed area, and self-generated power. In addition to these parameters, the material's optical description, specularity, and emissivity filename are required for the material database. Source data for the optical description was not required as all of the materials used in the scene are opaque, except for the trees. Source data for the specularity and emissivity file name parameters are described in Section 4.2.3.9. The database also allows for two optional parameters, the material's extinction coefficient (for transmissive materials) and texture (both are links to files). Source data for these parameters are also described in Section 4.2.3.9.

### File Creation:

The materials file was created in Microsoft Word™ and saved as a “text only” file. A sample of the file is shown in Figure 4.34. The file contains the parameters for 42 materials, which corresponds to the number of materials used in the scene. The majority of the parameters are used by the therm submodel, and therefore are not required for this study. For completeness, generic values were assigned to those parameters and no effort was made to validate or optimize them. The parameters required by this study include the optical description, specularity, and the emissivity filename. Materials were given specularity values based on estimates of the surface roughness. Emissivity filenames are links to the emissivity database files, and were assigned accordingly.

```

# NOTES: Entries can be arranged in any order. Tags within any entry can be in any
# order. A minimal set of tags are required (see below)
# Required Tags:
# MATERIAL_ENTRY_BEGIN start an entry
# MATERIAL_NAME name of the material
# MATERIAL_ID #ID of the material
# SPECIFIC_HEAT specific heat
# THERMAL_CONDUCTIVITY thermal conductivity
# MASS_DENSITY mass density
# SPECULARITY specularity of the material surface. 0.0 = 100% diffuse and 1.0 = 100% specular
# VISIBLE_EMISSIVITY solar/incident emissivity
# THERMAL_EMISSIVITY thermal/emissivity
# EXPOSED_AREA DCS/THERM surface area term
# OPTICAL_DESCRIPTION OPAQUE, UNIFORM_TRANSMISSION, or NONUNIFORM_TRANSMISSION
# EMISSIVITY_FILE name of emissivity file
# MATERIAL_ENTRY_END end of entry
#
# Optional/Additional Tags:
# EXTINCTION_FILE extinction file -- required for transmission
# TEXTURE_FILE name DIRSIG Texture Image file for material
# USE_GAUSSIAN_TEXTURE flag to generate Gaussian texture (default is FALSE)
#
# New material organization and development for Hawkeye scene

MATERIAL_ENTRY_BEGIN
MATERIAL_NAME = grass
MATERIAL_ID = 1
SPECIFIC_HEAT = 1
THERMAL_CONDUCTIVITY = 12.5
MASS_DENSITY = 1.0
SPECULARITY = 0.0
VISIBLE_EMISSIVITY = 0.79
THERMAL_EMISSIVITY = 0.93
EXPOSED_AREA = -0.25
THICKNESS = 1.275
OPTICAL_DESCRIPTION = OPAQUE
EMISSIVITY_FILE = fall_grass.ems
USE_GAUSSIAN_TEXTURE = FALSE
MATERIAL_ENTRY_END

```

Figure 4.34. Part of the materials file.

A description of the contents of the file is given in the file header.

#### 4.2.3.9 Creation of the Emissivity Files (.ems files)

DIRSIG uses the emissivity parameters of spectral emissivity (as a function of wavenumber), specularity, and specular emissivity to describe the characteristics of a

material. The specularity value is contained in the material database, and combined with the specular emissivity describes the magnitude of the specular lobe. The spectral and specular emissivity values for each material is contained in the emissivity database files.

### Source Data

Source data came from the original DIRSIG emissivity database, the Non-Conventional Exploitation Factors (NEF) database (NEF, 1995), and empirical measurements (pseudo and actual). The original database contained valid visible emissivity data for only a few materials. Previous DIRSIG work had focused on Infrared Imagery and the visible database had not been developed. The NEF database is a government funded effort that catalogs emissivity data. It contains BDRF data on approximately 400 materials. Approximately 100 of the materials were military related and therefore unusable for this scene. The last source of emissivity data was measurements made by the researcher with a spectro-densitometer. Measurements were made of actual objects in the scene, sample materials, and paint chips taken from the local hardware store. These measurements provided the spectral emissivity values. Specular and specularity values were estimated from NEF data for a class of materials.

### File Creation

The emissivity files were created in Excel™ and saved as a “text only tab-delimited” file. A sample emissivity file is shown in Figure 4.35.

1	.
1	22550 0.9358
1	22450 0.9349
0.99896	22350 0.934
0.998968	22250 0.9331

0.997936		22150	0.93198
0.997936		22050	0.93086
0.996904		.	
0.995872		.	
0.99484		.	
.		15850	0.5961
.		11050	0.88561905
.		10950	0.89705714
.		10850	0.90849524
0.50774		10750	0.91993333
0.474716		10650	0.93137143
0.44066		10550	0.94280952
0.405573		10450	0.95424762
0.368421		10350	0.96568571
0.330237		10250	0.97712381
0.291022		10150	0.9885619
0.249742		10050	1
0.20743		9950	1
0.164087		.	
0.118679		.	
0		.	
0		750	1
39850	1	650	1
39750	0.99967365	550	1
39650	0.9993473	450	1
39550	0.99902095	350	1
39450	0.99869459		
39350	0.99836824		
.			

Figure 4.35. A sample emissivity file

The first row gives the number of emissivity curves the file contains. Multiple curves are used for texture and require a texture map to be used. The files used for this scene generally contain one curve. Rows 2-92 (91 rows) contain the fall-off values. The values begin at the facet normal and are decremented at one degree intervals until parallel to the facet (91 increments). These values are common to all the curves that follow. (The specular value assigned to the material is also common to all the curves.) The

remaining rows contain the emissivity curves. Each set of curve values is preceded by a curve identification number (starting with 0). Each curve is described by two numbers, the wavenumber and the spectral emissivity value. The wavenumbers begin at 39850  $\text{cm}^{-1}$  and end at 350  $\text{cm}^{-1}$  (280-28,000 nm). The spectral emissivity values are equivalent to hemispherical emissivity values without the specular lobe.

### Original Database

To generate emissivity files from the original database, the existing files were simply transferred into the emissivity database directory without change.

### NEF database

To generate emissivity files from the NEF database, the DIRS staff created a program that extracts the spectral emissivity values for each material. Generic fall-off values and estimated specular values were then added to the files.

### Empirical Database

To generate emissivity files from empirical measurements, an X-Rite model 938 spectrodensitometer was used. The instrument is shown in Image 4.10.

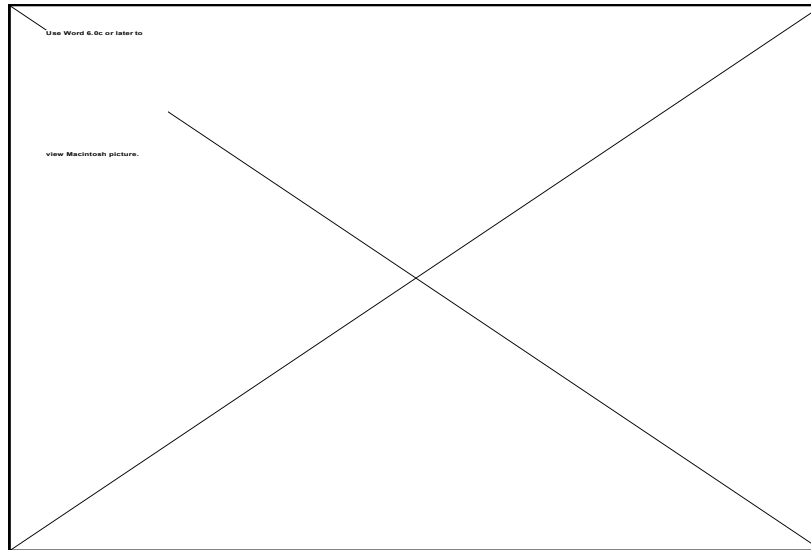


Image 4.10. X-Rite 938 spectro-densitometer.

The instrument illuminates at  $0^\circ$ , measures at  $45^\circ$ , and features a dual-beam, single light pulse compensation method to insure accuracy. Measurements are taken at 20 nm intervals from 400 to 700nm. The bandpass of the measurement is 15 nm and the measurement area is 4 mm in diameter. The instrument then interpolates to provide measurements at 10nm intervals. The result is thirty one values in reflectance units (0-100). Calibration is accomplished through a control target and an internal program. To validate the measurements, multiple independent readings of several samples were made at different times, by different researchers, and with different modes of the instrument. Comparison's were also made to readings of the same sample materials made with an integrating sphere.

#### Field Data:

For field measurements, a ground survey of materials used in the scene was conducted. The experimental setup is shown in Image 4.11.

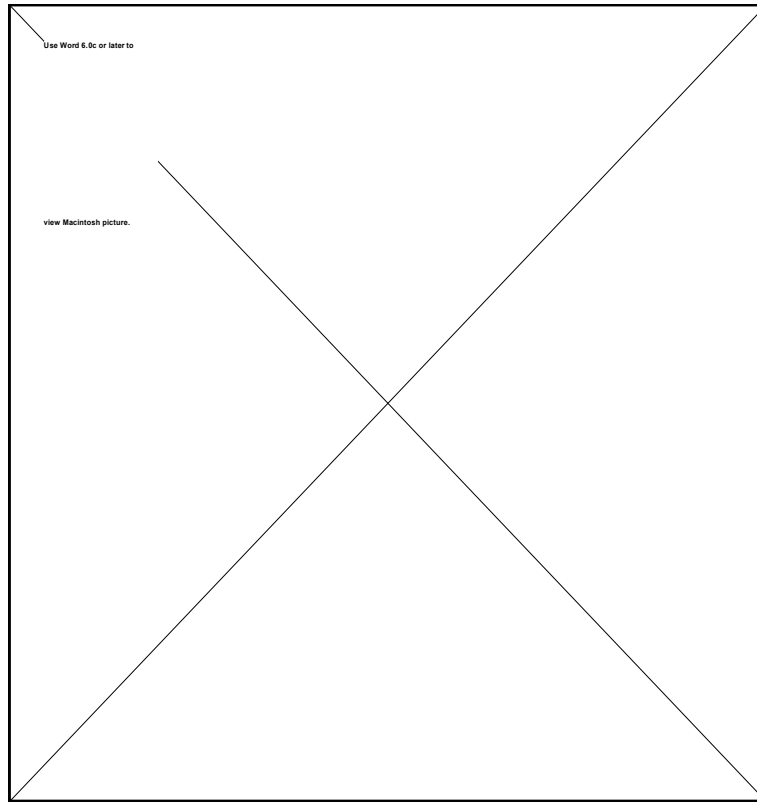


Image 4.11. Experimental Setup

Multiple readings of each material were taken as indicated by the pointers. In addition, digital images of the materials were taken using a Kodak DC-40 for documentation and future studies. A total of five materials were measured.

Sample Data:

For sample measurements, samples of common objects, such as shingles, were obtained for a local hardware store and measured in the laboratory using the spectro-densitometer.

### Pseudo Data:

Because the databases are limited and measuring the reflectivity of some objects is difficult, expensive, and tedious an alternative for generating reflectivity values was developed. The database generated is called the Colors database. It contains emissivity data for approximately 2,600 colors as measure by the X-Rite spectral-densimeter. The colors come from paint samples obtained from Chase-Piktins, a local hardware store. There are samples from four paint lines; Cuprinol (220 samples), Lucite (900 samples), Dutch Boy (Regular) (900 samples), and Dutch Boy Renaissance (640 samples).

To create the database, the measurements from a group of samples, typically 50-100 samples, were entered into an EXCEL worksheet, one column per sample. A listing of the files is provided as an attachment. There are three sheets in each file. The first sheet is named "ref%" and lists the raw data in reflectance units (0-100). The second sheet is named "ems" and contains the emissivity values. The first column in these sheets lists the wavelength of the sample. The second column converts the wavelength to the closest wavenumber ( $\text{cm}^{-1}$ ) required by DIRSIG for the .ems file structure. (See Table 4.4.) The first row lists the sample number. The emissivity values were converted using the formula " $=1 - \text{ref}/100$ ". Samples of these two sheets are shown in Figures 4.36 and 4.37.

Table 4.4. Actual wavenumbers Assigned

wavelength	actual wavenumbers	assigned wavenumbers
400	25000	25050
410	24390.2439	24350
420	23809.52381	23850
430	23255.81395	23250
440	22727.27273	22750
450	22222.22222	22250
460	21739.13043	21750
470	21276.59574	21250
480	20833.33333	20850
490	20408.16327	20450
500	20000	20050
510	19607.84314	19650
520	19230.76923	19250
530	18867.92453	18850
540	18518.51852	18550
550	18181.81818	18150
560	17857.14286	17850
570	17543.85965	17550
580	17241.37931	17250
590	16949.15254	16950
600	16666.66667	16650
610	16393.44262	16350
620	16129.03226	16150
630	15873.01587	15850
640	15625	15650
650	15384.61538	15350
660	15151.51515	15150
670	14925.37313	14950
680	14705.88235	14750
690	14492.75362	14450
700	14285.71429	14250

The reflectivity sheet also has the average blue (400-490 nm), green (500-590 nm), red (600-700nm), and total (400-700nm) reflectivity's of each sample computed below it (rows 34-37). The emissivity sheet also has the average blue (400-490 nm), green (500-590 nm), red (600-700nm), and total (400-700nm) emissivities of each sample computed below it (rows 34-37). In addition, on the emissivity sheet in row 39, is the “visible emissivity”, which is required by the materials database. The visible emissivity was computed by averaging emissivity values over the 280-1000nm band. Because no values

were available over the 280-400nm band, a linear extrapolation was made from measured value at 400nm to 1.00 at 280nm. This was repeated over the 700-1000nm band. The formula used to compute the values was

$$\text{"}=(10.5*(1+C2)+31*C37+15*(1+C32))/82\text{"}$$

where C2 is the value at 400nm, C37 is the average emissivity over the 400-700nm band, and C32 is the value at 700nm. The  $10.5*(1+C2)$  term computes the 21 values over 280-390nm times the average value,  $(1+C2)/2$ , over that range. The  $31*C37$  computes the 31 values over the 400-700nm times the average value, C37, over that range. The  $15*(1+C32)$  term computes the 30 values over 710-1000nm times the average value,  $(1+C32)/2$ , over that range. 82 is the number of values over the range 280-1000nm (a value every 10nm).

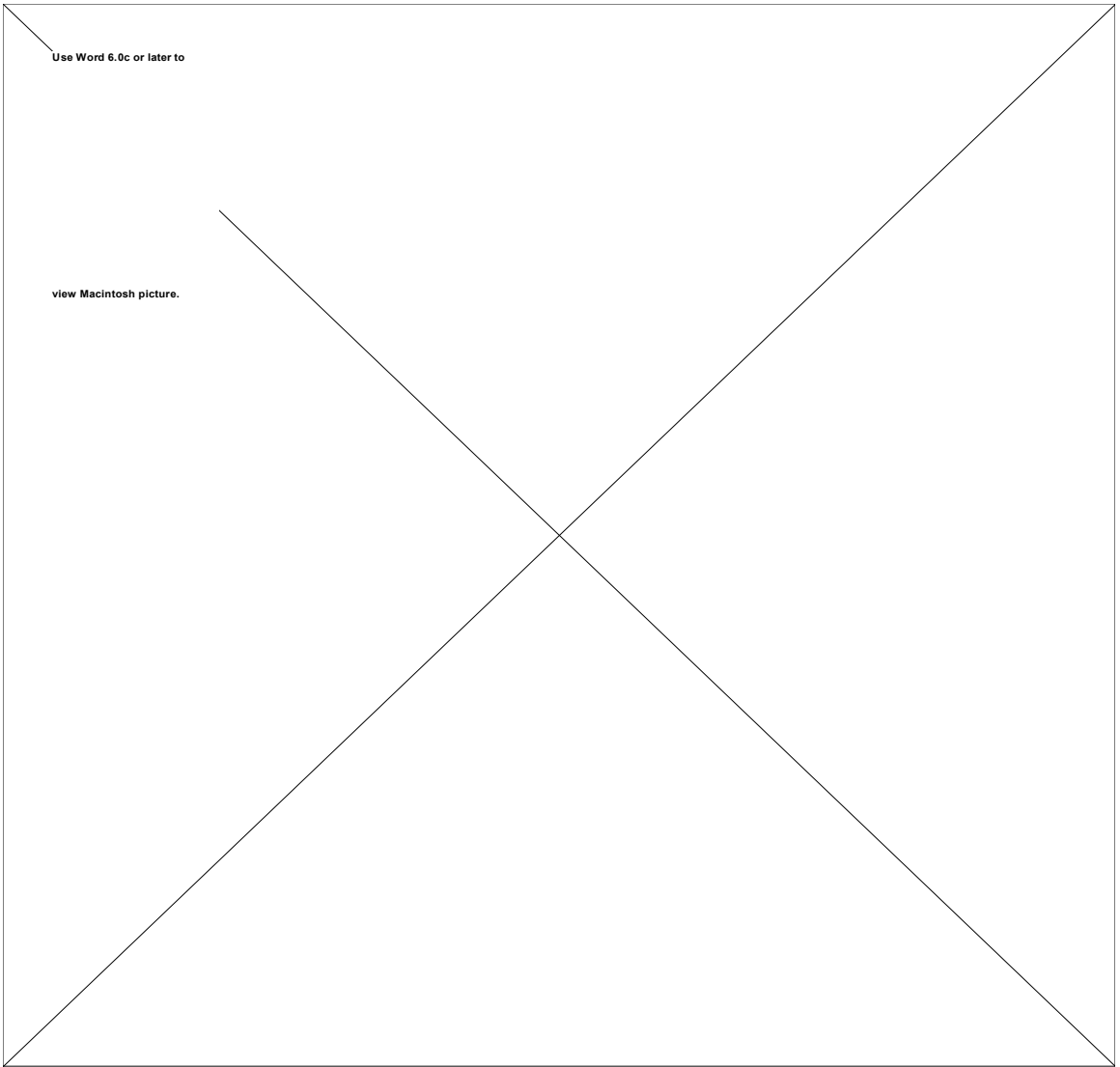


Figure 4.36. ref% sheet from a DB renais file

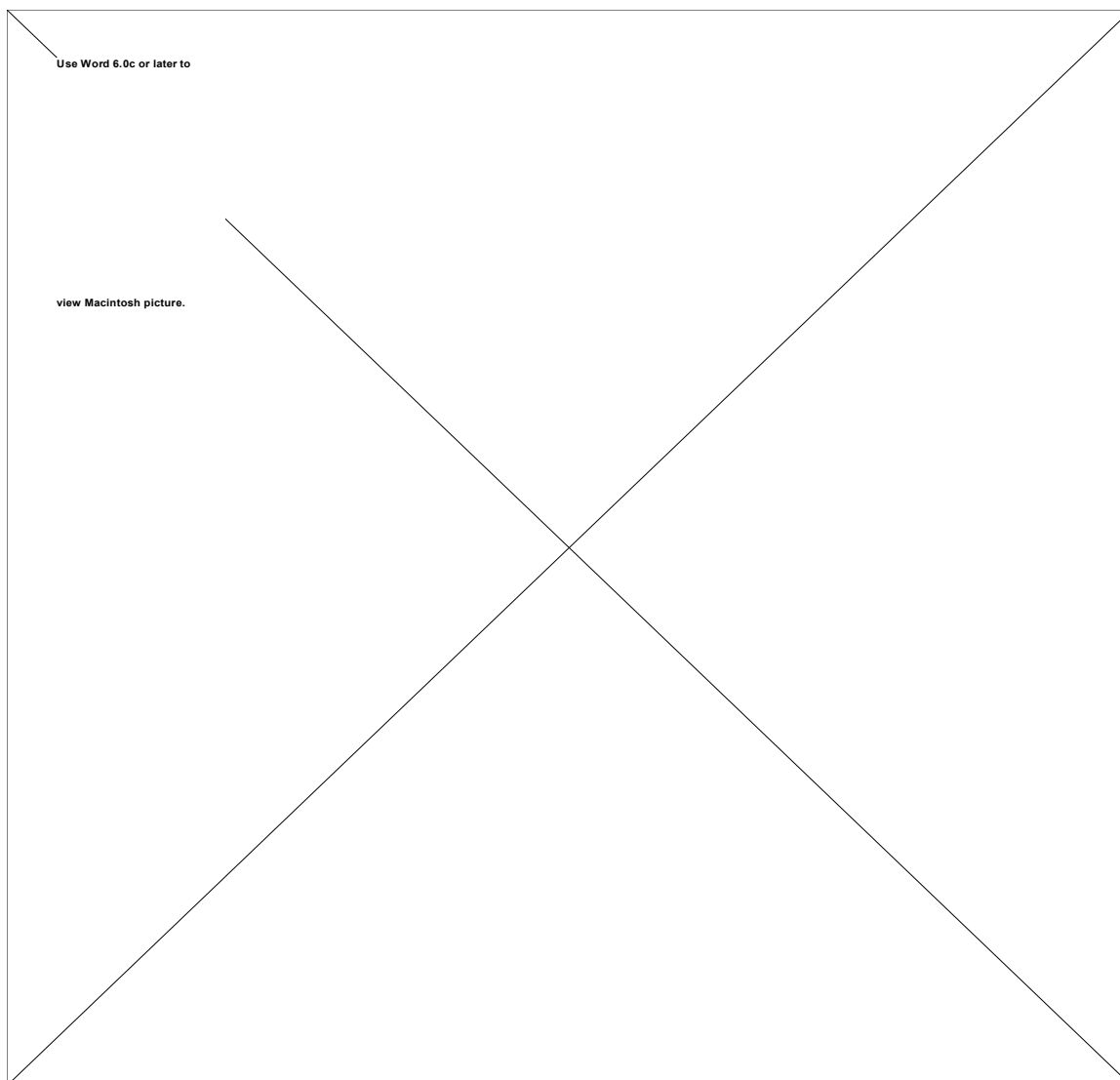


Figure 4.37. “ems” sheet from a DB renais file

The last sheet is called “ems files”. On this sheet the gaps in the wavenumbers were filled in and the specular values were inserted. No data was available for wavenumbers from 39850 to 25050  $\text{cm}^{-1}$  (280-400 nm), so the values were linearly decreased from 1 at 39850  $\text{cm}^{-1}$  to whatever the measured value was at 25050  $\text{cm}^{-1}$ . This was accomplished using the fill/series/trend (linear) EXCEL command. For the gaps in the data between 25050 and 14250  $\text{cm}^{-1}$  (400-700nm) linear interpolation, using the two nearest measured

values, was used. Again, the fill/series/trend command was used. No data was available above 700nm (below  $14250\text{ cm}^{-1}$ ). For the NIR region  $14250\text{-}10050\text{ cm}^{-1}$  (700-1000 nm) a linear ramp was used starting at the last measured value at  $14250\text{ cm}^{-1}$  and increasing to 1 at  $10050\text{ cm}^{-1}$ . Once again, the fill/series/trend command was used. For the values between  $10050$  and  $350\text{ cm}^{-1}$  a value of one was inserted. The first column in this sheet lists the specular values (rows 2-94) and the wavenumbers (rows 95-490). The remaining columns are sample data. The specular values were pulled from a random wood emissivity file. An example of this sheet is shown in Figure 4.38. The first row lists the sample number.

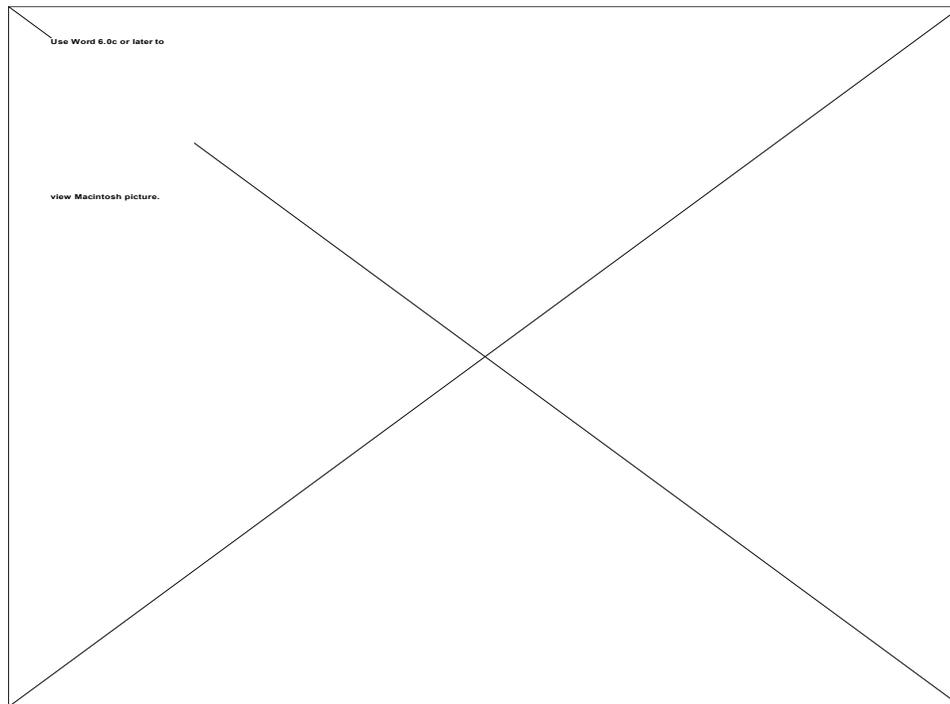


Figure 4.38. "emsfiles" sheet

Sample graphs of the reflectivity curves and the resulting .ems file curves are shown in Figures 4.39 and 4.40.

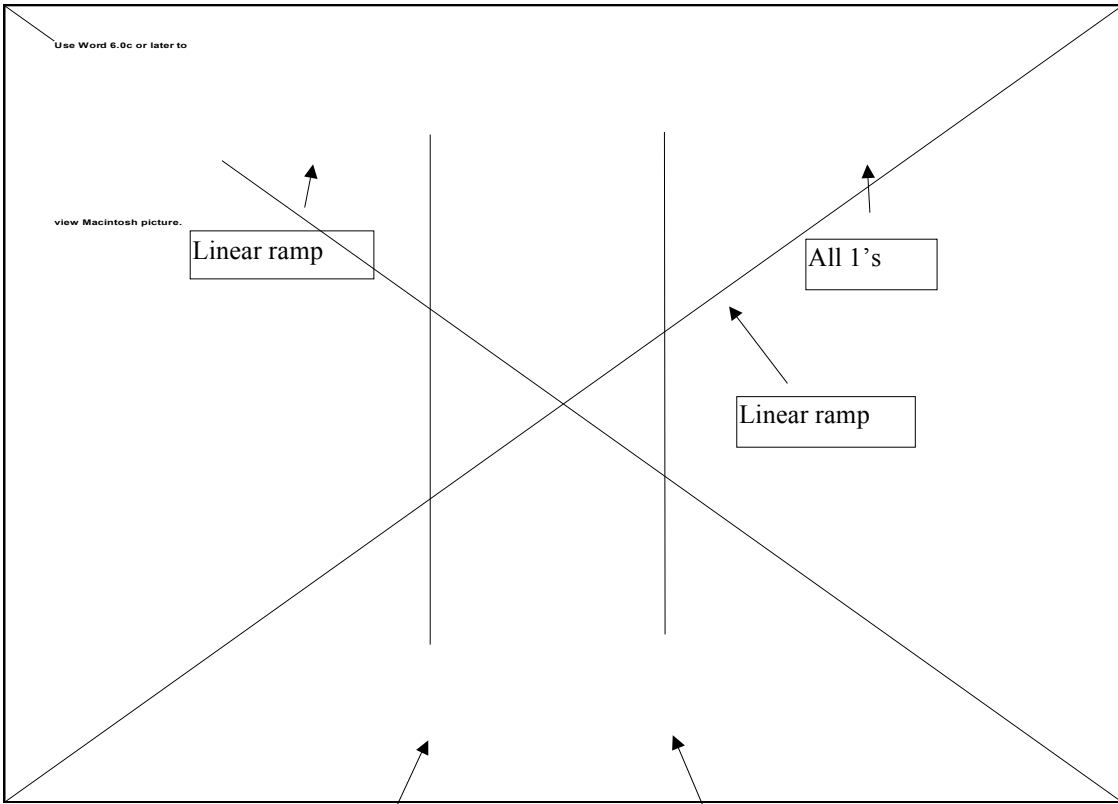


Figure 4.39. Ems file curves for 5 samples (1a, 1b, 2a, 2b, 3a)

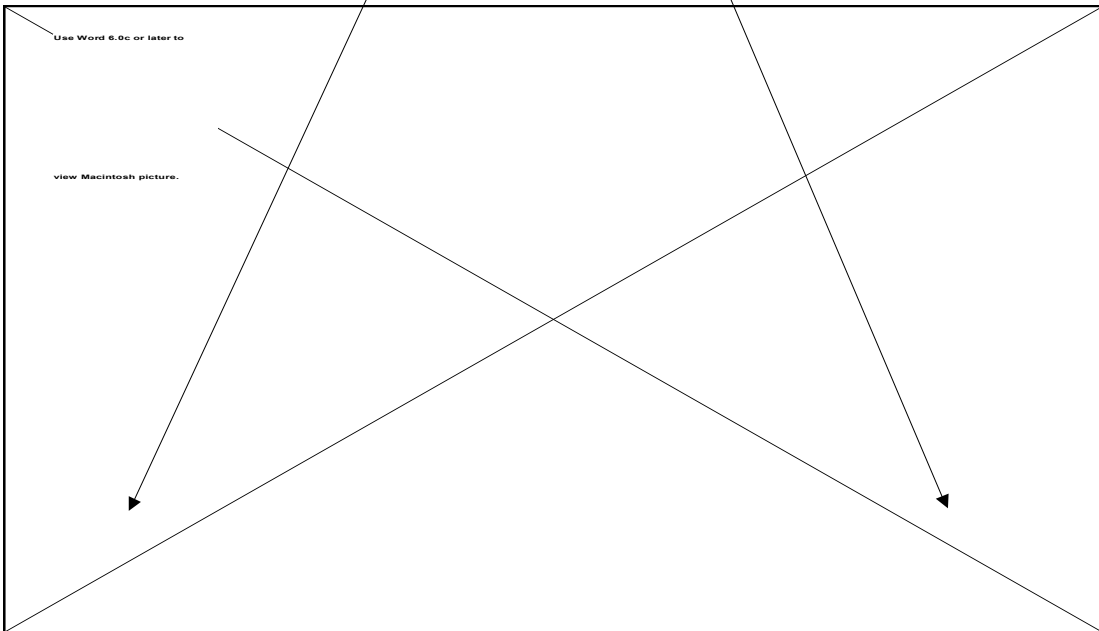


Figure 4.40. Reflectivity curves for the same samples above.

To create a .ems file the first column and the column of the desired color were pasted into a new excel file. The file was then saved as a text “tab-delimited” file with a .ems extension and transferred to the .ems database.

To determine the appropriate “color” to assign to a material, several options were available.

- Choose a color based on a memory or preconception of what the appropriate color should be. The color samples were arranged on a poster board to make this task easier. This method was not used due to its unscientific approach and unreliable results, no sensitivity analysis was accomplished.
- Match the color sample to the object during a ground survey.
- Match the color sample with the reference image visually.
- Average the reflectivity values of the samples (400-500 nm, 500-600 nm, 600-700nm [BGR]) and convert the DC values of the image into reflectivity values, removing the effects of the camera and atmosphere.

When possible, the last approach was used as it removes most sources of error.

When emissivity data was required outside of the band of data available (visible) two approaches were used. The first was the linear ramps described earlier. The second approach was to plot all of the spectral emissivity curves from the NEF database of the class of material desired. For example, all of the brick curves would be plotted. The curve which most closely matched the desired color at 700nm was then selected. The

400-700nm values of the NEF curves were then replaced with the corresponding 400-700nm values of the colors curves.

This was the best solution given the limited amount of data available. It is also reasonable given that at longer wavelengths emissivity is mainly a function of the composition of the material, i.e. most different colored bricks tend to have the same spectral shape at longer wavelengths.

#### **4.2.3.10 Creation of the Sensor Files (.sen files)**

##### Source Data

Source data for the CCD sensor was obtained from the camera manufacturer, Kodak Microelectronic Technology Division.

The response of the DCS camera is shown in Figure 4.41.

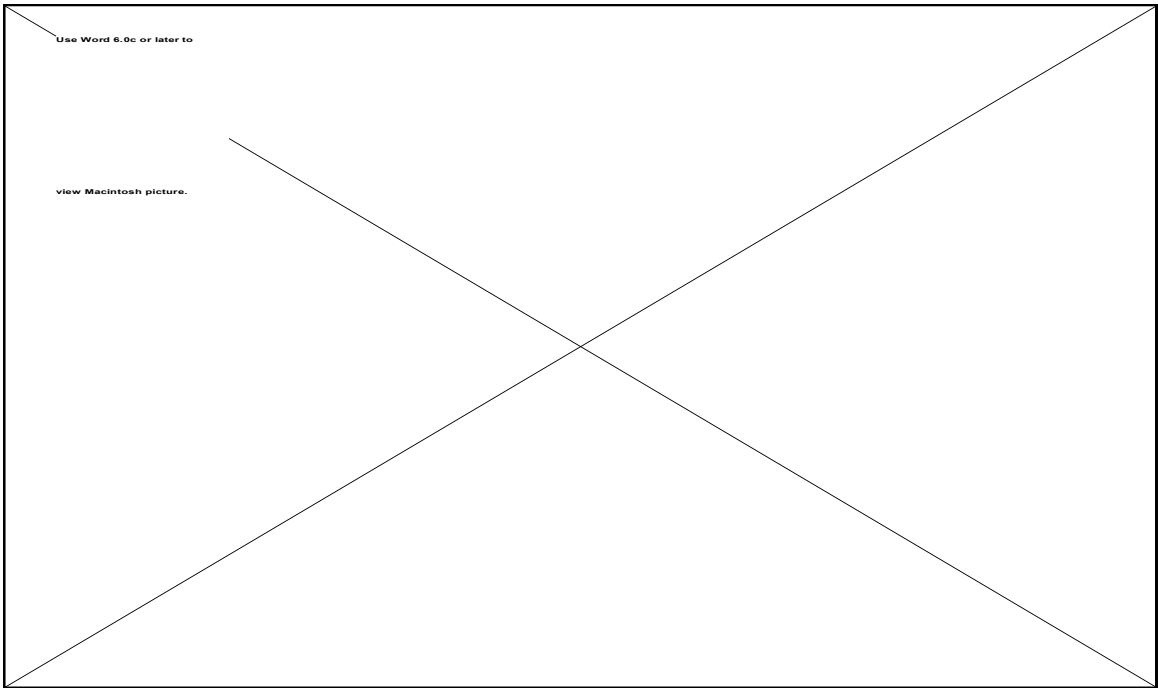


Figure 4.41. Spectral Response of the DCS 420 Camera

### File Creation

The files were created in Microsoft Excel™ and saved as a “text only, tab delimited”. The three files correspond to the bands of the sensor. An example of DCS .sen file is shown in Figure 4.42.

```
7
1
0
0.30
0.50
0.87
0.75
0.63
0.65
0.65
```

Figure 4.42. .sen file

The first row corresponds to the number of bands (resolution) of the corresponding .rad file. The second and third rows are the gain and bias of the sensor. Rows 4-10 are the average response of the sensor over that bandpass as a fraction.

#### **4.2.3.11 Creation of the Extinction coefficient Files (.ext files)**

To account for the transmissive nature of some materials, such as clouds and vegetation, DIRSIG provide .ext files. The files describe transmissiveness as a function of path length. The only transmissive objects in the target scene were tree canopies. Because this study focuses on the reflective nature of materials, the .ext files are documented for completeness only.

#### Source Data

Source data, in the form of .ext files, was obtained from the DIRS staff.

#### File Creation

No new .ext files were created for this scene.

#### 4.2.3.12 Creation of the Batch File (.bat file)

In order to efficiently run DIRSIG, the following batch file, Figure 4.43, was used.

```
#!/bin/csh
#*****
# Set up environment based on machine architecture
#*****
if ($HOSTARCH == aux) then
    setenv TIMER /bin/time
else if ($HOSTARCH == alpha) then
    setenv TIMER /bin/time
else if ($HOSTARCH == mips) then
    setenv TIMER /usr/bin/time
else if ($HOSTARCH == paragon) then
    setenv TIMER /usr/bin/time
else if ($HOSTARCH == sun4) then
    setenv TIMER /bin/time
else if ($HOSTARCH == sgi) then
    setenv TIMER /bin/time
else
    echo " "
    echo "Unsupported architecture for dirsig2.5"
    echo " "
    exit
endif
endif
#*****
# Current run information
#*****
setenv DIRSIG_HOME /dirs/pkg
setenv DIRSIG_EMISSIVITY ../ems_database
setenv DIRSIG_EXTINCTION ../common/extinction
setenv DIRSIG_TEXTURE ../common
setenv DIRSIG_TEXTURE_MIN_WAVELENGTH 0.4
setenv DIRSIG_TEXTURE_MAX_WAVELENGTH 0.7
$TIMER $DIRSIG_HOME/bin/dirsig -tf\
    testscene.adv \
    ../common_databases/testscene.snd \
    ../common_databases/weather_30_Sep_95.wth \
    ../mat_database/hawkeye_russ.mat \
    testscene.gdb \
    ../common_databases/testscene.rad \
    ../common_databases/testscene.sen \
    .....
```

Figure 4.43. .bat file

#### **4.2.4 Running DIRSIG**

Running DIRSIG consisted of simply executing the .bat file. The output of DIRSIG consists of one file for each spectral band. The scene for this study resulted in three files; blue, green, and red. To display the image, the files were combined into a TIFF file using a DIRSIG utility program. To obtain gain and bias values for scaling the scene was run again with the synthetic scene .gdb database replaced with a .gdb database of a scene consisting of two gray cards.

#### **4.3 Adjusting Parameters in the Synthetic Image**

DIRSIG can, using command options, output various debug images to assist in troubleshooting and understanding the scene. Some of the debug images include upwelled radiance, downwelled radiance, and reflectivity. The debug images were used to identify user's errors and correct them.

Once the scene was determined to be correctly created, only the reflectance values were adjusted to reduce the error between the synthetic scene and the reference scene.

#### **4.4 The Reference Imagery Acquisition Process**

##### **4.4.1 Aerial Film Imagery Acquisition Process**

The two aerial film images of the scene were taken prior to this study for Kodak Aerial Systems and were loaned to the researcher for this study. They were taken with a Carl Zeiss RMK A 15/23 Frame Camera. The camera takes 230mm x 230mm images for mapping applications. The camera has a 6" focal length f/4.0 lens and acquires imagery at 2 seconds intervals. The images were acquired at 1115 on 11 Oct 94 from an altitude of 1600 feet. One of the images is nadir and the other is oblique from east to west.

Digital values were obtained for comparison points using a densitometer.

#### **4.4.2 Aerial Digital Imagery Acquisition Process**

Digital imagery of the scene was acquired during a flyover of the target area at 1400L on 30 Sept 95. The platform, a Cessna 172, flew at 1600 feet (altimeter reading) and the images were taken by the researcher with a handheld Kodak Digital Camera System (DCS) - 420. The camera consists of NIKON N90 body with a Kodak Back. The Back replaces the film with a 1524x1012 pixel (14mmx9.3mm) CCD array and support electronics.

The camera was set to the automatic mode during the imaging to reduce motion effects and to ease image acquisition. The images, approximately 100, were taken through the side window of the Cessna. The focal length was adjusted to frame the image and then the autofocus was used. The focal length ranged between 20 and 35 mm. The camera records the camera settings; focal length, shutter speed, etc., for each image.

Raw digital count data (without color management techniques applied) were obtained using an acquisition option available in the camera drivers supplied by Kodak for Adobe Photoshop™.



## **4.5 Scene Validation**

### **4.5.1 Validation Process**

For the validation two perspectives were selected, a nadir film image and an oblique digital image. Within each image, and their corresponding synthetic images, eleven control points were selected for use in the RMS and ROC validation calculations. The control points were selected to provide a representative sampling of materials in the scene. Whenever possible the same control points in the nadir and oblique images were used. Care was also taken to ensure that the control points were pure (one material) for a more accurate comparison.

To obtain digital count values for the film image, the image was digitized at a high resolution on flatbed scanner in the Munsell Lab at RIT. The digitized image was then transferred to the Power Macintosh™ in the Digital Image and Remote Sensing (DIRS) Lab at RIT. Adobe Photoshop™ was then used to acquire control point values and to create histograms. Unfortunately, transfer curves were not available for the film image, making absolute RMS calculations invalid. However, the RMS calculations were made and used for discussions purposes.

To obtain digital count values for the digital image, the images were transferred from the DCS-420 camera to the Power Macintosh in the DIRS Lab. Adobe Photoshop was then used to acquire control point values and to create histograms.

To obtain digital count values for the synthetic images, Adobe Photoshop was also used. in the same manner as described for the digital image.

#### **4.5.2 Validation in the Nadir Perspective**

The eleven control points are labeled in Image 4.12, Nadir Reference Image, and are described in Table 4.5. The corresponding synthetic image is shown in Image 4.13, Nadir Synthetic Image. Digital count values for the control points are listed for the blue, green, red, and combined (R, G, R, C) bands for both the synthetic and reference images. The control points are ranked in order from lowest digital count to highest. At the bottom of each table the ROC and RMS values are computed. Following the table are the histograms of the reference image and the synthetic image, Figures 4.44 through 4.51.

To achieve the ROC correlation shown in Table 4.5 only two parameters from the initial run required adjustment. The diffuse reflectivity of the “new” asphalt was reduced by 30% and the diffuse reflectivity of the tan shingles was reduced by 10%. These adjustments were considered within the typical range of acceptable values.

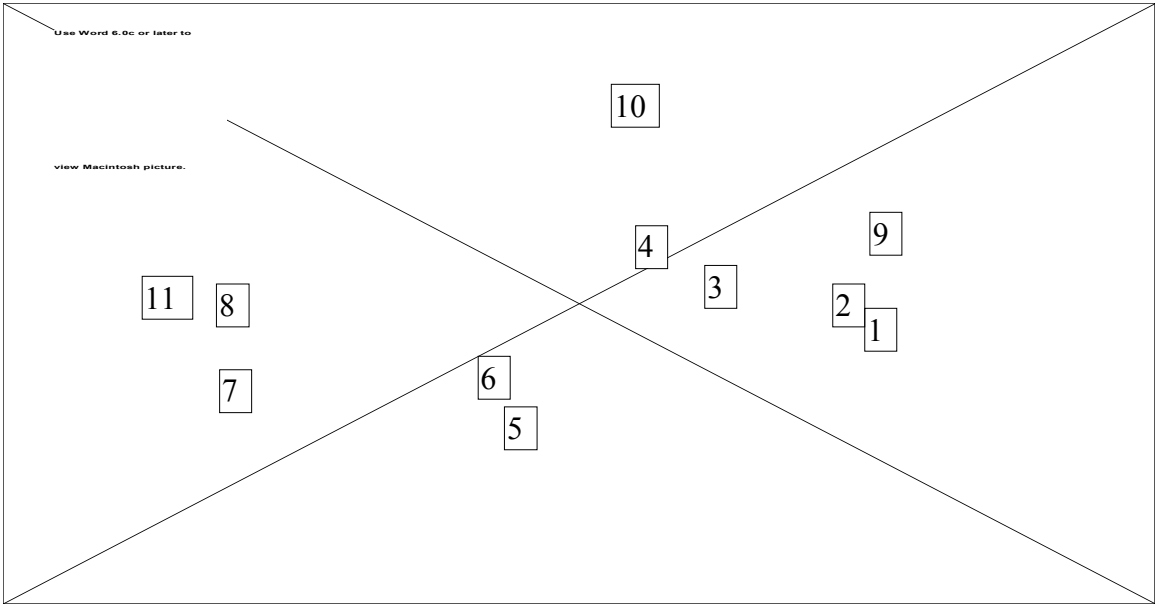


Image 4.12. Nadir Reference Image.

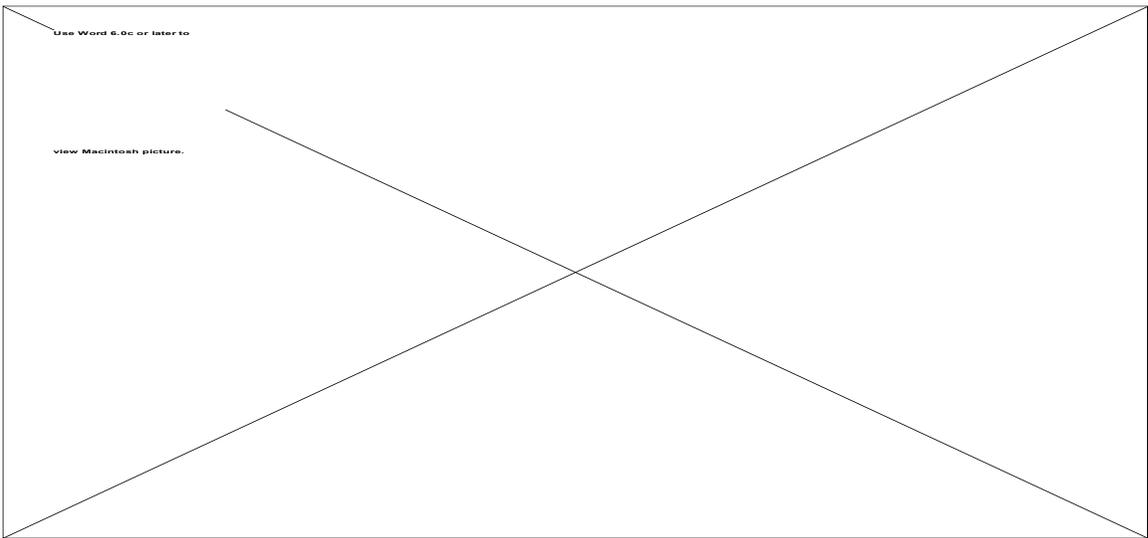


Image 4.13. Nadir Synthetic Image.



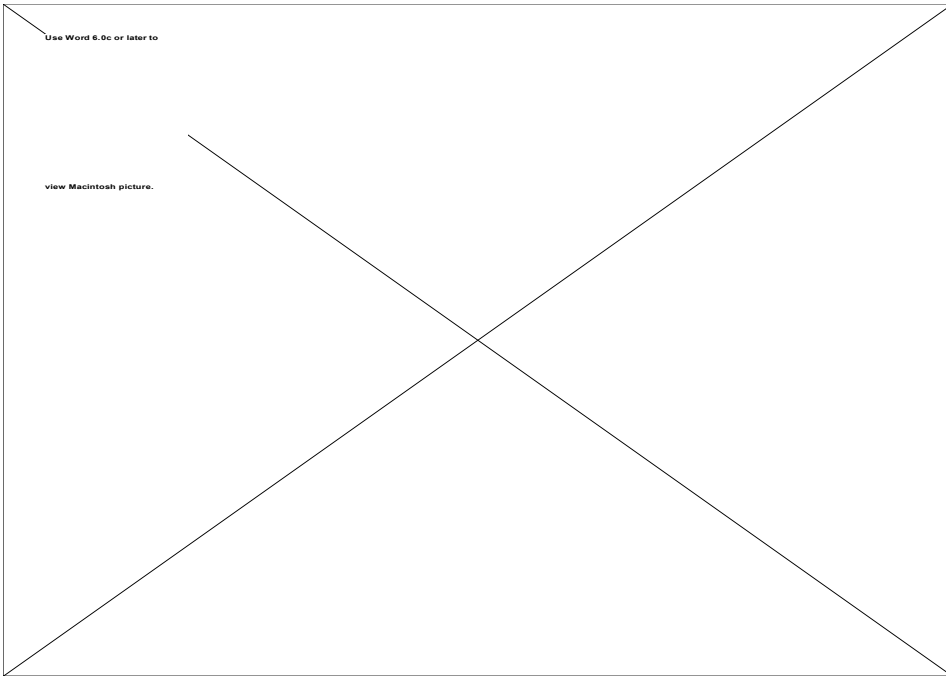


Figure 4.44. Histogram of the Reference Image, Red Band.

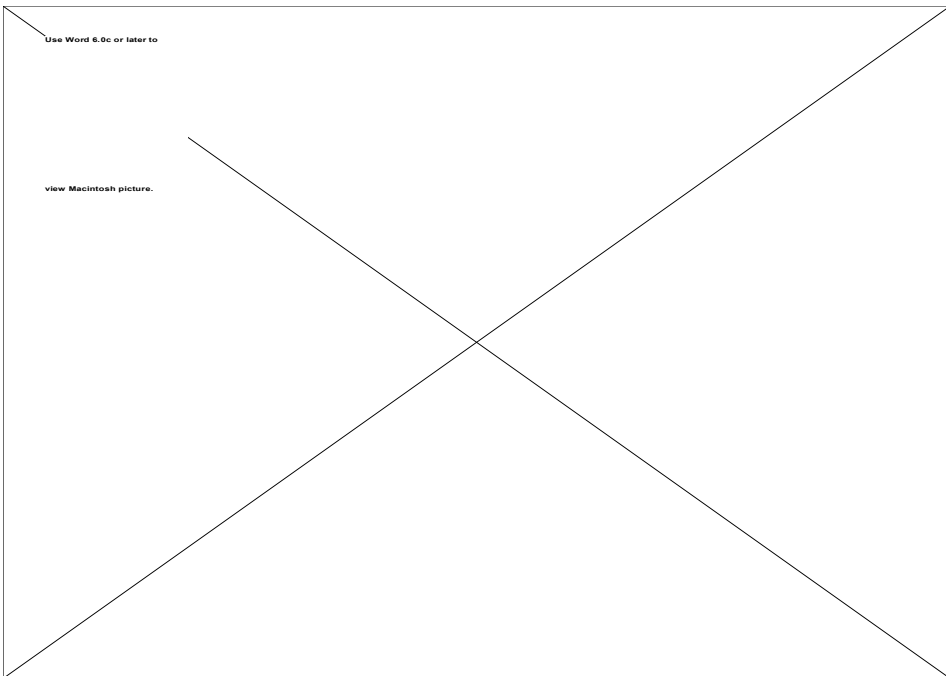


Figure 4.45. Histogram of the Reference Image, Green Band.

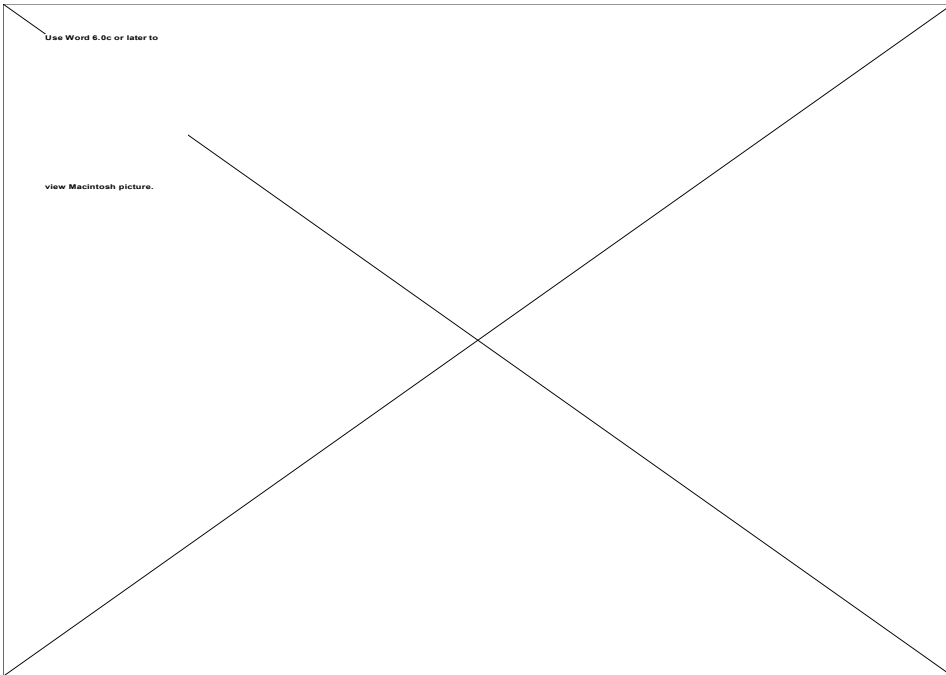


Figure 4.46. Histogram of the Reference Image, Blue Band.

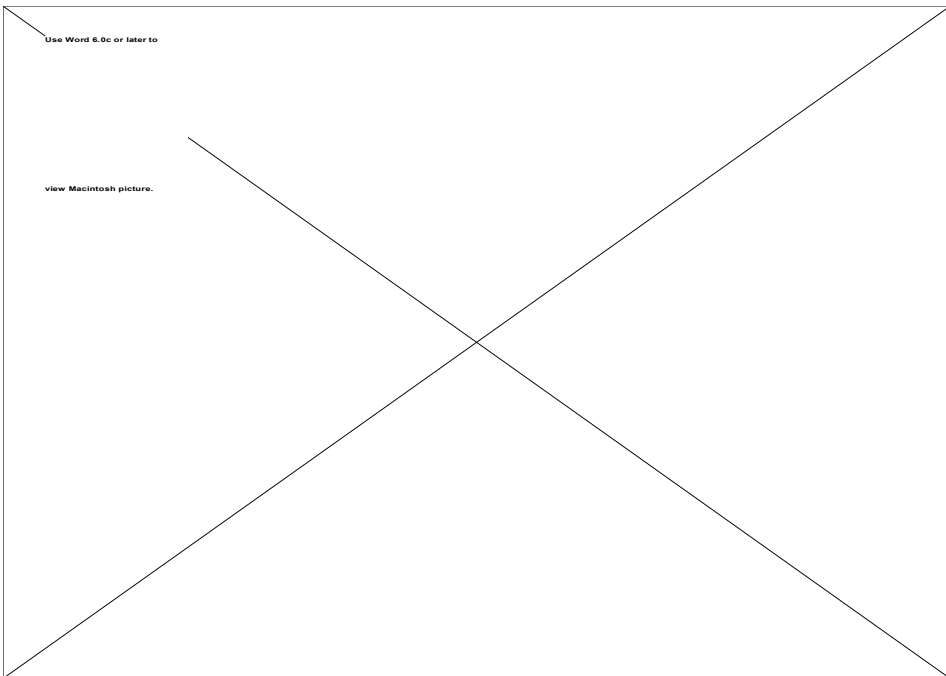


Figure 4.47. Histogram of the Reference Image, Combined Bands.

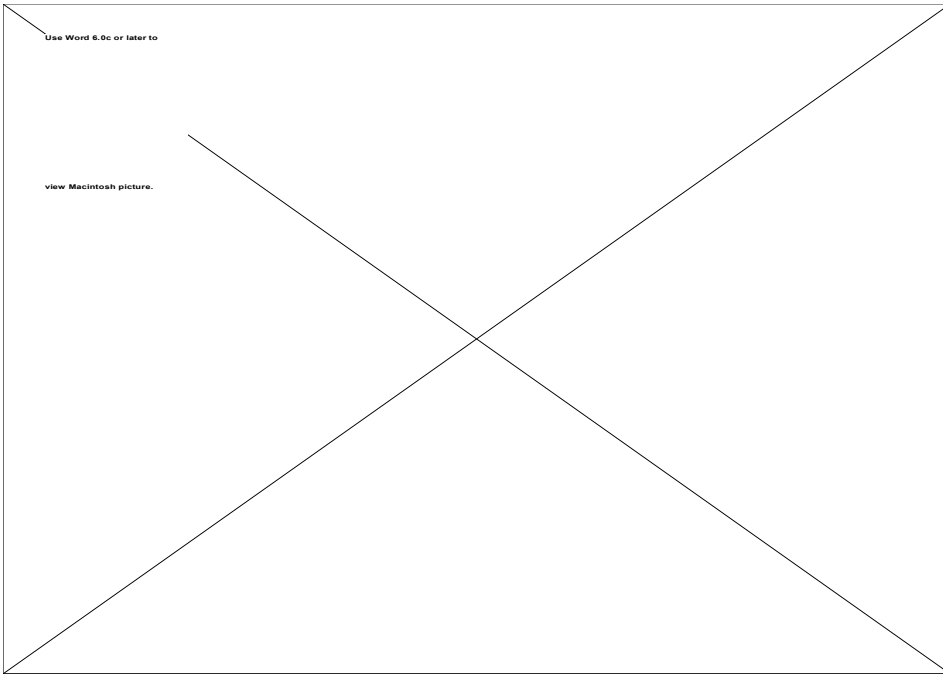


Figure 4.48. Histogram of the Synthetic Image, Red Band.

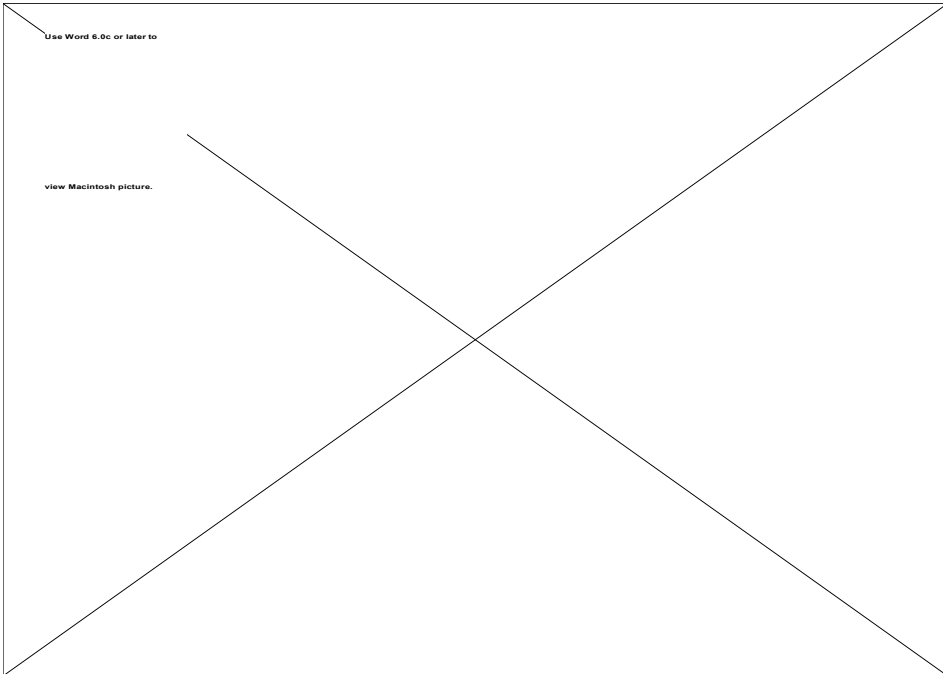


Figure 4.49. Histogram of the Synthetic Image, Green Band.

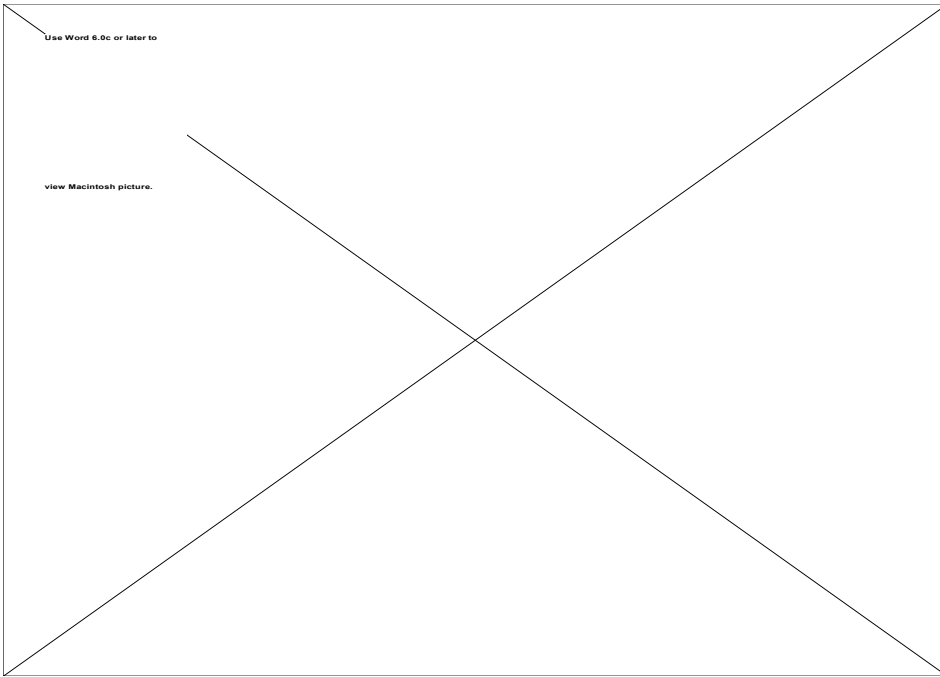


Figure 4.50. Histogram of the Synthetic Image, Blue Band.

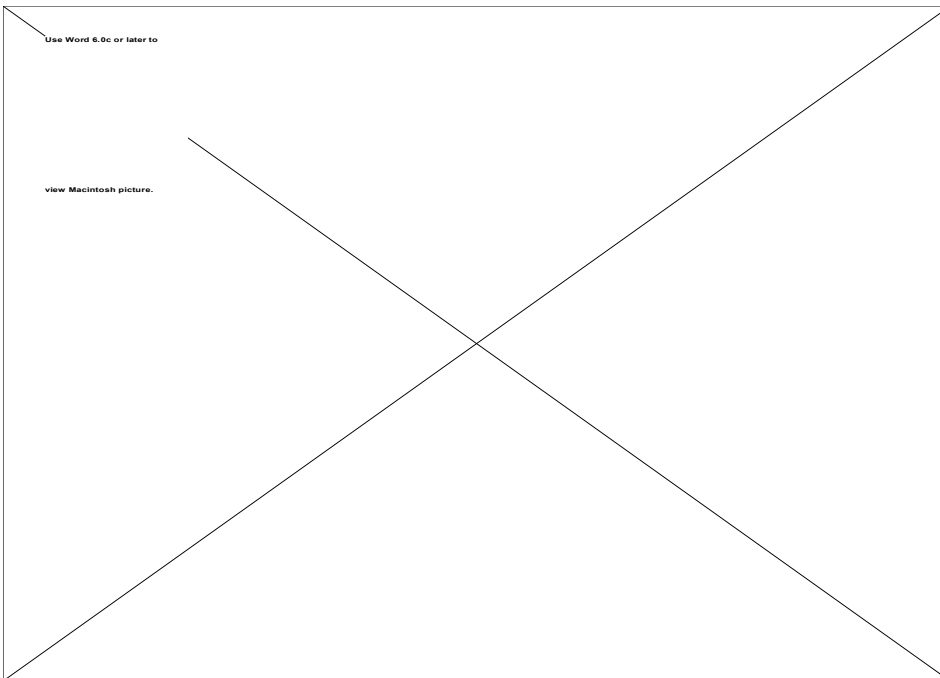


Figure 4.51. Histogram of the Reference Image, Combined Bands.

The ROC results show a high correlation between the reference image and the synthetic image indicating that the DIRSIG model is valid. The correlation in the red, green, and combined bands is 92 to 97%. The blue band showed a lower correlation, 78%. The reason for this is not clear from the results, there is no clear pattern or indicator. The RMS error for the three bands were 58, 64, and 82 respectively, indicating a bias in the images. The cause of the larger relative bias in the blue band is unknown but is consistent the lower ROC value in the blue band. The histograms of the film images show the characteristic weighting towards the lower digital count values. This is because the scanner is a linear-to-luminance device. The histograms of the synthetic images are more normally distributed. Each of the histograms has more distinct groupings around certain digital counts values. This is the result of three factors; the number of materials in the scene, lack of texture, and lack of mixed pixels. The addition of more materials would add “spikes” to the distribution. The reference images contains hundreds of distinct materials where the synthetic images has less than 50. The addition of texture would broaden the distribution around the “spikes” and lower their magnitude. The addition of mixed pixels would reduce the magnitude of the “spikes” and “fill-in” between the “spikes”. Overall, it was clear that DIRSIG can duplicate a reference image and is therefore valid.

### **4.5.3 Validation in the Oblique Perspective**

The eleven control points are labeled in Image 4.14, Oblique Reference Image, and are described in Table 4.6. The corresponding synthetic image is shown in Image 4.15. Table 4.6 also shows the results of the RMS and ROC calculations. Histograms of the images are shown in Figures 4.52 through 4.59. The only change to DIRSIG between the nadir and oblique images was a change in perspective. There were NO changes in reflectivity curves.

To achieve the ROC results shown in Table 4.6 any representative pixel of the material within the image was considered selectable for the validation.

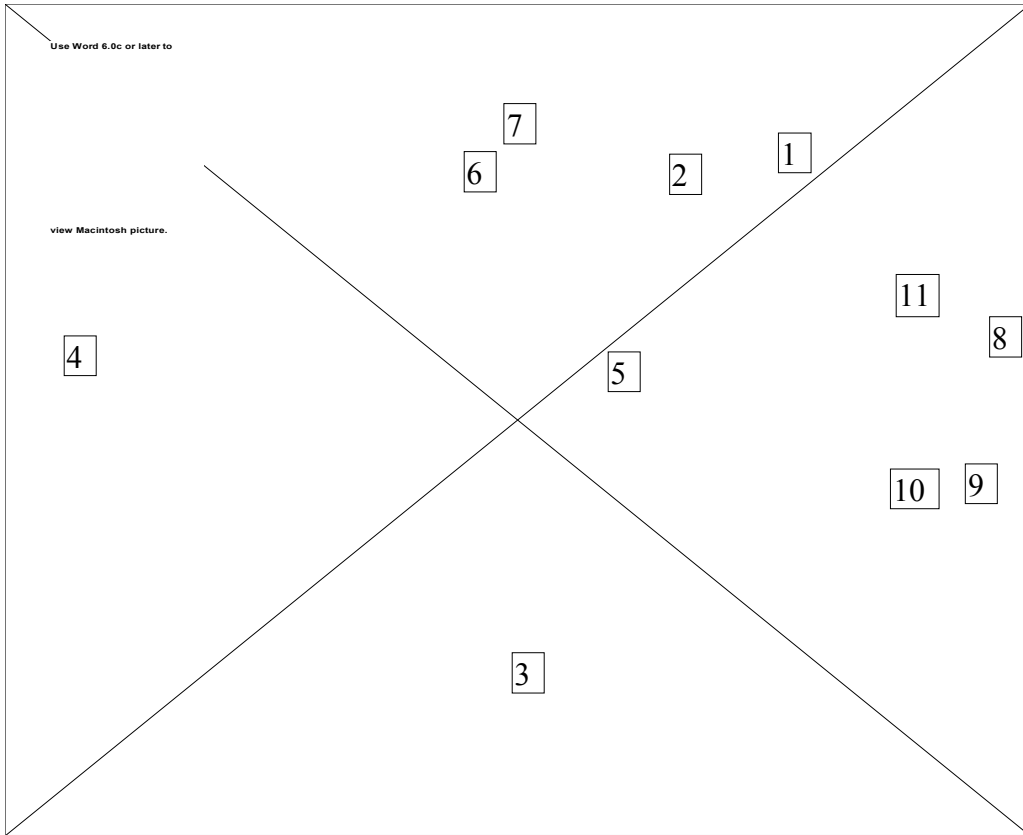


Image 4.14. Oblique Reference Image

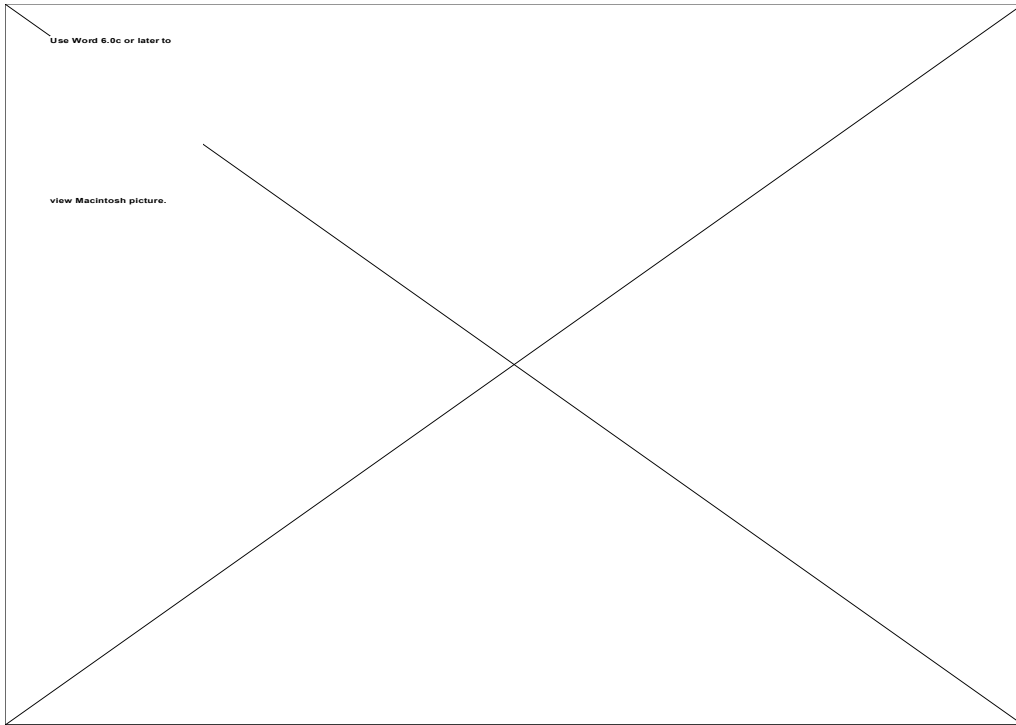


Image 4.15. Oblique Synthetic Image



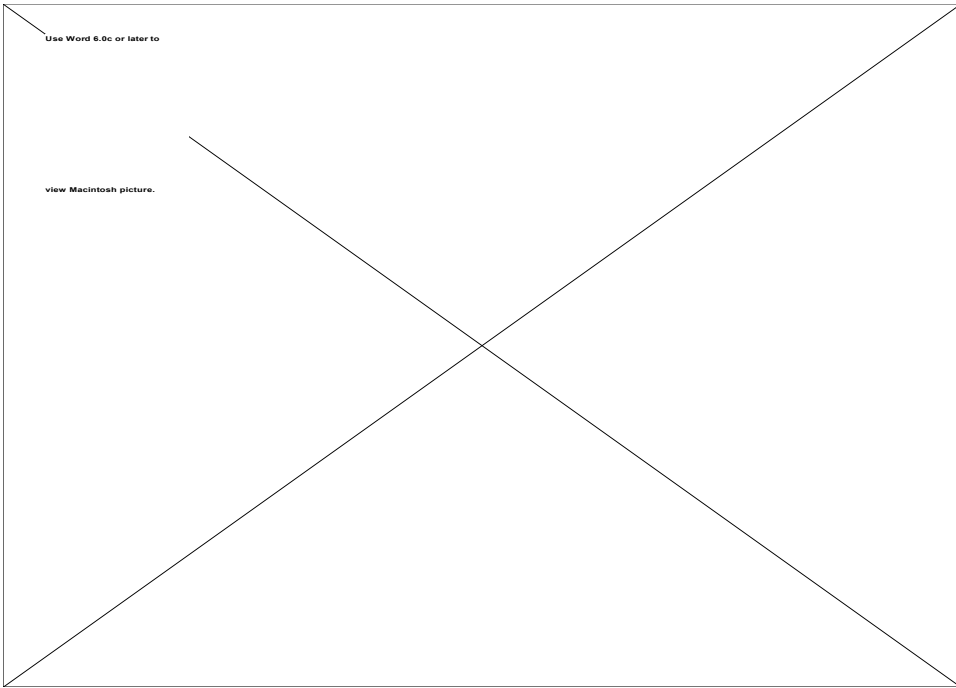


Figure 4.52. Histogram of the Reference Image, Red Band.

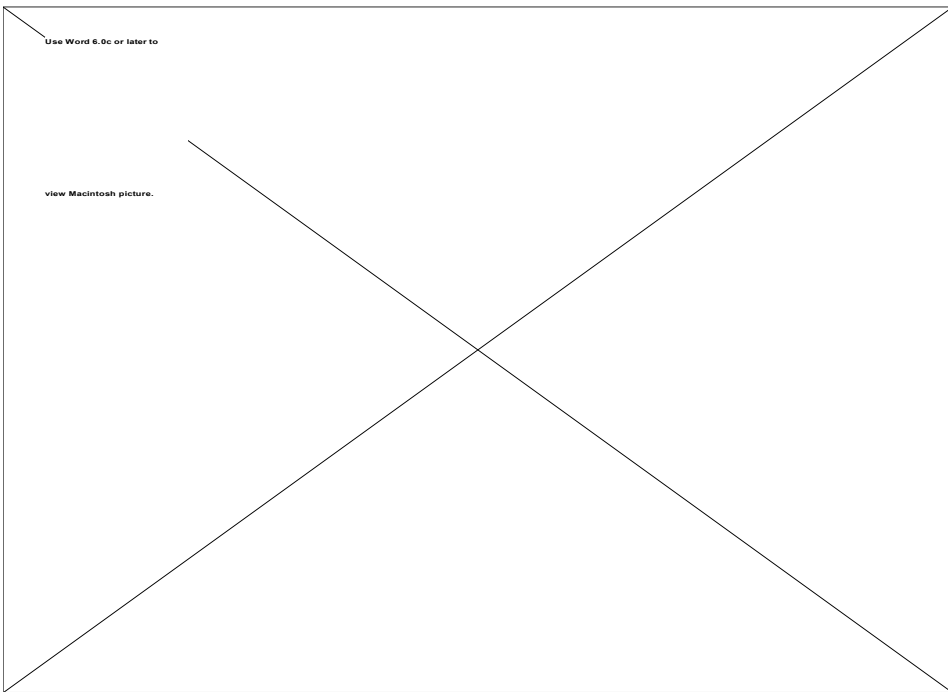


Figure 4.53. Histogram of the Reference Image, Green Band.

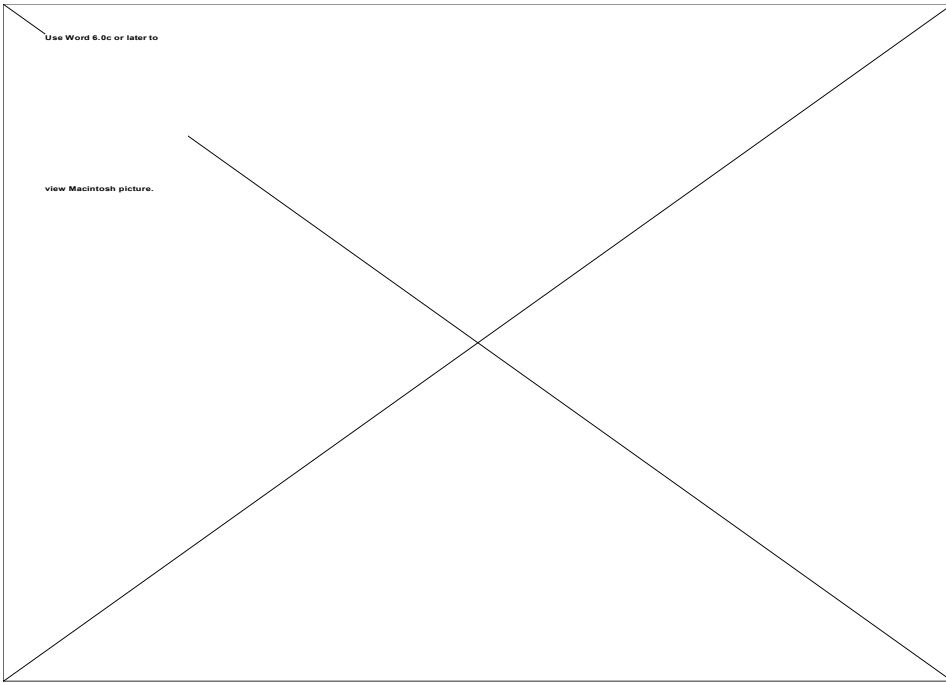


Figure 4.54. Histogram of the Reference Image, Blue Band.

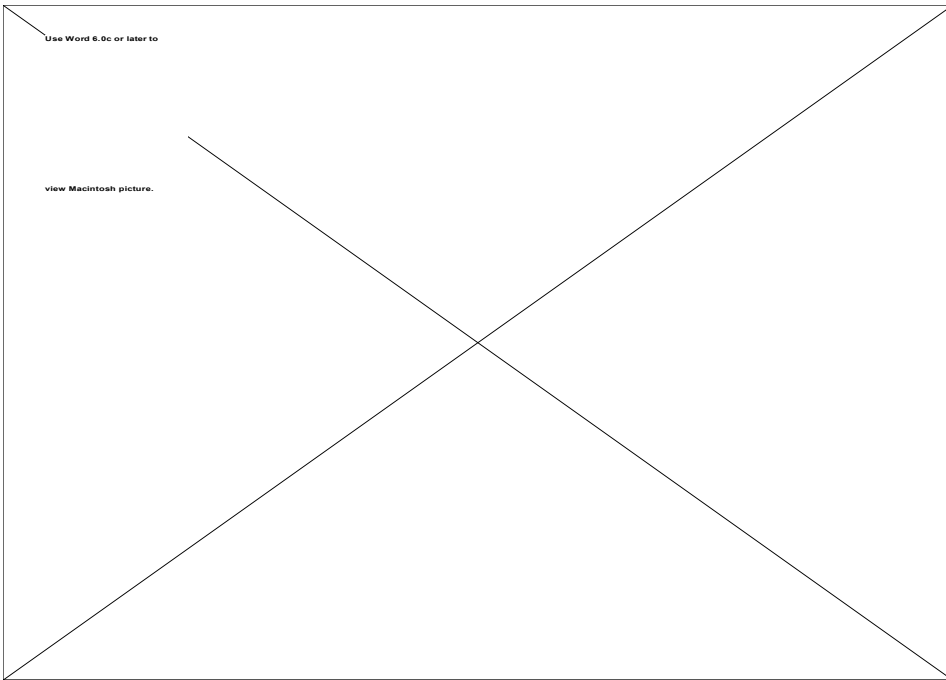


Figure 4.55. Histogram of the Reference Image, Combined Bands.

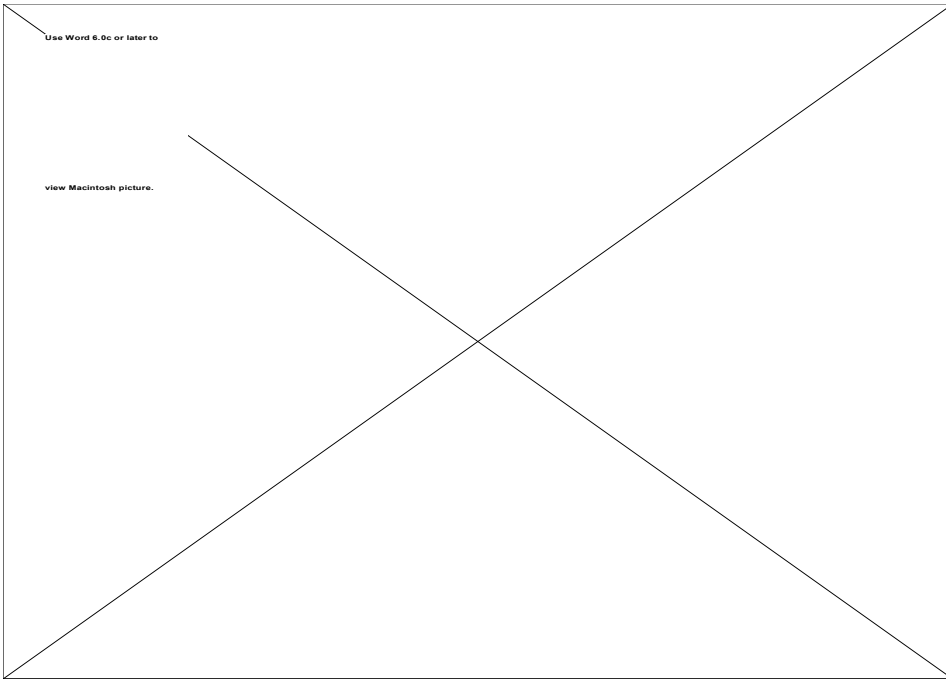


Figure 4.56. Histogram of the Synthetic Image, Red Band.

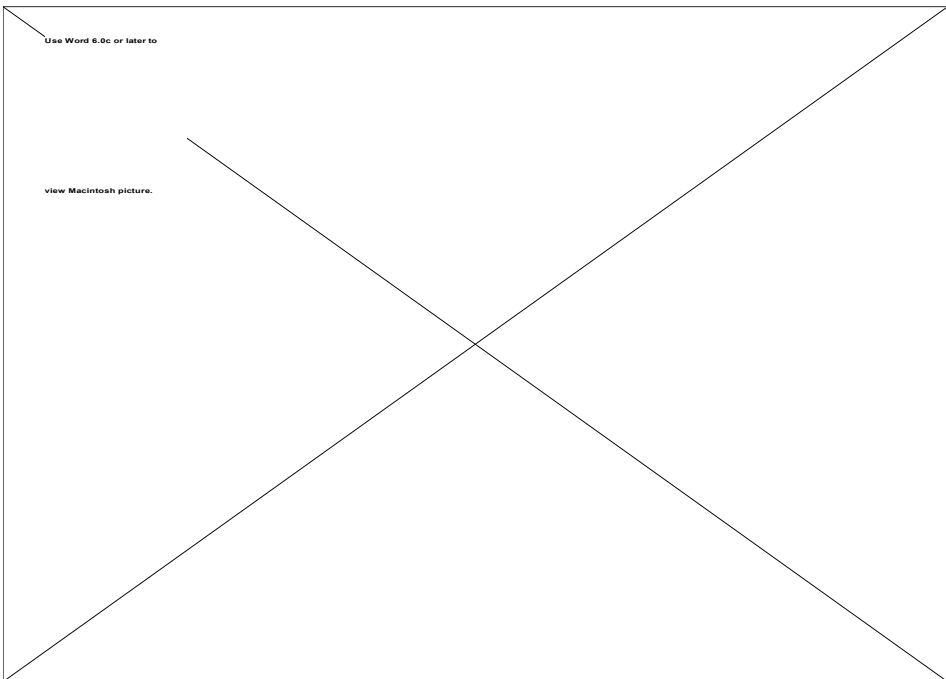


Figure 4.57. Histogram of the Synthetic Image, Green Band.

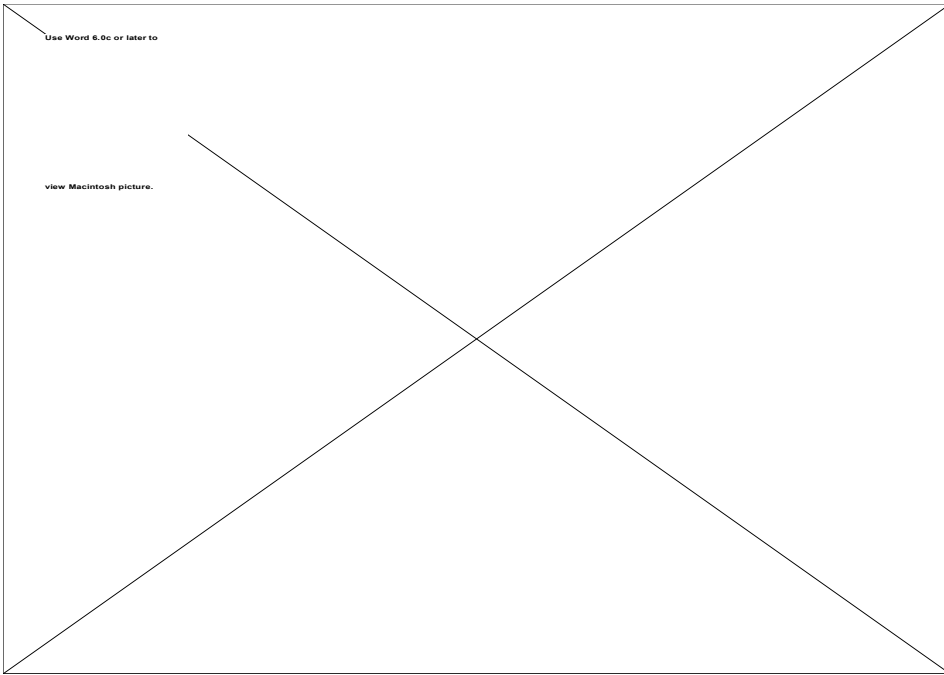


Figure 4.58. Histogram of the Synthetic Image, Blue Band.

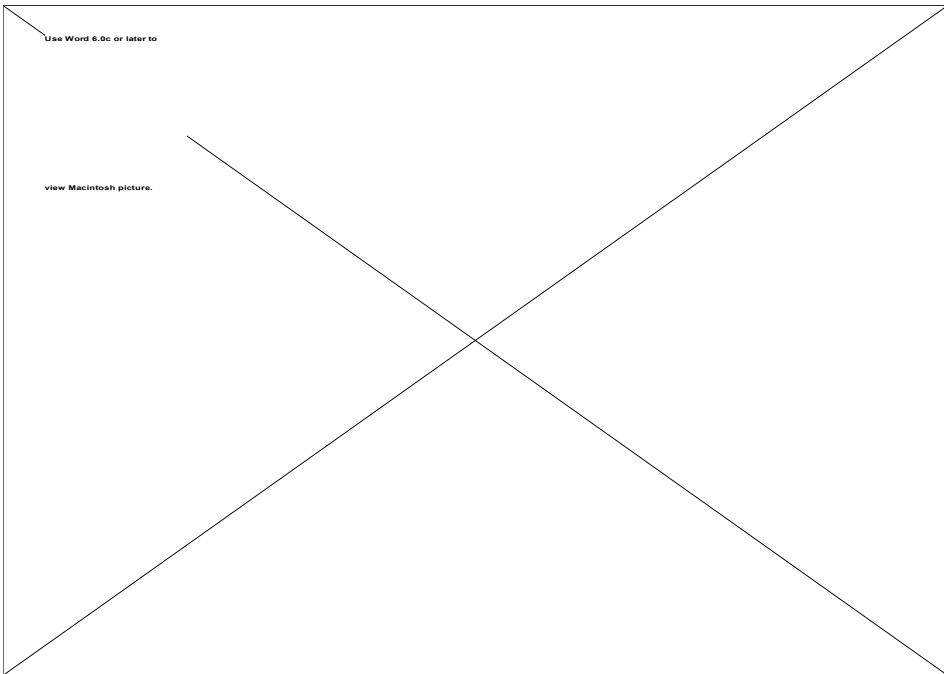


Figure 4.59. Histogram of the Reference Image, Combined Bands.

The ROC results show very high correlation between the synthetic and reference images. The correlation is between 0.93 and 1.00 for all the bands, indicating that DIRSIG is valid. The RMS errors for the control points are approximately 30 digital counts for each band indicating a bias. However, the mean and standard deviation derived from the histograms of the overall images do not support this bias for the blue band. They are shown in Table 4.7. In the blue band, the RMS is only 7 digital counts. The reason for this is unknown.

Table 4.7. Image Statistics

	Red		Green		Blue		Comb.	
	Ref	Syn	Ref	Syn	Ref	Syn	Ref	Syn
Mean	87	106	87	109	92	99	87	107
Std Dev	33	41	31	40	27	35	31	39
Median	80	90	80	90	85	83	80	92

From overall results, it is clear that the synthetic image was able to capture the general statistics of the reference image. The RMS error may indicate a variation of the possible values within a class of materials or number of materials. The synthetic image histograms also show the “spikes” described earlier for the nadir images. Based on the results, DIRSIG is valid and can be used to model a change in perspective.

## **5.0 DIRSIG Reflectance Analysis and a Proposed Model**

This section documents the analysis of the impact of reflectance on the radiance reaching the sensor. It also describes proposed changes to how DIRSIG models reflectance to improve radiometric accuracy.

### **5.1 Sensitivity Analysis**

The value of a reflectance model is, in part, proportional to the impact reflectance has on radiance reaching the sensor. If a large error in reflectance causes only a very small error in radiance calculations, the value of the reflectance model is limited. Of course, the impact will also be a function of the imaging conditions. To measure the value, a simple “sensitivity analysis” is performed in Section 5.1.1. This is followed by a formal sensitivity analysis of DIRSIG’s (Beers, 1957) implementation in Section 5.1.2. All variables in the analysis are assumed to be independent. This assumption holds reasonably well except for the atmospheric transmittance values between the sun/target ( $\tau_1$ ) and the target/sensor ( $\tau_2$ ) and between the upwelled radiance ( $L_{us}$ ) and the target/sensor atmospheric transmittance ( $\tau_2$ ). The atmospheric transmittance values tend to be positively correlated as the altitude of the sensor increases and its orientation relative the target becomes similar to the sun/target orientation. The upwelled radiance and the target/sensor atmospheric transmittance are inversely correlated.

#### **5.1.1 Simple Sensitivity Analysis of the Big Equation (Visible Spectrum)**

The parameters that must be considered when computing the radiance exiting a material include solar radiance, downwelled radiance, diffuse reflectivity, specular reflectivity, and shape factor. To make comparisons of the relative importance of these parameters, a base case is presented and the radiance exiting the material is computed. Individual

parameters are then modified, the radiance exiting the material is computed, and the results are compared to the base case. This simple analysis will provide a general perspective on the relative importance of the parameters and will create a context for the formal analysis.

### BASE CASE

The setup for the Base Case is shown in Figure 5.1.

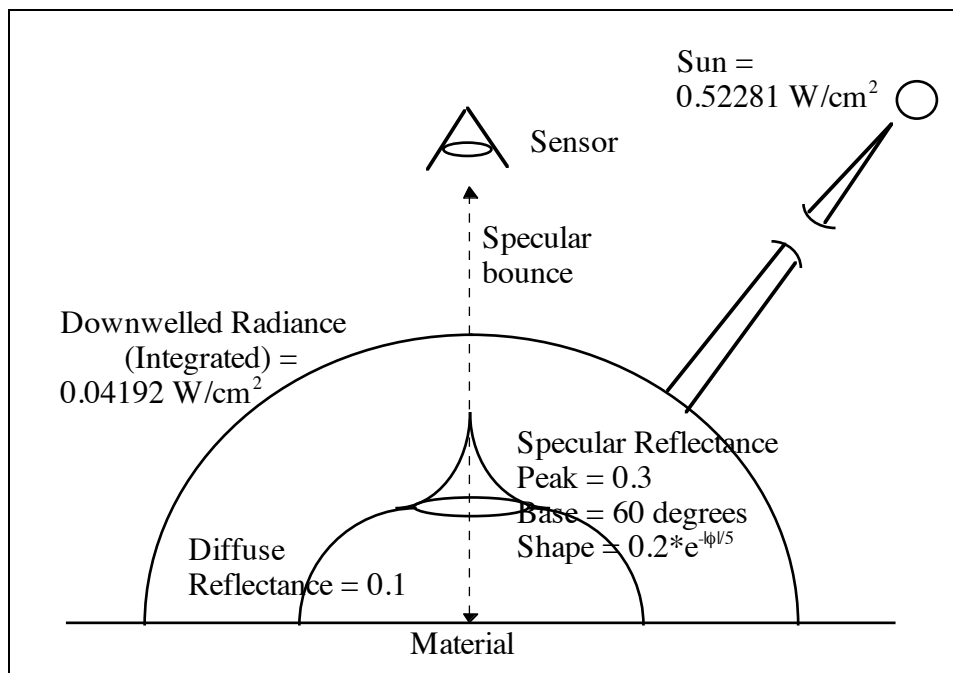


Figure 5.1. Base Case Radiance and Reflectance Maps.

In the base case, the material is viewed from a nadir perspective and illuminated by the sun from a zenith angle of 45 degrees, imaging conditions common in remote sensing. The diffuse reflectivity of the material is 0.1 [unitless]. The specular lobe has a base of 60 degrees (1/8 of the hemisphere - See Appendix B for the calculation.), a peak amplitude of 0.3, and a shape characterized by the function

$$r_{\text{specular lobe}} = 0.1 + 0.2 * e^{\frac{-|\text{angle from specular bounce angle}|}{5}} \quad [\text{unitless}]$$

The shape of the reflectance map was modeled to reflect curves observed in the NEF database. The material has a shape factor of 1, no obscuration. The solar radiance has a magnitude of 0.52281 W/cm<sup>2</sup> and occupies an insignificant solid angle. The integrated downwelled radiance has a magnitude of 0.04192 W/cm<sup>2</sup> and is assumed to be evenly distributed over the hemisphere. This assumption was designed to make calculations tractable. The radiance magnitude values were generated by the build\_radiance program and cover the 0.4 to 1.0 μm spectral band.

The radiance exiting the facet for the Base Case is given by

$$\begin{aligned} \text{Radiance (L)} = & \text{diffuse\_reflectance} * \text{solar\_radiance} + \\ & \text{specular\_lobe\_percent} * \text{average\_specular\_reflectance} * \text{downwelled\_radiance} + \\ & \text{remaining\_percent} * \text{diffuse\_reflectance} * \text{downwelled\_radiance} \end{aligned}$$

$$L = 0.1 * 0.52281 + 1/8 * 0.16335 * 0.04192 + 7/8 * 0.1 * 0.04192$$

$$L = 0.052281 + 0.00086 + 0.00367 = 0.052281 + 0.00453 = 0.05680 \text{ [W/cm}^2\text{]}$$

From the Base Case it is clear that the solar radiance term dominates the calculation. It is an order of magnitude larger than the downwelled radiance term. This indicates that it must be included in any SIG model.

#### CASE 1: Estimate Errors

In Case 1, the setup is the same as the Base Case except that the effect of a ten percent error in each of the parameters is calculated. The results are shown in Table 5.1.

Table 5.1. Estimate Error Calculation Results

<b>Parameter</b>	<b>Value</b>	<b>L [W/cm<sup>2</sup>]</b>	<b>Percent Error [%]</b>
BASE CASE		0.05680	0.0
Diffuse reflectance	0.11	0.06420	9.9
Solar radiance	0.57509	0.06203	9.2
Specular Lobe Percent	0.1375/0.8625	0.05684	0.1
Average Specular Reflectance	0.17969	0.05689	0.2
Downwelled Radiance	0.04611	0.05726	0.8

The calculations show that for each percent error in diffuse reflectance or solar radiance a percent error in the final radiance calculation results. The calculations also show that the final radiance calculations are not affected very much by errors in the Specular Lobe Percent, the Average Specular Reflectance, or the Downwelled Radiance.

#### CASE 2: Specular Reflectance

In Case 2a and 2b, the effect of not modeling the specular nature of the material is determined. The setup for Case 2a is the same as the Base Case except that the reflectivity has no specular component. It is shown in Figure 5.2. In Case 2b, the reflectivity has a specular term and the sun has been put in the specular bounce direction. The setup is shown in Figure 5.3. The results are shown in Table 5.2.

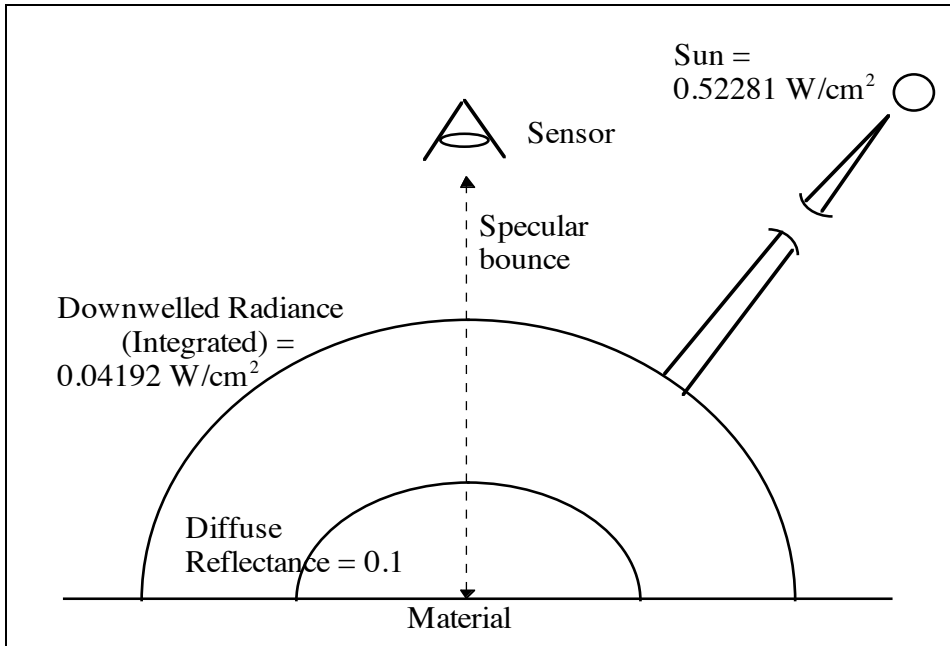


Figure 5.2. Case 2a Radiance and Reflectance Maps: No specular reflectance, initial setup.

In Case 2a, there is no specular reflectance component.

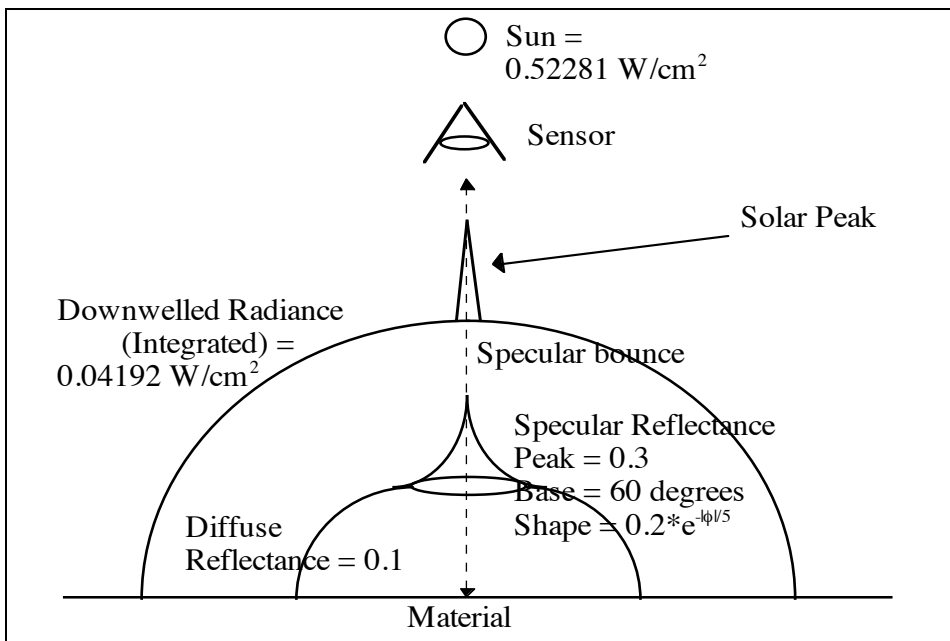


Figure 5.3. Case 2b Radiance and Reflectance Maps: Specular bounce direction changed (Sun moved to nadir).

In Case 2b, the specular reflectance component is present. The sun has been moved such that it is in the specular bounce direction.

Table 5.2. No Specular Reflectance Error Calculation Results

	<b>Calculations</b>	<b>L [W/cm<sup>2</sup>]</b>	<b>Error [%]</b>
BASE CASE		0.05680	0.0
Case 2a	$0.1 * (0.52281 + 0.04192)$	0.05647	-0.6
Case 2b	$(0.25 * 0.52281) + (1/8 * 0.16335 * 0.04192) + (7/8 * 0.1 * 0.04192)$	0.13523	138.1
	Note: The 0.25 specular reflectance is an estimated average over the solid angle of the sun		

The results of Case 2a show that, for the initial imaging conditions setup, not modeling specular reflectance results in only a 0.6 % error. However, Case 2a shows that an error of 138% can occur if the sun is in the specular bounce direction. Most remote sensing imaging conditions are similar to those of Case 2a (initial setup). This means that the error produced by the conditions of Case 2b are only like to occur locally, due to the particular orientation of that material, and not generally over the whole scene.

### CASE 3: Downwelled Radiance and Shape Factor

In Case 3, the effect of modeling the downwelled radiance and shape factor are determined. The first case (Case 3a) determines the effect of not modeling downwelled radiance at all and is shown in Figure 5.4. The second case (Case 3b) determines the

effect of shape factor with respect to downwelled radiance and is shown in Figure 5.5. The third and fourth cases (Case 3c and 3d) determine the effect of shape factor in general and are shown in Figure 5.6. The last case (Case 3e) determines the effect of not modeling the fall-off in reflectance at large zenith angles and is shown in Figure 5.7. The net effect is similar to effect of shape factor so it is presented here. The results for all the cases are shown in Table 5.3.

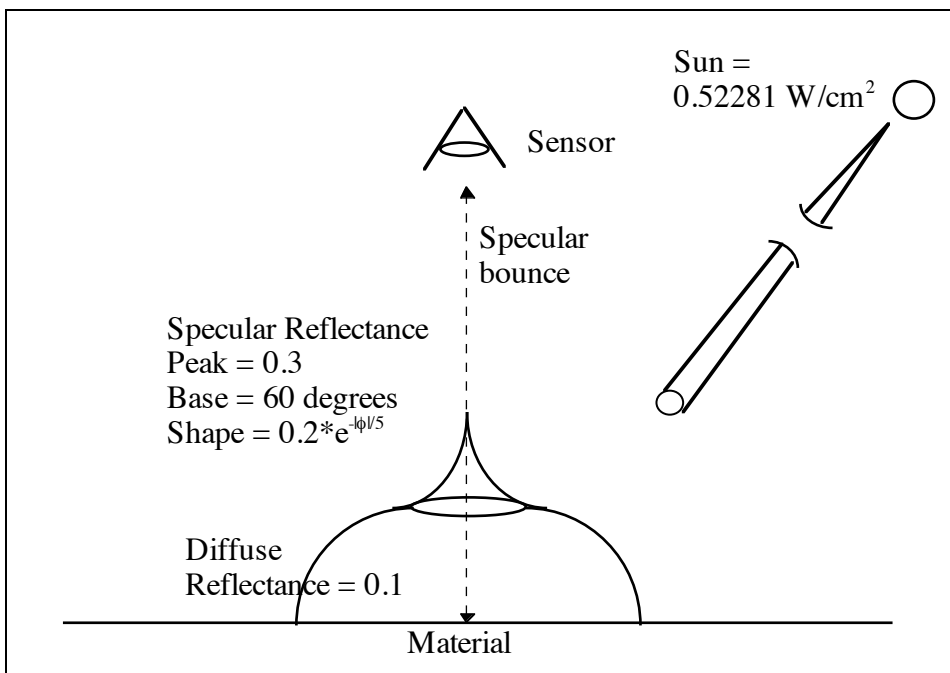


Figure 5.4. Case 3a Radiance and Reflectance Maps. No Downwelled Radiance.

In Case 3a, the downwelled radiance portion of the radiance map has been removed.

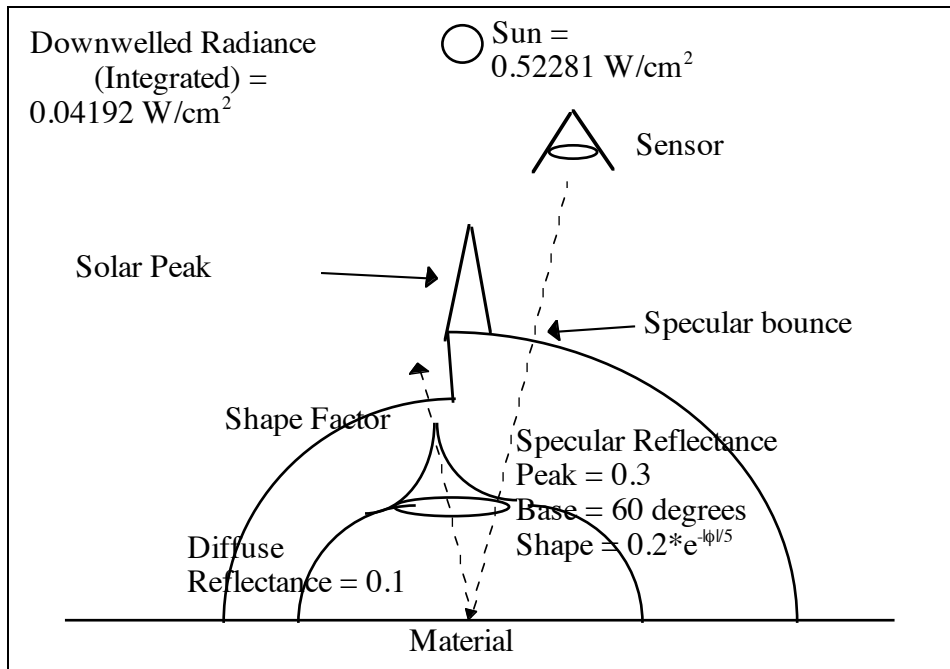


Figure 5.5. Case 3b Radiance and Reflectance Maps: Shape Factor is 0.5 and sun at nadir.

In Case 3b, half of the downwelled radiance map (shape factor 0.5) is obscured by other objects and the sun has been moved such that it illuminates the material but does not reflect off other objects onto the material. Note that the sun is still at a zenith angle of 45 degrees and thus not in the specular bounce direction. The reflectance of the background object is 0.1 and reflects only the downwelled radiance.

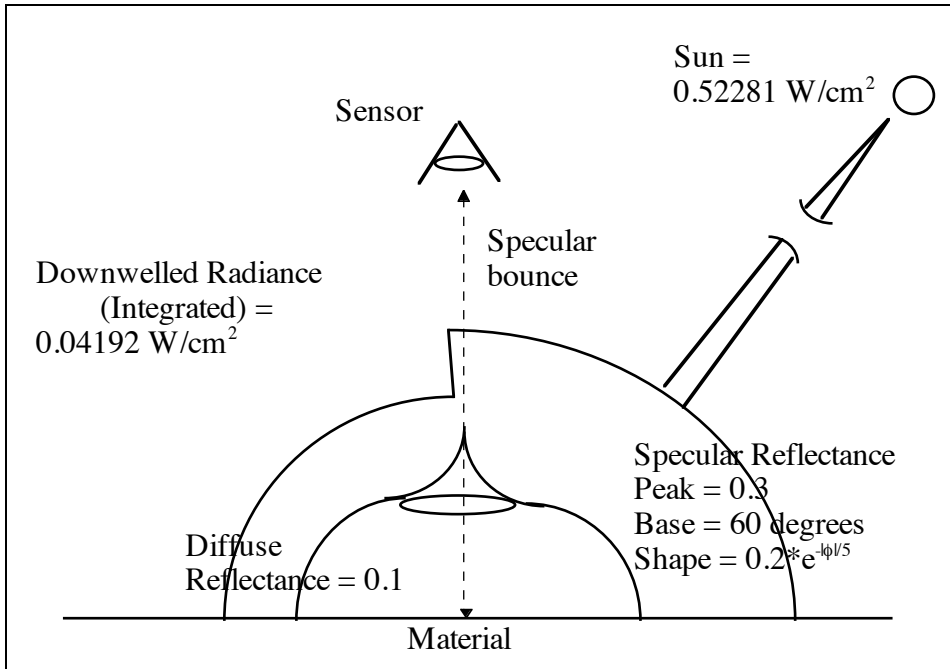


Figure 5.6. Case 3c and 3d Radiance and Reflectance Maps. Shape factor is 0.5 and sun at 45 degrees.

In Case 3c, the shape factor is 0.5 and the reflectance of the background object is 0.1. The solar radiance now reflects off of the background object onto the material. Case 3d is the same as Case 3c except that the reflectance of the background object is 0.4 (specular).

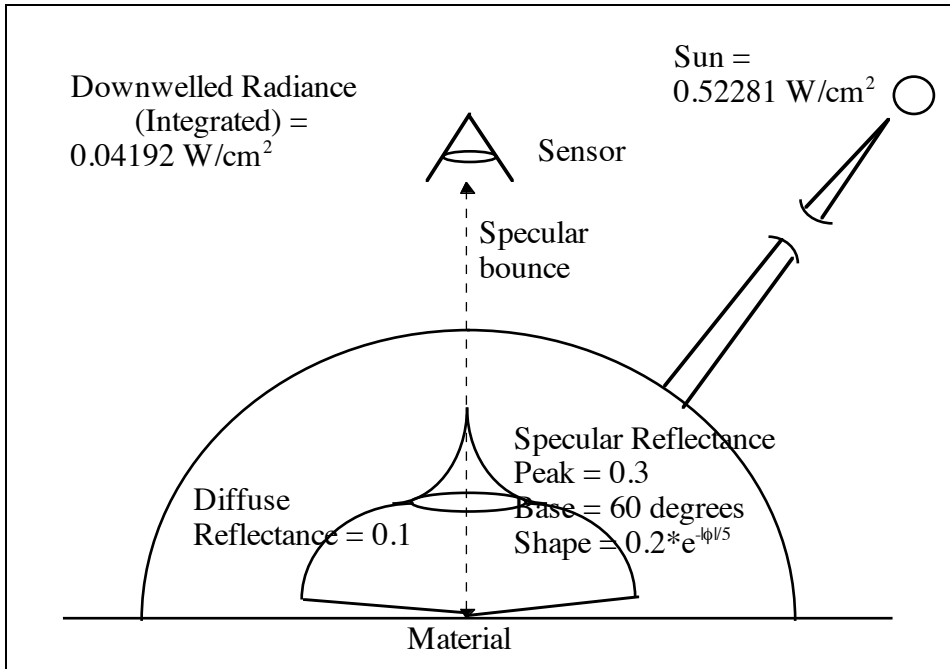


Figure 5.7. Case 3e Radiance and Reflectance Maps. Reflectance reduction at high zenith angles

In Case 3e, the reflectance at high zenith angles has been reduced to 0.0. The reduced area covers 1/8 of the hemisphere above the target.

Table 5.3. Downwelled Radiance and Shape Factor Error Calculation Results

	<b>Calculations</b>	<b>L</b> <b>[W/cm<sup>2</sup>]</b>	<b>Error</b> <b>[%]</b>
BASE CASE		0.05680	0.0
Case 3a	$0.1 * 0.52281$	0.05228	-8.0
Case 3b	$(0.1 * 0.52281) + (1/2 * 0.1 * 0.02096) + (2/16 * 0.16335 * 0.1 * 0.02096) + (6/16 * 0.1 * 0.1 * 0.02096) +$	0.05345	-5.9
Case 3c	$(0.1 * 0.52281) + (0.1 * 0.1 * 0.52281) + (1/2 * 0.1 * 0.02096) + (1/2 * 0.1 * 0.1 * 0.02096) + (1/16 * 0.16335 * 0.02096) + (1/16 * 0.16335 * 0.1 * 0.02096)$	0.05890	3.7
Case 3d	$(0.1 * 0.52281) + (0.1 * 0.4 * 0.52281) + (1/2 * 0.1 * 0.02096) + (1/2 * 0.1 * 0.4 * 0.02096) + (1/16 * 0.16335 * 0.02096) + (1/16 * 0.16335 * 0.4 * 0.02096)$	0.07496	32.0
Case 3e	$(0.1 * 0.52281) + (1/8 * 0 * 0.04192) + (6/8 * 0.1 * 0.04192) + (1/8 * 0.16335 * 0.04192)$	0.05628	-0.9

The results show that downwelled radiance and shape factor are significant contributors to the radiance exiting the material, contributing approximately 6-8% error. For the case of specular background objects, normally only a local condition, the error is 32%. The contribution of a reduction in reflectance at high zenith angles was insignificant, less than 1%. This is true as long as the sun is not at high zenith angles, a condition that is not common in remote sensing.

#### CASE 4: High Oblique View Angles

In Case 4, the effect of the reduction in reflectance at high oblique view angles is determined. The setup is shown in Figure 5.8 and the results are shown in Table 5.4.

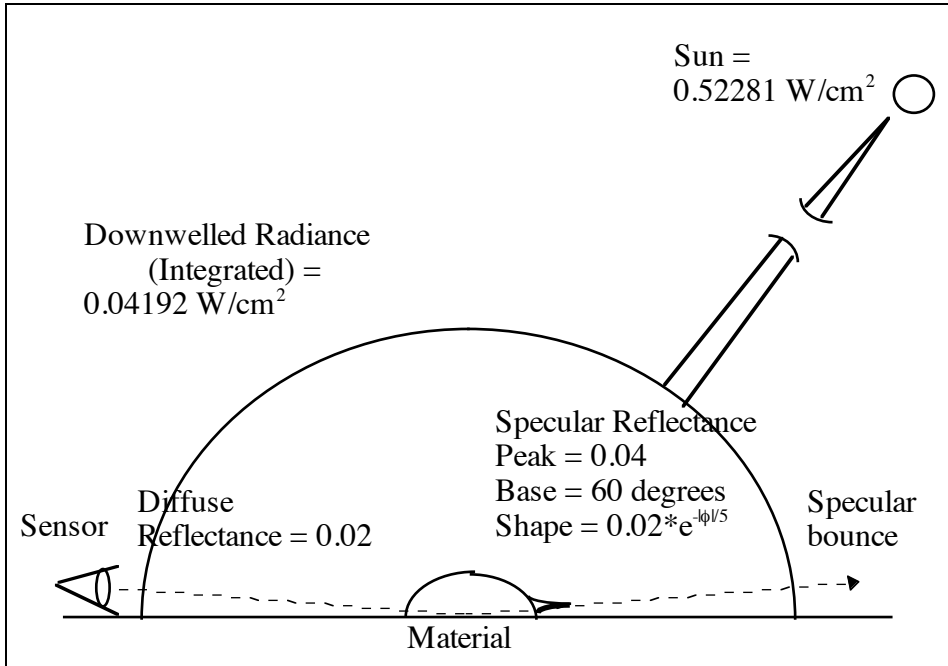


Figure 5.8. Case 4 Radiance and Reflectance Maps. Reflectance reduction at High Oblique View Angles.

In Case 4, the reflectance has been reduced to 0.02 and the peak specular lobe to 0.04. The goal is to model the phenomena of a reduction in the radiance exiting a material when viewed from a high oblique angle. Since the radiance the material “sees” is unchanged there must be a reduction in reflectance. The nature of the reductions made in this analysis is an attempt to model an unknown. Note that these imaging conditions are local.

Table 5.4. High Oblique Viewing Angle Error Calculation Results

	<b>Calculations</b>	<b>L</b> <b>[W/cm<sup>2</sup>]</b>	<b>Error</b> <b>[%]</b>
BASE CASE		0.05680	0.0
Case 4	$(0.02 * 0.52281) + (1/8 * 0.02633 * 0.04192) + (7/8 * 0.02 * 0.04192)$	0.01793	-68.4

The results show that not accounting for the reduction in reflectance at high oblique viewing angles can cause significant error, 68%.

This simple analysis showed that to create a robust SIG model it must account for all of the parameters listed. A robust model is able to model general and local conditions and a variety of imaging conditions. It also should provide a context by which the formal sensitivity analysis presented in the next section can be viewed.

### 5.1.2 Sensitivity Analysis of the Big Equation (Visible Spectrum) - DIRSIG

The Big Equation as implemented by DIRSIG is given by

$$\begin{aligned} & \text{total\_radiance} = \\ & \text{total\_transmission} * \\ & (((\text{solar\_scattering\_term} + \text{background\_specular\_component}) * \text{specular\_reflectivity} * (\text{specularity})) + \\ & ((\text{solar\_scattering\_term} + \text{background\_diffuse\_component}) * \text{diffuse\_reflectivity} * (1 - \text{specularity})) + \\ & \text{emissive\_component}) + \text{upwelled\_radiance} \end{aligned}$$

where

total_transmission	- $\tau_2$ - the atmospheric transmission coefficient between the target and the sensor
solar_scattering_term	- $E_s \cos(\sigma) \tau_1 / \pi$ - the solar radiance reduced by the atmospheric transmission coefficient between the sun and the target
background_specular_component	- the specular radiance on the target from direction of the sun and from the specular direction
specular_reflectivity	- reflectivity in the specular direction
specularity	- the overall specular reflectivity, corresponds to the volume of the specular lobe when combined with the specular_reflectivity
background_diffuse_component	- the diffuse irradiance on the target from the direction of the sun and from multiple directions in the hemisphere above the facet
diffuse_reflectivity	- reflectivity from all directions except the specular direction
emissive_component	- output of the therm submodel
upwelled_radiance	- $L_{us}$ upwelled radiance

or, using standard (non-programming) terminology by

$$L_{\lambda} = \tau_2(\lambda) \left[ \begin{array}{l} \left( \frac{E'_{s\lambda} \cos \sigma' \tau_1(\lambda)}{\pi} + L_{ds\lambda\_specular} \right) r_{specular}(\lambda) \text{specularity} + \\ \left( \frac{E'_{s\lambda} \cos \sigma' \tau_1(\lambda)}{\pi} + L_{ds\lambda\_diffuse} \right) r_{diffuse}(\lambda) (1 - \text{specularity}) + \\ L_{\epsilon} \end{array} \right] + L_{us\lambda}(\theta, \phi)$$

Where

$r_{specular}$  is the specular lobe peak

$L_{ds\_specular}$  is the radiance from the specular direction

$r_{diffuse}$  is the diffuse reflectivity

$L_{ds\_diffuse}$  is the radiance from the hemisphere above the material

The error (squared) for this equation takes the form, assuming no cross correlation, of (Beers, 1957)

$$S_Y^2 = \left[ \left( \frac{\partial Y}{\partial X_1} S_{X_1} \right)^2 + \left( \frac{\partial Y}{\partial X_2} S_{X_2} \right)^2 + \dots + \left( \frac{\partial Y}{\partial X_N} S_{X_N} \right)^2 \right]$$

The error (squared) in total\_radiance ( $S_{\text{total\_radiance}}$ ) is then given by

$$\begin{aligned}
S_{\text{total\_radiance}}^2 = & \\
& ((\text{solar\_scattering\_term} + \text{background\_specular\_component}) * \\
& \quad \text{specular\_reflectivity} * \text{specularity} + (\text{solar\_scattering\_term} + \\
& \quad \text{background\_diffuse\_component}) * \text{diffuse\_reflectivity} * (1 - \text{specularity})) * S_{\text{total\_transmission}}^2 \\
+ & (\text{total\_transmission} * (\text{specular\_reflectivity} * \text{specularity} + \\
& \quad \text{diffuse\_reflectivity} * (1 - \text{specularity}))) * S_{\text{solar\_scattering\_term}}^2 \\
+ & (\text{total\_transmission} * \text{specular\_reflectivity} * \text{specularity} * S_{\text{background\_specular\_component}}^2) \\
+ & (\text{total\_transmission} * (\text{solar\_scattering\_term} + \\
& \quad \text{background\_specular\_component}) * \text{specularity}) * S_{\text{specular\_reflectivity}}^2 \\
+ & (\text{total\_transmission} * \\
& \quad (((\text{solar\_scattering\_term} + \text{background\_specular\_component}) * \\
& \quad \quad \text{specular\_reflectivity}) \\
& \quad - ((\text{solar\_scattering\_term} + \text{background\_diffuse\_component}) * \\
& \quad \quad \text{diffuse\_reflectivity}))) * S_{\text{specularity}}^2 \\
+ & (\text{total\_transmission} * \text{diffuse\_reflectivity} * (1 - \text{specularity}) * S_{\text{background\_diffuse\_component}}^2) \\
+ & (\text{total\_transmission} * ((\text{solar\_scattering\_term} + \\
& \quad \text{background\_diffuse\_component}) * (1 - \text{specularity}))) * S_{\text{diffuse\_reflectivity}}^2 \\
+ & (1 * S_{\text{upwelled\_radiance}}^2)
\end{aligned}$$

or, using standard (non-programming) terminology by

$$\begin{aligned}
S_{L_\lambda}^2 = & \\
& \left( \left[ \left( \frac{E'_{s\lambda} \cos \sigma' \tau_1(\lambda)}{\pi} + L_{ds\lambda\_specular} \right) r_{specular}(\lambda) \text{specularity} + \right. \right. \\
& \quad \left. \left( \left( \frac{E'_{s\lambda} \cos \sigma' \tau_1(\lambda)}{\pi} + L_{ds\lambda\_diffuse} \right) r_{diffuse}(\lambda) (1 - \text{specularity}) \right) \right] * S_2 \right)^2 \\
+ & \left( \tau_2(\lambda) \left[ r_{specular}(\lambda) \text{specularity} + r_{diffuse}(\lambda) (1 - \text{specularity}) \right] * S_{E_{s\lambda} \tau_1 \cos \sigma / \pi} \right)^2
\end{aligned}$$

$$\begin{aligned}
& + (\tau_2(\lambda)r_{specular}(\lambda)specularity) && * S_{Lds\_specular})^2 \\
& + (\tau_2(\lambda)\left(\frac{E'_{s\lambda} \cos \sigma' \tau_1(\lambda)}{\pi} + L_{ds\lambda\_specular}\right)specularity) && * S_{R\_specular})^2 \\
& + (\tau_2(\lambda)\left[\left(\frac{E'_{s\lambda} \cos \sigma' \tau_1(\lambda)}{\pi} + L_{ds\lambda\_specular}\right)r_{specular}(\lambda) - \right. && \\
& \quad \left. \left(\frac{E'_{s\lambda} \cos \sigma' \tau_1(\lambda)}{\pi} + L_{ds\lambda\_diffuse}\right)r_{diffuse}(\lambda)\right] && * S_{specularity})^2 \\
& + (\tau_2(\lambda)r_{diffuse}(\lambda)(1 - specularity)) && * S_{Lds\_diffuse})^2 \\
& + (\tau_2(\lambda)\left(\frac{E'_{s\lambda} \cos \sigma' \tau_1(\lambda)}{\pi} + L_{ds\lambda\_diffuse}\right)(1 - specularity)) && * S_{R\_diffuse})^2 \\
& + (1 && * S_{us})^2
\end{aligned}$$

The estimated error (S) for each of the variables is given in Table 5.5. The source data for these estimates comes from prior DIRSIG testing and engineering judgment. The error assumes a one sigma probability distribution.

Table 5.5. Error Variable Values

Error Variable	Value (%)
S <sub>total_transmission</sub>	4
S <sub>solar_scattering_term</sub>	8.85
S <sub>background_specular_component</sub>	6.35
S <sub>specular_reflectivity</sub>	2.5
S <sub>specularity</sub>	5.0
S <sub>background_diffuse_component</sub>	6.35
S <sub>diffuse_reflectivity</sub>	2.5
S <sub>upwelled_radiance</sub>	6.35

The analysis considers two cases. In the first case, the target is sunlit on a cloudless day on a horizontal surface away from any tall objects. In the second case, the target is in the shadow of a diffuse object. Both cases use a nadir perspective with the sensor at an

altitude of one kilometer and the sun not in the specular direction. The sensor is assigned a field-of-view of 20 degrees (-10 to 10 degrees). The setup is shown in Figure 5.9.

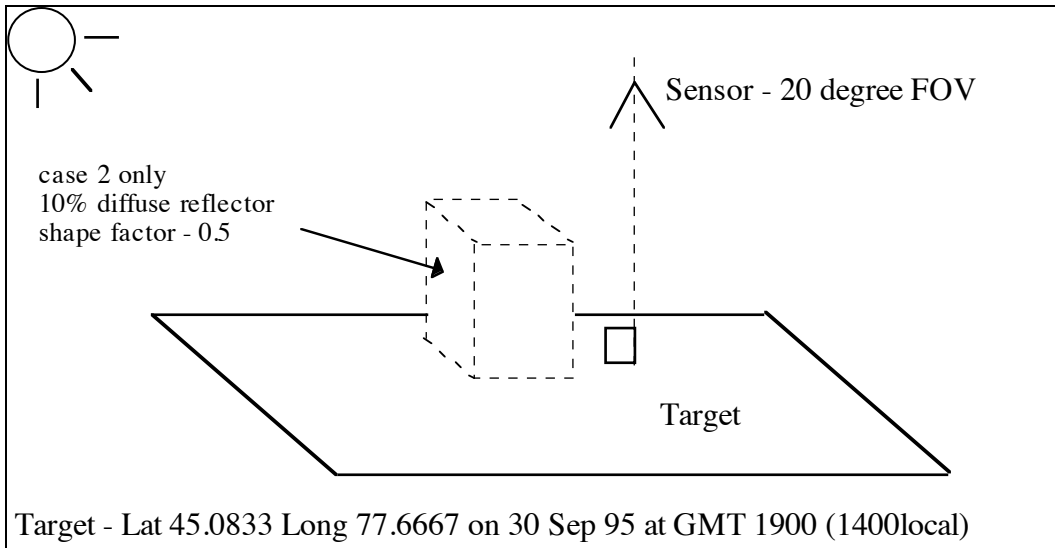


Figure 5.9. Sensitivity Analysis Setup

The target is a gray 15% reflector with a specular lobe which has a peak at 20% and covers 10% of the hemisphere. This is shown in Figure 5.10.

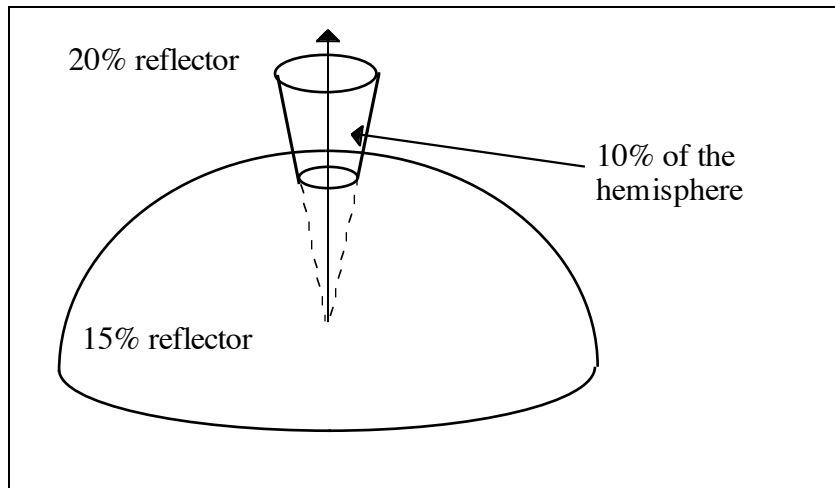


Figure 5.10. BRDF of target material

The tall object in the second case is a gray 10% diffuse reflector and causes only half the sky to be visible to the target (and not the sun.)

Inputs to the analysis were obtained by running `build_radiance` for the scenario described above. Each band; red, green, and blue, was analyzed separately. The results are shown in Table 5.6 for Case 1 and Table 5.7 for Case 2 (The changed parameters from Case 1 are highlighted.)

The results from Case 1 show that the `solar_scattering_term` ( $E_s \cos \sigma / \pi$ ) is the largest contributor to the overall error, about 50%. This is not unexpected, the magnitude of radiance from an object in the sun compared to the same object in the shade varies greatly. The analysis shows that the error is roughly equal across the bands (slightly less for the blue). This means that, given the high correlation between bands across the scene, errors in estimating the `solar_scattering_term` will act as a bias in the image.

The second largest contributor is the total transmission ( $\tau_2$ ), at 26%, and is constant across the bands. Again, an error in estimating this parameter will act as a bias in the radiance calculations. The third largest contributor is the diffuse reflectivity, at 14%, and is constant across the bands. However, unlike the first two contributors, diffuse reflectivity will change across the scene (with material). Thus the final image statistics will be impacted by errors in estimating this parameter and must be modeled with a high degree of fidelity.

The error in the `upwelled_radiance` and the `background_diffuse_component` is approximately 4% in the blue band and 2% in the green and red bands. The difference between bands reflects the magnitude of the radiance in those bands. Again, the `upwelled_radiance` and `background_diffuse_component` are constants across a scene.

Of particular significance in the analysis is the low impact of “specular” factors (specular\_reflectivity, specularity, and background\_specular\_component). Combined they contribute less than four percent of the error. This means that for scenes of this type, such as agricultural land, imaged under these conditions, the reflectance model can be simplified. The analysis also highlighted another error source. Even though the sun was not in the specular bounce direction, part of its contribution was reduced by the specular\_reflectivity \* specularity factor rather than the diffuse\_reflectivity \* (1-specularity) factor as it should have been. The specular\_reflectivity \* specularity factor was 0.02 [0.2 \* 0.1] and the diffuse\_reflectivity \* (1-specularity) factor was 0.135 [0.15 \* (1-0.1)]. This results in an effective reflectance against the sun of 0.155 rather than the actual 0.135, an error of 14.8%. For more “specular” situations this could be very significant. For example, given a diffuse\_reflectivity of 0.1, a specular\_reflectivity of 0.4, and a specularity of 0.25, the effective reflectivity would be 0.175 [0.4 \* 0.25 = 0.1 plus 0.1 \* (1 - 0.25) = 0.075 ] rather than the actual 0.075, an error of an 133%! The reverse situation (Cases 3 and 4) occurs when the sun IS in the specular bounce direction, part of its contribution will be attenuated by the diffuse\_reflectivity \* (1-specularity) factor rather than the correct specular\_reflectivity \* specularity factor.

The Case 2 analysis shows that the upwelled\_radiance becomes the dominate error contributor in the shadowed portions of the scene, at 45-38%. The next largest contributors are the background\_diffuse\_component and the total\_transmission, at 20-30%. This is followed by the diffuse reflectivity and the “specular” factors. Again, the contribution due to errors in the “specular” factors is small and indicates that a high fidelity reflectance model will allow for only a small gain in the overall performance of the SIG model.





### 5.1.3 Sensitivity Analysis of the Reflectivity Model

To measure the sensitivity of the Big Equation to the effects of the BDRF nature of reflectance, two additional cases were run. The first case (Case 3) matches Case 1 except that the specular bounce from the sensor strikes the sun. The setup is shown in Figure 5.11 and the results in Table 5.8 (The changes in input are shaded.) The only change was in the background\_specular\_component, which was increased from 10% of the downwelled radiance to 15%. This was to allow for the non-symmetry of the downwelled radiance. Downwelled radiance increases as you approach the direction of the sun.

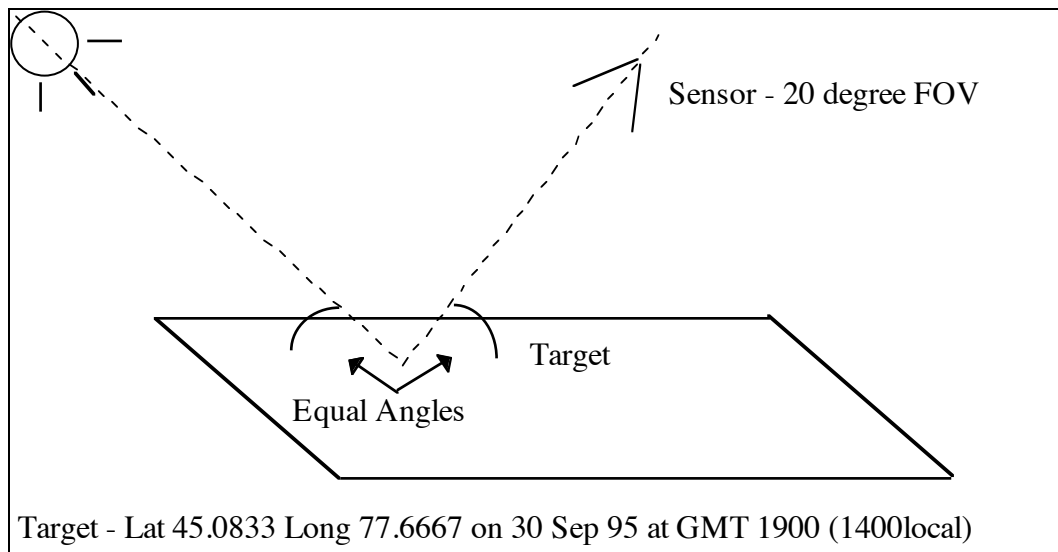


Figure 5.11. Sensitivity Analysis Setup

The second case (Case 4) matches Case 3 except that the target is more specular. The specular reflectance is 40 % and covers 25% of the hemisphere above the material. The diffuse reflectivity is 10%. The results are shown in Table 5.9 with the changes shaded.

The results of Case 3 are virtually the same as Case 1. This is because, as described earlier, reflectivity is not sensitive to the position of the sun. The results of Case 4 show a marginal increase in the error associated with the “specular” factors. If reflectivity were sensitive to the position of the sun the impact would be greater.





#### 5.1.4 Recommendations

Based on the sensitivity analysis and an understanding of DIRSIG the following recommendations are provided to assist the scene builder in developing more radiometrically accurate synthetic scenes. The recommendations are for the situation where a change in perspective is desired.

1. Model the radiance map above the scene as accurately as possible, especially the sun. This map is then fixed for changes in perspective.
2. Model the diffuse reflectivity as accurately as possible. Again, this map is then fixed for changes in perspective and should be valid except at very high oblique angles.
3. Sample the radiance and reflectance maps more frequently (cast more secondary rays), especially in areas of activity, i.e. the sun, the specular lobe, and transitions from background objects to the sky.
4. Adjust the specular lobe parameters. This will be more important when building a scene with many “specular” factors, i.e. specular material and specular angles.
5. Adjust the orientation of the facets. This is important when the “effective” shape factor is important. Local orientations within a facet may vary significantly. An example is a hill modeled by only a few facets.
6. Apply texture maps. This is important both for visual acceptability as well as for images that will serve as input to classification algorithms.
7. Cast more primary rays to create mixed pixels through pixel aggregation.

## 5.2 Proposed Model

The recommended model attempts to balance radiometric accuracy, the ability to obtain reflectance data, and computational requirements (limitations).

### 5.2.1 Basis and Structure of the Proposed Model

There are two components that affect the amount of radiance leaving a facet, the radiance sources in view of the facet and the facets directional reflectivity characteristics.

The radiance the facet receives can be described as a map covering the hemisphere over the facet. This concept is illustrated in Figure 5.12.

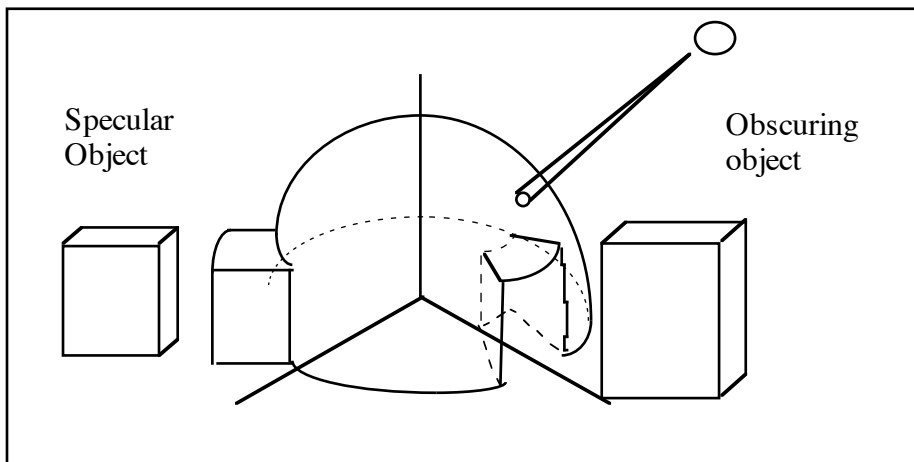


Figure 5.12. Radiance map above a facet.

The height of the surface above the facet indicates the amount of radiance the facet receives from that direction. Of course, the primary source is from the sun as indicated with the large “bump” or “spike”. Other “bumps” on the surface can come from secondary (self-emitting) sources, from solar radiance reflections from specular objects,

or reflections from very light colored secondary surfaces. “Dips” in the surface can come from the effects of transmissive objects, such as clouds and vegetation, obscuring objects, or from dark secondary surfaces. The map for a facet changes with wavelength and time of day.

The reflective characteristics of the facet can also be described as a map over the hemisphere above the facet. This concept is illustrated in Figure 5.13.

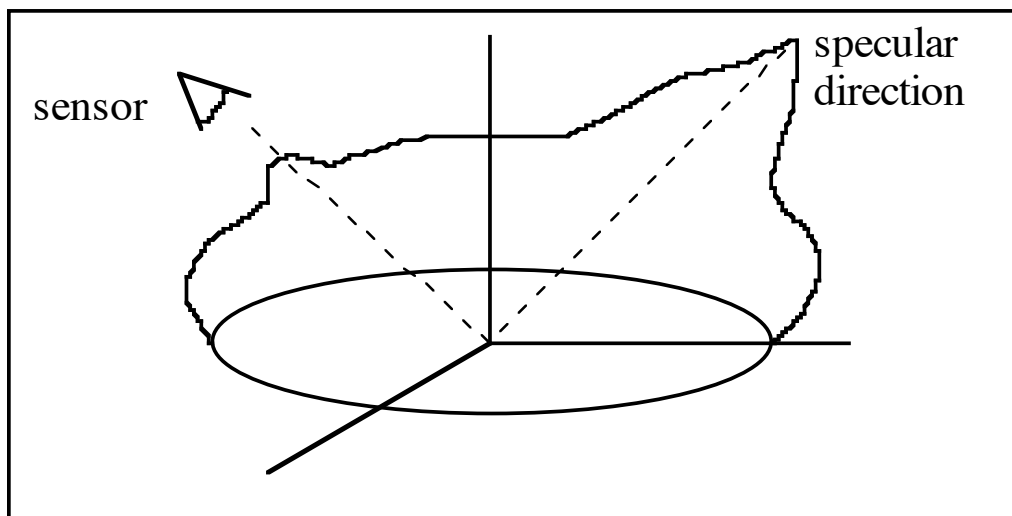


Figure 5.13. Reflectance map for one wavelength and viewing angle.

The primary “bump” is in the specular direction. The secondary “bump” is due to the opposition effect. The reduction in the map at high angles from zenith is an observed phenomena. The map for a facet changes with wavelength and viewing angle (both the size and position of the specular “bump”).

The radiance leaving the facet is a multiplication of the two maps on a solid angle by solid angle basis. This is in essence the proposed model. The radiometric accuracy of the model is then a function of the fidelity of the maps and the proper sampling of them.

## Radiance Map

DIRSIG currently produces what is in essence a radiance map in the form of the .rad files produced by the build\_radiance program. Each file contains the spectral band pass, azimuth and zenith angles, and the downwelled radiance. They do not contain the solid angle (or percent of the hemisphere above the target) over which the calculations are valid. DIRSIG assumes that the radiance map is valid for the whole scene not just an individual facet. This assumption is reasonable for all but very large, 10's to 100's of square kilometer, scenes. DIRSIG also assumes a flat world (at any elevation), the map covers only a hemisphere. Again, this is reasonable for all but a few "special" scenes. The solar radiance and its location are provided via the Therm Submodel. Dips and secondary bumps in the radiance map are provided through the ray-tracer submodel, it determines the shape factor and accesses the reflectance values of background objects.

The proposed model uses this radiance map but recommends the following modifications to increase its fidelity and, in the future, decrease its computational requirements.

- Provide the solid angle values over which the calculations were made. This can be accomplished in a couple of ways; sample uniformly (golf ball) such that all the solid angles are the same and thus the solid angle can be assumed or provide the solid angles with the radiance values. The second approach would require more computational power.
- Sample the map more frequently to reduce sampling error. The trade for this recommendation must be made against the error contributed by the downwelled radiance (less than 4%) and computational requirements.

Future:

- Degenerate the map into a 3-dimensional mathematical function (surface). Because the surface is well behaved a suitable function which requires only a few parameters and relatively little computing should be relatively easy to develop. This would reduce the overall computational requirements and potentially allow for an integration approach (discussed in the sampling section) to determine the radiance exiting a facet.

Testing of the radiance map fidelity can be accomplished independent of a DIRSIG scene by comparing calculated values with experimental data.

### Reflectance Model

The proposed model relies on experimental measurements and the symmetry of the BDRF data, as many models do, as a way of reducing computational requirements. It begins with a dome and adds a mathematical function to describe the spectral lobe. The height of the dome is a function of wavelength and view angle. The shape of the lobe is controlled by a choice of functions and up to four parameters. The functions proposed include a cone, a delta function, a cosine function, and an exponential function. The parameters used at this time include wavelength (not counted as one of the parameters), zenith angle [degrees], base radius [degrees], and the height of the lobe [reflectance units]. The validity of this approach was shown by Culpepper (1995). He was able to model three materials to within 2% data for any combination of illumination and viewing angles by using an exponential function and interpolation of experimental. His approach assumed perfect sampling.

The various options for the specular lobe function are described below. The actual (reference) specular lobe is shown in Figure 5.14.

- Actual (reference) specular lobe.

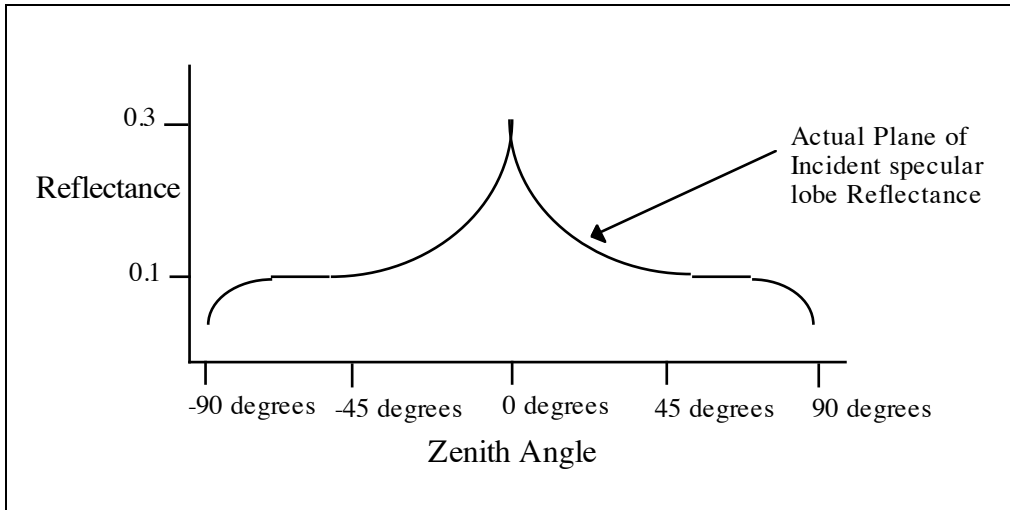


Figure 5.14. Actual reflectivity of the sample.

From 90 degrees to approximately 85 degrees it increases from 0 to 0.1 reflectance units. From 85 degrees until +/- 45 degrees it has a constant value of 0.1 reflectance units. From +/- 45 degrees to 0 degrees it increases from 0.1 to 0.3 reflectance units. All the figures assume a nadir perspective. The thick lines in each figure are the proposed model, the thin lines are the actual reflectivity.

- A delta function - This is the current DIRSIG approach and is reasonably valid for many situations and is computationally simple. The parameters which control the function include wavelength, lobe height, zenith angle, and base area (specularity). It is shown in Figure 5.15.

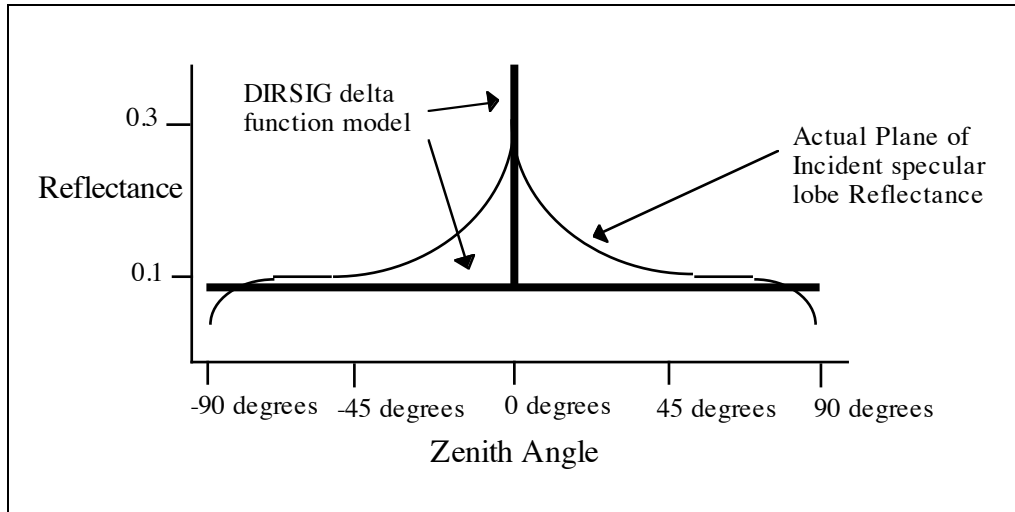


Figure 5.15. DIRSIG delta function model of the specular lobe.

The DIRSIG model has a constant value of 0.1 except at 0 degrees where it is a pre-determined value. The pre-determined value is chosen such that when multiplied by the specularity of the material, it equals the volume of the actual specular lobe.

- A cone - This is the initial recommendation, White's model. The parameters used to control the function include wavelength, lobe height, base radius, and zenith angle.

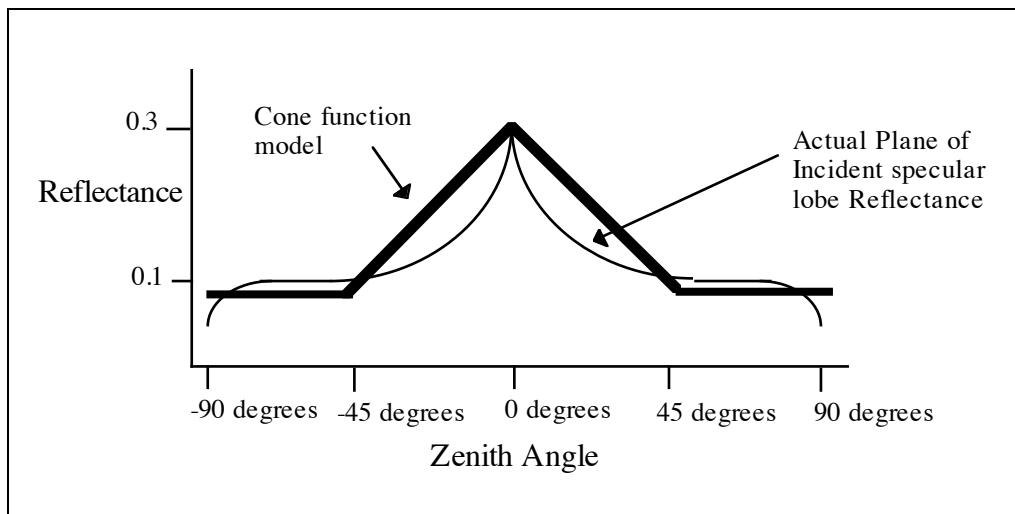


Figure 5.16. Cone model of the specular lobe.

The reflectance is constant at 0.1 until +/- 45 degrees where it increases linearly to 0.3 at 0 degrees.

- A cosine function raised to a power - This is a modified version of the Phong model. The parameters used to control the function include wavelength, lobe height, base radius, zenith angle, and slope shaper (exponent).

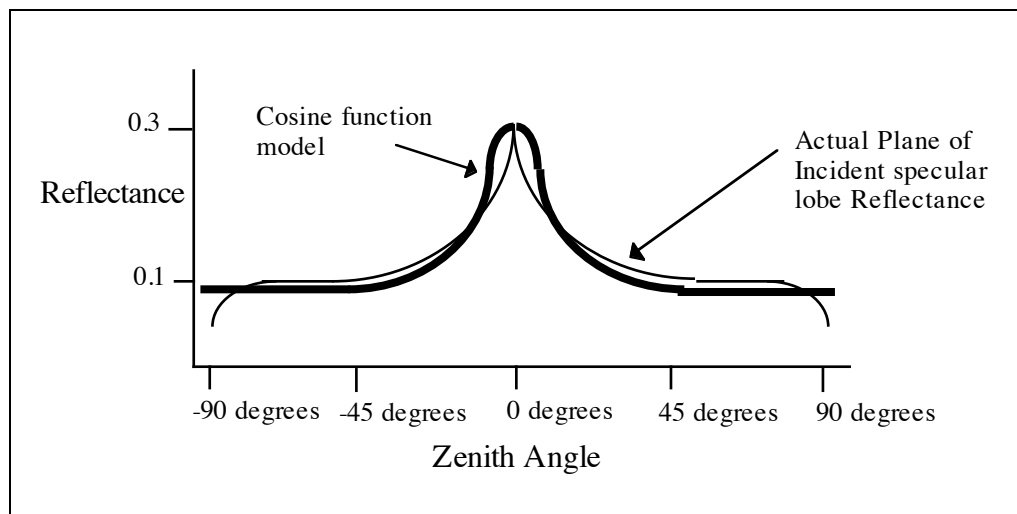


Figure 5.17. Cosine model of the specular lobe.

The reflectance is constant at 0.1 until +/- 45 degrees where it increases as a cosine raised to a power ( $\text{spectral\_reflectance} + \text{Peak\_value} * \cos(2\theta)^x$ ). (The angles are doubled in the example to allow the function equal zero at 45 degrees.)

- An exponential function - This is a modified version of the Culpepper model. The parameters used to control the function include wavelength, lobe height, base radius, zenith angle, and other parameters as needed to control the slope shape.

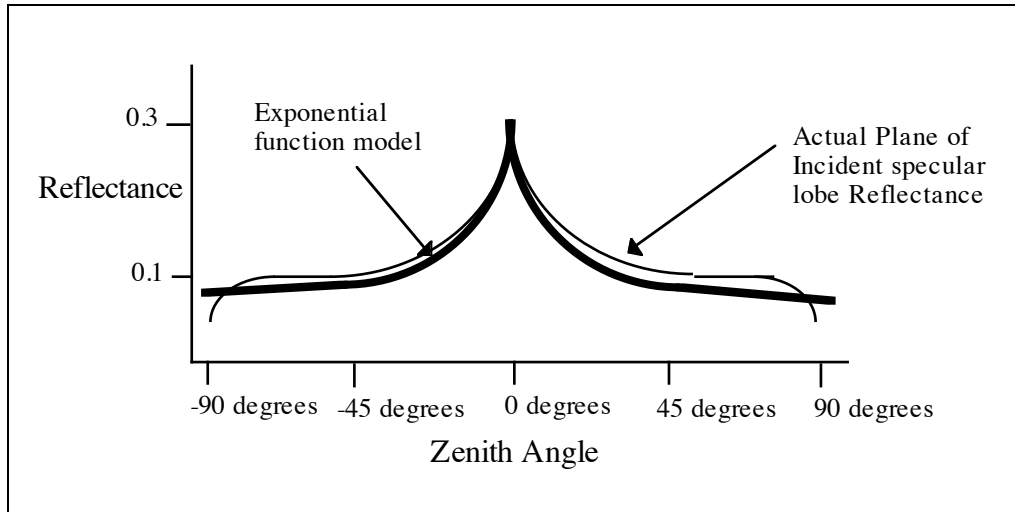


Figure 5.18. Exponential model of the specular lobe.

The reflectance increases very slowly about 0.1 until +/- 45 degrees where it increases to 0.3 at 0 degrees. The entire curve is modeled by the function

$$BRDF = \frac{r}{\pi} + a * e^{-\frac{|zenith\ angle|}{b}}$$

where  $r/\pi$  is the diffuse reflectivity

$a$  and  $b$  are constants chosen to control the shape of the lobe.

- Interpolation - This is a future recommendation. The approach simply stores a sufficient number of experimental values to describe the slope shape for a sufficient number of zenith angles and wavelengths.

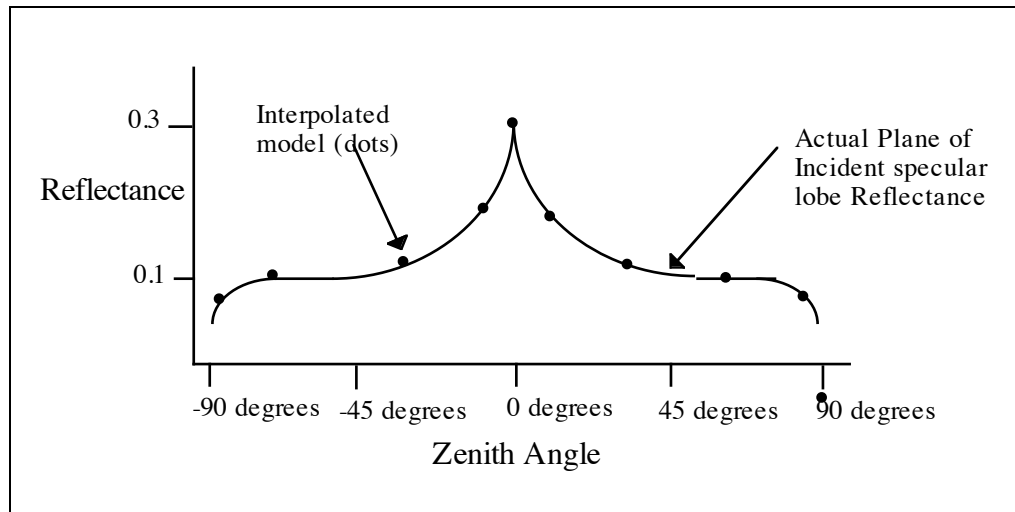


Figure 5.19. Interpolated data model of the specular lobe.

The reflectance is an interpolation between the measured values. The interpolation could be linear or a polynomial depending the amount of data available and the fidelity required.

To model the phenomena of reduced reflectance at high zenith angles, the proposed models include the option of multiplying the surfaces described by an attenuating function (fall-off). The function is a pseudo dome whose height decreases with zenith angle.

To model the phenomena of reduced reflectance at high viewing angles, the overall value of the radiance exiting the material can be reduced by multiplying the same attenuating function. In this case, the function is a pseudo dome whose height decreases with viewing angle.

Testing of the model requires comparison of the surfaces produced by the model to BRDF data.

Disadvantages/Drawbacks:

- The model assumes an azimuthal symmetry. This is not always true, an example is mowed grass. To model this additional maps must be used. (See Section 5.2.4)
- The model also does not inherently provide for texture. To model this, texture maps must be used. (See Section 5.2.4)
- Lastly the model does not allow for changes in resolution. To model resolution, the aggregate aperture used to acquire experimental data must be approximately equal to the resolution of the image.
- The size of the spectral lobe is not a function of wavelength other than to ensure that the lobe “sits” on the dome.

Now that the radiance maps and the reflectivity maps have been described, how they are combined to determine the radiance exiting a material must be addressed. The proposed model assumes that a ray-tracing approach will be used, which implies sampling.

### Sampling

The proposed model/algorithm to combine the maps is shown in Figures 5.20 and 5.21. Significant changes to the current model include how transmissive objects and secondary facets are handled. The changes are recommended based on a trade between computational requirements and the magnitude of the radiance contributions.

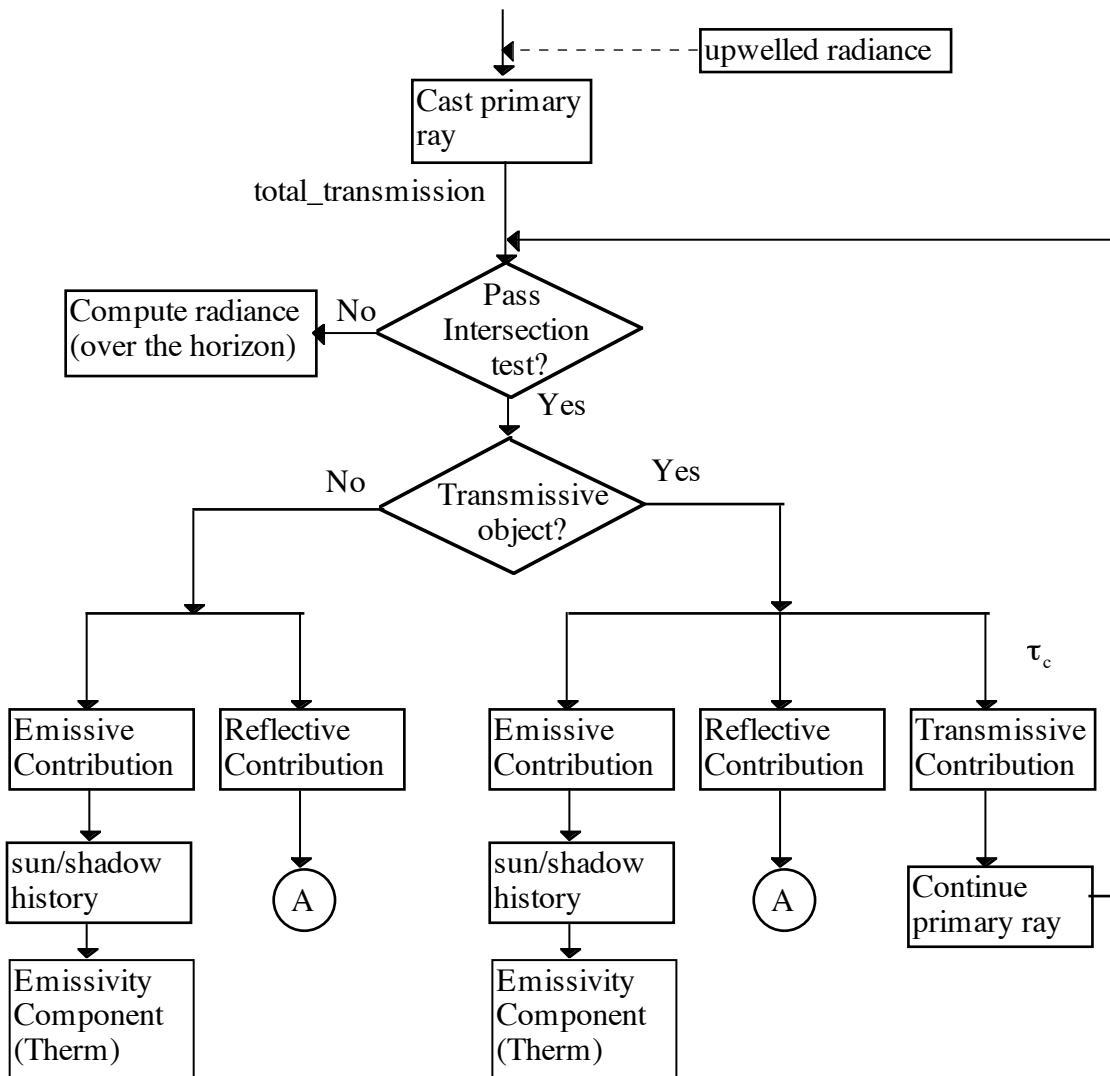


Figure 5.20. Proposed Ray Tracer Flow

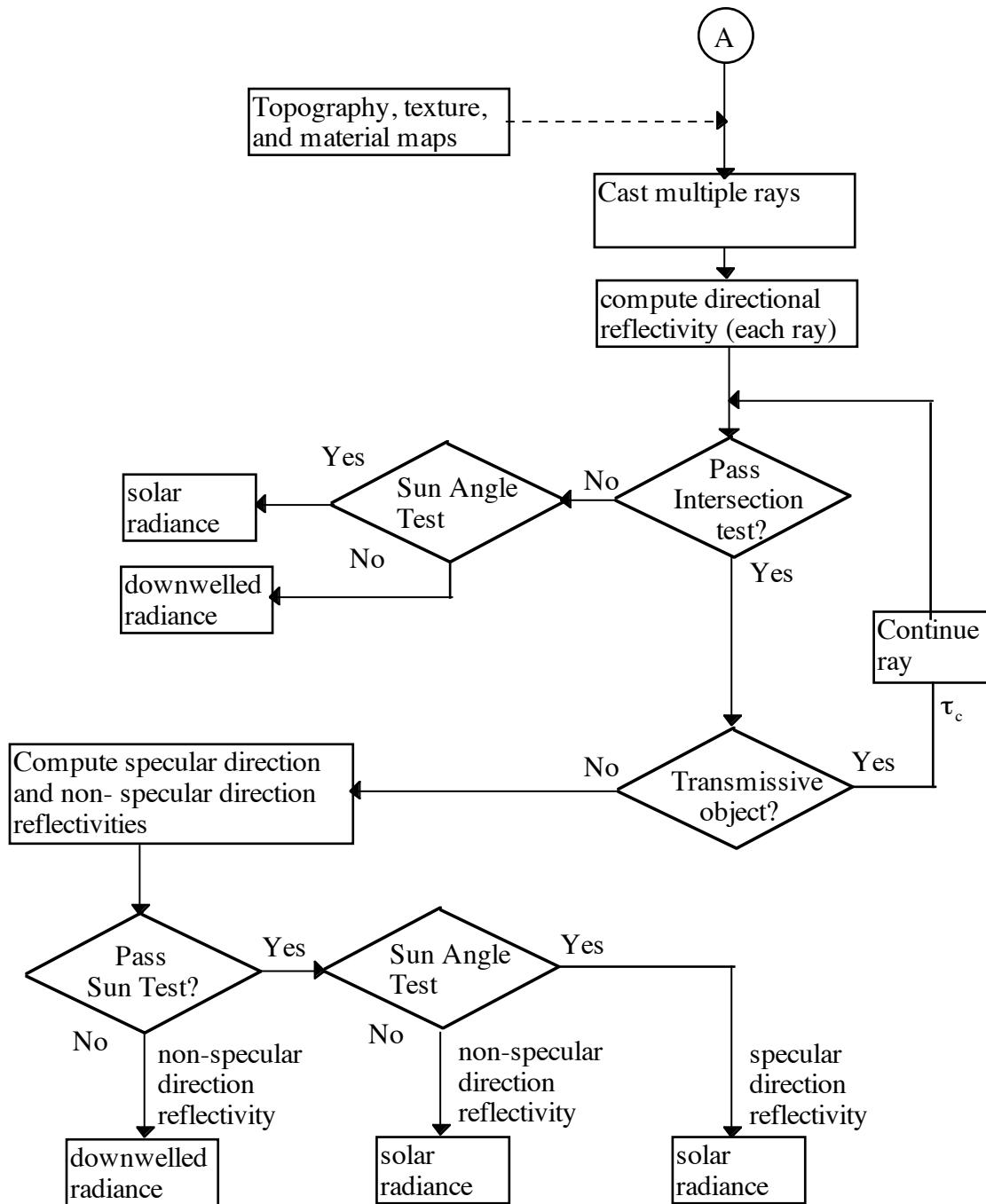


Figure 5.21. Proposed Ray Tracing Flow (continued)

The process begins by casting a ray from the focal plane (single pixel) onto the scene. The ray starts at the center of the pixel. The path of the ray is determined through sensor-scene geometry. Within the scene, the facet (if any) the ray strikes is determined through intersection tests. If the ray does not pass the intersection test (does not intersect a facet), it is assumed that the pixel is looking above the horizon and the effective radiance the pixel would see is computed. If the ray passes the intersection test, the transmissivity of the facet is tested.

If the facet is opaque, the emissive and reflective radiance contributions exiting the facet are determined. The emissive contribution is computed using the therm submodel. The reflective contribution is computed by casting multiple (secondary) rays from the primary facet. To ensure that the solar radiance is included, one of the rays is cast to the sun. The contribution from each of the rays is a function of the “sensitivity” (reflectivity) of the facet to radiance from that direction. If a secondary ray does not intersect a facet, the appropriate downwelled or solar radiance is used. If the ray intersects a transmissive facet, the transmittance is noted for reduction of the radiance from that direction and the ray is continued. If the ray intersects an opaque facet, two tests are performed. The first test will be to determine if the facet is sunlit and the second to determine if the specular direction points to the sun. If the specular direction of the second facet points to the sun, the solar radiance will be reduced by the specular reflectivity from that direction. If the second facet is sunlit the direct solar and downwelled radiance will be reduced by the diffuse reflectance. If the second facet is not sunlit, the downwelled radiance will be reduced by the spectral reflectivity.

If the facet is transmissive, the emissive, reflective, and transmissive contributions exiting the facet are determined. The emissive and reflective contributions are calculated in the same manner as if the facet were opaque. The transmissive contribution is determined by noting the transmittance of the facet for reduction of radiance coming from that direction

and by continuing the ray. It may be necessary in certain situations to limit the number of transmissive facets the primary ray is allowed to traverse. A situation where this may be recommended is in an oblique image of a forest canopy.

The emissive component, specular component, and the diffuse component are summed, multiplied by the atmospheric transmission coefficient, and then added to the upwelled radiance. This is the radiance reaching the sensor for that pixel.

Secondary rays:

The intelligent casting of secondary rays is very important to radiometric accuracy. This is especially so with respect to the sun as shown in the sensitivity analysis. One of the rays must go to the sun. To a much lesser extent, the sensitivity analysis showed the sampling of the specular lobe can be important.

Integration Approach:

If the radiance and reflectance maps are modeled as functions, the ray tracer could be used to set the limits of integration. The radiance from a solid angle would not be calculated until the ray tracer mapped out a contiguous section such as the sky or the side of a building. This approach would minimize error and is recommended in the future. The form would be very close to the continuous form.

$$L = \int_{\phi_1} \int_{\theta_1} L(\phi, \theta) * r(\phi, \theta) \partial\phi \partial\theta + \int_{\phi_2} \int_{\theta_2} L(\phi, \theta) * r(\phi, \theta) \partial\phi \partial\theta + \dots$$

$$+ \int_{\phi_N} \int_{\theta_N} L(\phi, \theta) * r(\phi, \theta) \partial\phi \partial\theta$$

### **5.2.2 Inputs to the model**

The proposed model requires three inputs; spectral emissivity values, specular lobe parameters, and orientation angles.

The spectral reflectivity values can be obtained from common directional reflectivity instruments. Visible and near-infrared values must be obtained for each material. Infrared values, depending on the fidelity required, may be obtained for a class of materials.

Specular reflectivity values can be obtained from Plane of Incidence (PLIN) measurements. These values can be used for a class of materials. A coarse estimate can be made through an image of a material illuminated by a point source (sun). The spread of the point source as reflected by the material in the image would indicate the width of the base of the spectral lobe. The peak is the reflectance in the specular direction. (See Appendix B for more details on obtaining specular reflectivity values.)

Care must be made to ensure that the effective aperture of the measured reflectance values matches the resolution of the synthetic scene.

Orientation angles are a function of the amount of effort used to create the geometric database and the quality of the input data available. Possible measures to improve this calculation of orientation angles are discussed in Section 5.2.4.

### **5.2.3 Incorporation into DIRSIG**

The value of this research is limited if not incorporated into DIRSIG. This section reviews, in detail, the required changes to DIRSIG. The goal is to facilitate the incorporation of the changes. Incorporation will require changes to the ray tracer model and to the structure and contents of the emissivity database. The changes to the ray tracer were discussed in Section 5.2.1. The changes to the emissivity database include the addition of parameters to describe the specular lobe and a redefinition (and use) of the fall-off values. The structure and contents of proposed emissivity database is shown in Figure 5.22. This is followed by a discussion of the mechanics of the actual calculation of the radiance exiting a facet.

<i>Row</i>	<i>Col 1</i>	<i>Col 2</i>	<i>Col 3</i>	<i>Col 4</i>	<i>Comments</i>	
<i>1</i>	8				number of curves in the file	
<i>2</i>	1.000				Fall-off values	
<i>3</i>	1.000				The values start at zenith and decrement by one degree intervals for a total of 91 values	
<i>4</i>	.999					
<i>.</i>	<i>.</i>					
<i>.</i>	<i>.</i>					
<i>.</i>	<i>.</i>					
<i>.</i>	<i>.</i>					
<i>91</i>	0.256					
<i>92</i>	0.123					
	<i>a</i>	<i>b</i>	<i>c</i>	<i>d</i>		These values describe the specular cone. They begin at zenith and go to 90 degrees at 15 degrees increments, for a total of 7 rows. I've included four values to describe the dome even though I currently plan to use two values. a - cone depth [emissivity units] b - cone base radius [degrees] c - not used d - not used
<i>93</i>	0.4	36.5	-999	-999		
<i>94</i>	0.5	21.0	-999	-999		
<i>95</i>	0.3					
<i>96</i>	<i>.</i>					
<i>97</i>	<i>.</i>					
<i>98</i>	<i>.</i>					
<i>99</i>	<i>.</i>				Interpolation will be used between given angles	
<i>100</i>	0				Curve number 0	
<i>101</i>	39850	.432			wavenumber, spectral emissivity value.	
<i>102</i>	39750	.345			This number describes the dome.	
<i>.</i>						



Figure 5.22. Proposed emissivity database (.ems file) structure. Italicized text and the comments are not part of the file

The first row gives the number of spectral curves in the file. Additional curves are used for texture routines. The next 91 rows (Rows 2-92) are the fall-off values. The fall-off values serve two functions. They reduce the overall reflectance at high view angles and they attenuate the radiance the facet receives at high zenith angles. The next seven rows (Rows 93-99) describe the specular lobe. Each row describes the lobe at 15 degrees increments, starting at zenith (0 degrees). For specular angles that fall between the increments interpolation is used. The file shown assumes a cone function for the specular lobe. The first column describes the depth, in emissivity units, of the specular lobe below the diffuse component. Note that the database is given in emissivity units, therefore the specular “bump” in reflectivity units is a “dip” in emissivity units. The second column describes the cone base radius, in degrees. The last two columns are not used. The remaining rows describe the spectral (diffuse) emissivity at  $100 \text{ cm}^{-1}$  (wavenumber) increments starting at  $39850 \text{ cm}^{-1}$  and ending at  $350 \text{ cm}^{-1}$ . Interpolation is used as required.

The implementation of this database (reflectance map) with the radiance map for a single detector element (pixel) is given below. The goal is to aid the incorporation process and further the understanding of the mechanics of the calculation of the radiance exiting a facet. The description parallels the ray-tracer algorithm.

1. A ray is cast and a facet passes the intersection test. The assumption is that the facet is opaque. At this point, the following parameters are known.

INPUTS:       $\phi_{\text{ray\_primary\_incident}} = \phi_{\text{rpi}}$                $\theta_{\text{ray\_primary\_incident}} = \theta_{\text{rpi}}$   
                   $\phi_{\text{facet\_normal}} = \phi_{\text{fn}}$                        $\theta_{\text{facet\_normal}} = \theta_{\text{fn}}$   
                  MATERIAL\_ID

These parameters serve partial input to the calculations.

2. At this point, the input parameters can be modified through topography, texture, and material maps. This is optional and is described in Section 5.2.4.
3. The emissivity is then calculated through the following actions. Reference angles are shown in Figure 5.23 to aid the discussion.

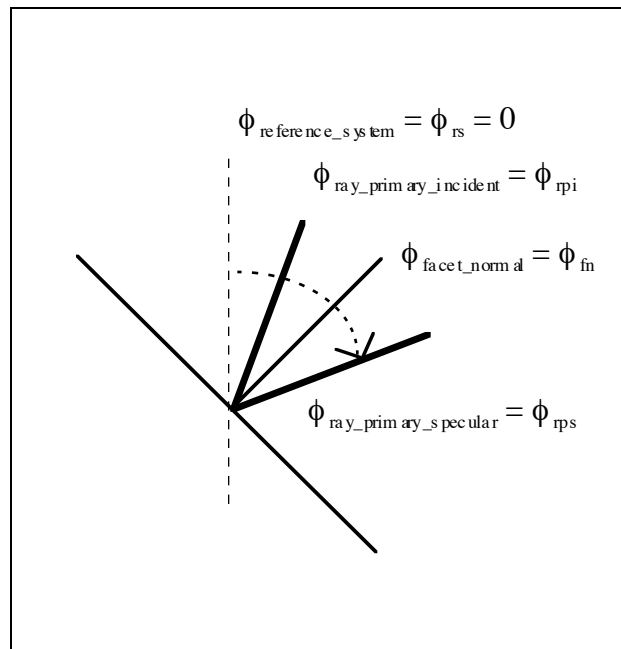


Figure 5.23. Reference Angles

- Compute specular angles

$$\phi_{\text{rps}} = (\phi_{\text{fn}} - \phi_{\text{rpi}}) + \phi_{\text{fn}} = 2\phi_{\text{fn}} - \phi_{\text{rpi}}$$

$$\theta_{\text{rps}} = 2\theta_{\text{fn}} - \theta_{\text{rpi}}$$

- Select the secondary ray casting strategy. This description varies from the current DIRSIG secondary ray casting strategy. The goal is to cast more rays into the specular lobe without incurring a computational penalty of calculating the optimum angles on-the-fly. The technique proposed uses one of three fixed sets of angles for casting the secondary rays. The fixed set of angles breaks up the hemisphere above the facet into 61 equal solid angles. (24 of the solid angles, the ones at a zenith angle of 90 degrees, are half the area so the effective number of solid angles is 49). This concept is illustrated in Figure 5.24. The effect is to create half a “golf-ball” over the facet, a dome made of hexagons. Within a subset of the solid angles, additional rays are cast to accommodate an increased sampling of the specular lobe. The subsets are centered about zenith angles of 0, 22.5, and 45 degrees. This is illustrated in Figures 5.25-27. The selection of which “golf-ball” to use is a function of the specular bounce angle. The logic is given below.

If  $|\phi_{\text{rps}} - \phi_{\text{fn}}| > 33.75$                     then golf\_matrix\_3

Else if  $|\phi_{\text{rps}} - \phi_{\text{fn}}| > 11.25$             then golf\_matrix\_2

Else golf\_matrix\_1

- Compute secondary ray angles. The effect of the following calculations are to orient the rays of the golf-ball in azimuth and zenith directions with respect to the orientation of the facet. The result is a set rays.

$$\phi_{srx} = \phi_{fn} + \phi_{golf_x}$$

$$\theta_{srx} = \theta_{fn} + \theta_{golf_x}$$

$$\phi_{secondary\_ray(s)} = \phi_{sr} \quad \theta_{secondary\_ray(s)} = \theta_{sr}$$

- Read .ems file. These values will be used as input to the calculations of the sensitivity (emissivity) of the secondary rays to the radiance they “encounter.”

spectral\_ems(wn)

fall\_off ( $\phi_{fall\_off} = \phi_{fo}$ )

specular\_ems ( $\phi_{fall\_off}$ )

- Compute  $\alpha$  and  $\beta$ , the specular lobe depth and base radius, through interpolation. (The database values are given in 15 degree increments.)

INPUTS:       $\alpha_1$        $\beta_1$        $\alpha_2$        $\beta_2$       ( $\phi_{rps} - \phi_{fn}$ )

$\alpha$  and  $\beta$  are the interpolated values between the  $\alpha$  and  $\beta$  values.









$$\text{where } \phi_i = [ (\phi_{\text{tps}} - \phi_{\text{sr}})^2 + (\theta_{\text{tps}} - \theta_{\text{sr}})^2 ]^{1/2}$$

- Compute `ems_secondary_ray(s)`. The first test is to see if the ray falls within the specular lobe. If it does not, the sensitivity (emissivity) of the ray is the spectral (diffuse) emissivity times the fall-off value. The `spectral_emissivity` is interpolated for the wavenumber being calculated. (The values in the database are at  $100 \text{ cm}^{-1}$  increments.) The fall-off values attenuate the sensitivity of the ray at high relative zenith angles. If the ray is in the specular lobe, the emissivity is calculated using the formula listed below. The formula linearly increases the sensitivity as the rays approach the specular bounce direction.

Is  $\phi_i \leq \beta$ ?

No =>  $\epsilon_{\text{sr}} = \text{spectral\_emissivity} * \text{fall\_off}$

Yes =>  $\epsilon_{\text{sr}} = ( \text{spectral\_emissivity} + (\alpha - \alpha / \beta * \phi_i) ) * \text{fall\_off}$

The output is a set of secondary rays with their associated sensitivities and fraction of the hemisphere they represent. The output is shown in Figure 5.28.

<code>secondary_ray_1</code>	<code>ems_1</code>	<code>solid_angle_percent_1</code>
<code>secondary_ray_2</code>	<code>ems_2</code>	<code>solid_angle_percent_2</code>
<code>secondary_ray_3</code>	<code>ems_3</code>	<code>solid_angle_percent_3</code>
.	.	.
.	.	.
.	.	.
<code>secondary_ray_103</code>	<code>ems_103</code>	<code>solid_angle_percent_103</code>

Figure 5.28. Call Emissivity Output

4. The rays are then cast to acquire the radiance values from the radiance map for the solid angle the ray represents. If the individual ray hits the sun, the solar radiance term is attenuated by the sensitivity of the ray. (The `solid_angle_percent` is ignored because the solid angle of the ray is much larger than the solid angle of the sun angle and the reflectance over that solid angle is constant.) Because of the importance of the solar radiance, an additional ray should be cast in the exact direction of the sun. If the individual rays hit the atmosphere, the downwelled radiance for that solid angle is attenuated by the sensitivity of the ray. It is important that the solid angle of the radiance match the solid angle of the ray to minimize error. Typically, the resolutions of the reflectance and radiance maps differ. When the rays intersect the radiance map an interpolated value between the four nearest neighbors is calculated. That value represents a defined solid angle, the value to the solid angles are also interpolated. To adjust the value to represent the correct solid angle it must be multiplied by the fraction

$$\frac{\text{ray solid angle percent}}{\text{radiance solid angle percent}}$$

If the individual rays hits a transmissive object, the attenuation for reduction of the radiance from that direction is noted and the ray is continued. If the ray strikes an opaque facet, the `spectral_ems` and  $\alpha$  (the cone height) are noted. A ray is then cast to the sun. If sunlit, the solar radiance term and downwelled radiance are attenuated by the `spectral_ems` plus  $\alpha$  if the sun is within 10 degrees of the specular direction. If greater than 10 degrees, they are attenuated by only the `spectral_ems`. If not sunlit, the downwelled radiance is attenuated by the `spectral_ems`.

5. The individual contributions are then summed. This total is then attenuated by the fall-off value as determined by the view angle.

$$\phi_{\text{fall-off}} = \phi_{\text{fn}} - \phi_{\text{rpi}}$$

This is the radiance exiting the facet.

This detailed implementation description, hopefully, illustrated the sensitivity of the value of the concepts presented in this study to how they are implemented. The sensitivity analysis of the proposed model is now presented.

#### 5.2.4 Sensitivity Analysis of the Proposed Model

The Big Equation as implemented by DIRSIG would then be

$$\text{total\_radiance} = \text{total\_transmission} * (\text{emissive\_component} + \text{reflective\_component} + \text{transmissive\_component}) + \text{upwelled\_radiance}$$

where

total_transmission	-	$\tau_2$ - the atmospheric transmittance
emissive_component	-	output of the therm submodel
reflective_component	-	reflected radiance from a facet
transmissive_component	-	transmissive contribution from a facet
upwelled_radiance	-	$L_{\text{us}}$ upwelled radiance

However, analysis of this equation would not be informative so the reflective\_component is expanded one more level as shown below.

$$\begin{aligned} \text{total\_radiance} = & \text{total\_transmission} * (\text{emissive\_component} + \\ & \text{solar\_radiance} * \text{reflectance} \\ & + \text{downwelled\_radiance} * \text{reflectance} + \text{transmissive\_component}) + \\ & \text{upwelled\_radiance} \end{aligned}$$

where

$$\begin{aligned} \text{solar\_radiance} & \quad - \quad E_{s_s} * \cos\sigma * \tau_1 / \pi \\ \text{reflectance} & \quad - \quad \text{BDRF} \\ \text{downwelled\_radiance} & \quad - \quad F * L_{ds_s} + (1 - F) * L_{bs_s} \end{aligned}$$

The error ( $S_{\text{total\_radiance}}$ ) in total\_radiance is then given by

$$\begin{aligned} S_{\text{total\_radiance}}^2 = & \left( (\text{emissive\_component} + \text{solar\_radiance} * \text{reflectance} + \right. & * S_{\text{total\_transmission}})^2 \\ & \left. \text{downwelled\_radiance} * \text{reflectance} + \text{transmissive\_component}) \right. & * S_{\text{emissive\_component}} \\ + & \left( \text{total\_transmission} \right. & \\ + & \left( \text{total\_transmission} * \text{reflectance} \right. & * S_{\text{solar\_radiance}})^2 \\ & \left( \text{total\_transmission} * (\text{solar\_radiance} + \text{downwelled\_radiance}) \right. & * S_{\text{reflectance}})^2 \\ & \left. \left( \text{total\_transmission} * \text{reflectance} \right. \right. & * S_{\text{downwelled\_radiance}} \\ + & \left. \left( \text{total\_transmission} \right. & * S_{\text{transmissive\_component}} \right. \\ + & \left. \left( 1 \right. & * S_{\text{upwelled\_radiance}})^2 \end{aligned}$$

The estimated error (S) for each of the variables is given in Table 5.10. The source data for these estimates comes from prior DIRSIG testing and engineering judgment. The error assumes a one sigma probability distribution.

Table 5.10. Error Variable Values

Error Variable	Value (%)
$S_{\text{total\_transmission}}$	4

$S_{\text{emissive\_component}}$	8.85
$S_{\text{solar\_radiance}}$	8.85
$S_{\text{reflectance}}$	2.5
$S_{\text{downwelled\_radiance}}$	8.85
$S_{\text{upwelled\_radiance}}$	6.35

This analysis considers the same four cases used earlier for DIRSIG. The results are shown in Tables 5.11-14.

Case 1a and 2a results are very similar to the Case 1 and 2 results. The only notable difference is that the error in reflectance is combined into a single term. The Case 3a results showed a significant increase in the error contribution of the solar\_radiance term, approximately 6%, over Case 3. It also showed a significant decrease in the error contribution of the total\_transmission term, approximately 6%. The error in the remaining terms was fairly constant with Case 3. The reason for these shift was the increase in sensitivity of the proposed model to the directional characteristics of reflectivity. Case 4a supports this also, the error in solar\_radiance increased with an increase in specular reflectance. This indicates that the directional characteristics are important and should be accounted for in the model.









The simple sensitivity analysis showed that the directional nature of reflectivity is significant and must be addressed for the model to be considered robust. The sensitivity analysis of DIRSIG shows that how it addresses reflectivity could be improved. Finally, the sensitivity analysis of the new model showed that proposed changes will improve the robustness of DIRSIG.

### **5.2.5 Topography, Texture, and Material Maps**

This section is beyond the scope of this study but illustrates the potential of the proposed model. Because it is optional, the same scientific rigor is not applied.

#### **5.2.5.1 Topography Maps (optional section)**

The value of topography maps are two-fold. First they allow the scene to be built with fewer facets. Second they allow for infinite geometric resolution. To capture a curved surface such as a hill or a car bumper in DIRSIG, the scene builder must control two factors, resolution and the number of facets used to describe the geometric shape of the object. This concept shown in Figures 5.29-30.

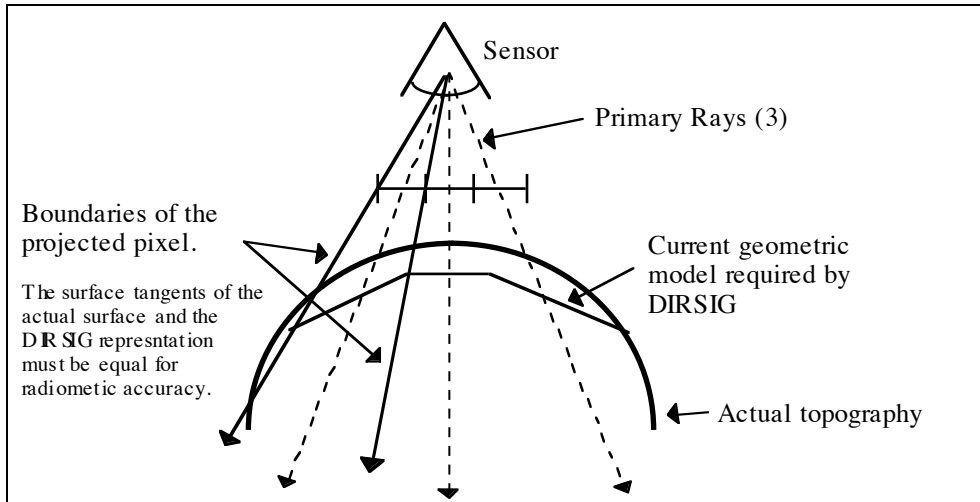


Figure 5.29. Surface Topography - lower resolution

Because the sensor projects three pixels onto the surface the geometric resolution of the DIRSIG image must be three facets. (See Figure 5.29.)

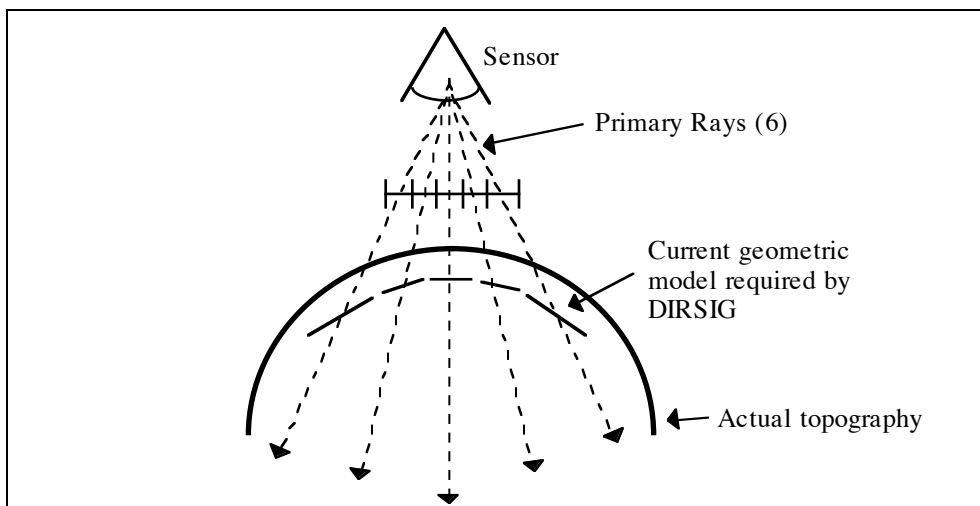


Figure 5.30. Surface Topography - higher resolution

At the resolution shown in Figure 5.30 the geometric model must contain 6 facets.

The greater the resolution greater the number of facets required. The size of the facets should equal the projected pixel size of the image. If the number is less, the specular bounce may be incorrect and the shape factor incorrect. If the number is greater, the scene builder has wasted energy. In addition, a greater resolution in the geometric model than needed does not ensure radiometric accuracy. The facet tangent must be equal to the tangent of the actual surface over the “integration” area as defined by the projected pixel.

Because the sensor averages over the projected area of the detector, the best estimate for the specular direction is the average normal over that area plus the specular difference. This leads to topography maps. The idea is to create a facet much larger than the resolution of the synthetic to reduce construction time and assign to it a topography map. The map would ideally be a continuous function. A discrete map would be acceptable as long as its resolution was greater than the scene resolution. The process for using the topographical map is described below.

1. Pass the intersection test.

OUTPUT:     (x, y, z) of the intersection point  
              (x, y, z) vector of the intersecting ray  
              Facet\_ID\_number  
              Material\_ID\_number  
              Pixel Projected Area

2. Access the topographical map. This is shown in Figure 5.31.

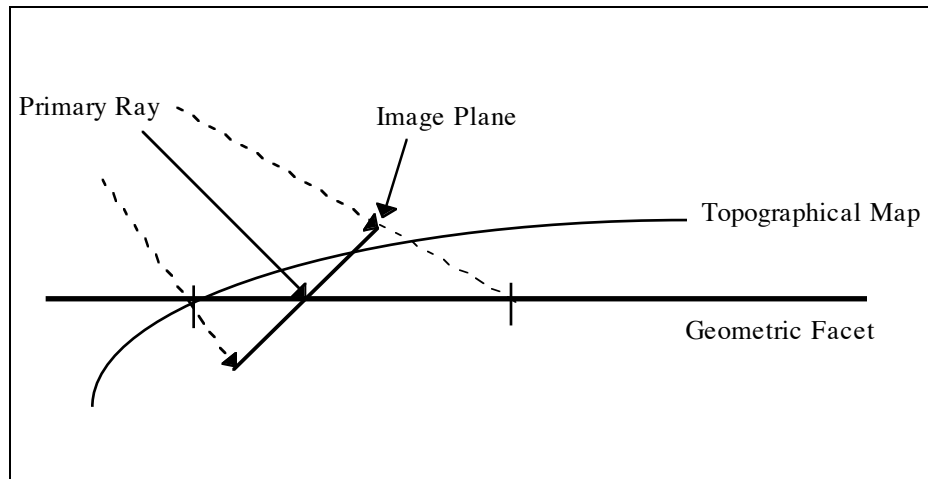


Figure 5.31. Topographical Map

3. Calculate the average normal to the topographical map over the project pixel area (two dimensions. (At this point the average normal for the entire topographical map could be made to reduce computational time later.)
5. Calculate the direction of the correct specular bounce based on the average normal.
6. Calculate the intersection point of the primary ray with the topographical map.
7. Use this point and vector as the INPUT to the remaining emissivity calculation.

Topographical maps for terrain can be generated automatically through photogrammetric techniques from reference imagery.

### 5.2.5.2 Material Maps

The value of material maps is that it will allow for mixed pixels without down sampling of synthetic images. The approach is similar to that of topographical maps. The output

of the process is a material\_ID and percentage for each material in the projected pixel area. These values would be used in the calculation of the radiance exiting the facet.

Material maps can be generated from classification maps of reference imagery.

### **5.2.5.3 Texture Maps**

The value of texture maps is that they allow for the duplication of texture found in nature. The approach is similar to that of Material maps except that the output is a single material and emissivity curve numbers.

## **6.0 Summary**

In the first part of this study, DIRSIG was validated. The validation showed that DIRSIG was capable of producing radiometrically accurate imagery in the reflective region. The results also showed that DIRSIG's robustness could be improved.

In the second part of this study, methods were developed to increase DIRSIG's robustness with respect to imagery created in the reflective region. The methods included, in part, a new reflectance model and methods to create databases to feed the model. Sensitivity analysis of the new model showed a potential improvement (slight) in overall radiometric accuracy. (No degradation from the current model.) It also showed that the new model will be accurate over a broader range of imaging conditions, an increase in robustness..

## 7.0 References

- AutoCad Release 10 Reference Manual, Autodesk Inc., 1989.
- Beers, Y., "Introduction to the Theory of Error," Addison-Wesley Publishing Company, Inc., Reading Mass., 1957.
- Berk, A., L.S. Bernstein, and D.C. Robertson, "MODTRAN: A moderate resolution model for LOWTRAN 7," GL-TR-89-0122, Spectral Sciences Inc., April 1989.
- Cathart, J.M., and A.D. Sheffer, "Target and background infrared signature modeling for complex synthetic scenes," *Infrared Systems and Components II (1988)*, SPIE Vol. 890, pp. 95-103, 1988.
- Cook, R.L. and K.E. Torrence, "A Reflectance model for Computer Graphics," *ACM Transactions on Graphics*, Vol. 1, No 1, pp. 7-24. January 1982.
- Culpepper, Mark A., "Empirical bidirectional reflectivity model," SPIE Vol. 2469, pp.208-209, 1995.
- DCS Corporation and J.R. Schott, "Automatic target recognition/counter-countermeasures technology development program model review," DCS Report No. 13430LT003Z, Autometric Incorporated, 1987.
- Feng, X., "Comparison of methods for generation of absolute reflectance factor measurements for BDRF studies," M.S. Thesis, Rochester Institute of Technology, Center for Imaging Science, December 1990.
- Francis J., L. Maver, and J.R. Schott, "Comparison of physically and computer generated imagery," *Image Modeling*, SPIE Vol. 1904, pp. 20-33, 1993.
- Henry A.C., "TAV-IR: A visible and near-IR radiometric analysis code which operates with an off-the-shelf computer animation package," *Characterization and Propagation of Sources and Backgrounds*, SPIE Vol. 2223, pp. 445-487, 1994.
- Kneizys, F.X., E.P. Shettle, L.W. Abreu, J.H. Chetwynd, G.P. Anderson, W.O. Gallery, J.E.A. Selby, and S.A. Clough, "Users Guide to LOWTRAN 7," AFGL-TR-88-0177, Environmental Research Papers, No. 1010, Air Force Geophysics Laboratory, Optical/Infrared Technology Division, Hanscom AFB, MA,

December 1988.

Kodak Aerial Systems, "Aerial Imagery," Rochester, NY, 1994.

Kornfeld, G.H., "Digital simulation of precise sensor degradations including nonlinearities and shift variance," *Infrared Image Processing and Enhancement*, SPIE Vol. 781, pp. 63-70, 1987.

Kraska, T., "DIRSIG (Digital Image and Remote Sensing Image Generation) Model: Infrared Airborne Validation and Input Parameter Analysis," M.S. Thesis, Rochester Institute of Technology, Center for Imaging Science, April 1996.

Lehman, E.L., "Nonparametrics; Statistical Methods Based on Ranks," Holden-Day, Inc., San Francisco, 1975.

National Imagery Resource Library Non-Conventional Exploitation Factors Database, U.S. Government, 1995.

Lindahl, C., A. Cockcroft, T. Derryberry, J. Sigler, and M. Yablonski, "Synthetic, multisensor, database generation and validation," *Signal and Image Processing Systems Performance Evaluation*, SPIE Vol. 1310, pp. 88-94, 1990.

Mason, J. E., and J.R. Schott, "Validation analysis of the thermal and radiometric integrity of RIT's synthetic image generation model, DIRSIG" *Characterization and Propagation of Source and Backgrounds*, SPIE Vol. 2223, pp. 474-487, 1994.

Maver, L., and L. Scarff, "Multispectral imagery simulation," *Image Modeling*, SPIE Vol. 1904, pp. 144-160, 1993.

Phong, B.T., "Illumination for Computer Generated Pictures," *Communications of the ACM*, 18(6), pp.311-317, June 1975.

Salacain, J. M., "Application of Imaging System Geometric Models to a Synthetic Image Generation System," M.S. Thesis, Rochester Institute of Technology, Center for Imaging Science, March 1995.

Salvaggio, C., G. Braun, and J.R. Schott, "SVGM; a spectral vector generating model using the LOWTRAN 7 and SCATRAN atmospheric propagation codes,"

RIT/DIRSD 90/91-63-141, prepared for Eastman Kodak Company, Federal Systems Division, January 1991.

Salvaggio, C., R. Raqueno, J.S. Warnick, E. Kraus, and J.R. Schott, "A thermal infrared synthetic image generation model," Final Report RIT/DIRS 90/91-63-142, prepared for the Central Intelligence Agency, Office of Development and Engineering, April 1991.

Schott, J.R., M. Fairchild, X. Feng, R. Raqueno, B. Brower, and T. Galligher, "Techniques for measurement of the optical properties of materials," Final Report RIT/DIRS 89/90-51-134, prepared for the United States Department of Energy, January 1990.

Schott, J.R. J.E. Mason, C. Salvaggio, J.D. Sirianni, R.A. Rose, E.O. Kulp, and D.K. Rankin, "DIRSIG-Digital Imaging and Remote Sensing Image Generation Model: Description, Enhancement, and Validation," RIT/DIRS report 92-93-51-146, prepared for the Central Intelligence Agency, Office of Development and Engineering, July 1991.

Schott, J.R., et al., "DIRSIG - Digital Imaging and Remote Sensing Image Generation Model: Description, Enhancements and Validation", RIT/DIRS Report 92/93-51-146, Office of Development and Engineering, Central Intelligence Agency, July 1993.

Schott, J.R., "Remote Sensing; The Image Chain Approach," (book in progress) Oxford Press, NY, 1997.

Servoss, T., "Infrared Symbolic Scene Comparator." M.S. Thesis, Rochester Institute of Technology, Center for Imaging Science, October 1993.

Side Corporation, "Demonstration of DIRSIG Capabilities," Side Report, 1996.

Stark R., "Synthetic Image Generation Model: Application of Specular and Diffuse Reflectivity Components and Performance Evaluation in the Visible Region," M.S. Thesis, Rochester Institute of Technology, Center for Imaging Science, September 1993.

